Novel Hardware Implementation and Adaptive Beamforming Algorithms for Microwave Beamforming Structure

Sadegh Farzaneh Koodiani

A Thesis

in

The Department

of

Electrical and Computer Engineering

Presented in Partial Fulfilment of the Requirements for the

Degree of Doctor of Philosophy (Ph.D.)

Concordia University, Montreal, Quebec, Canada

September 2008

Your file Votre référence
ISBN: 978-0-494-45668-2
Our file Notre référence
ISBN: 978-0-494-45668-2

Abstract

Novel Hardware Implementation and Adaptive Beamforming Algorithms for Microwave Beamforming Structure

Sadegh Farzaneh Koodiani, Ph.D.
Concordia University, 2008

Using beamforming in a wireless communication channel increases its capacity. A major challenge in deploying beamforming in commercial wireless communications is the high implementation cost. Microwave beamforming (MBF) is a low complexity alternative due to using only one radio frequency (RF) down-conversion and analog to digital converter (ADC). However, traditional MBF structures employ a phase shifter and a gain control block per antenna element which are expensive and bulky. Moreover, signal processing for MBF structures is more difficult due to lack of an antenna array signal vector in the processor.

This thesis investigates both the microwave hardware and the signal processing issues associated with the MBF structures. It introduces a new low-complexity beamforming implementation technique, the microwave sampling beamformer (MSBF). In addition, a new perturbation technique based on array signal estimation is devised for application of advanced signal processing to the MBF structures. Throughout this research different RF implementation and signal processing issues are jointly taken into account.

In the proposed MSBF structure, phase shift and amplitude attenuation are controlled through switching of the antenna array signals using control pulses with adjusted time delay and pulse width. Both the phase shift and amplitude attenuation are

controlled over the full range in one simple block. The proposed structure is validated in the frequency and time domains with microstrip and wire antenna arrays. Different MSBF issues such as switch design, finite duration pulse train, and image replica rejection are investigated. A four-element prototype of the MSBF structure composed of the microwave and control hardware is constructed and tested. The beamforming structure is designed to have eight bits phase shifter resolution and 12 bits amplitude resolution. The whole prototype is examined for beam steering, side-lobe level (SLL) control, and null-forming.

In the new perturbation technique the antenna array signal vector is estimated based on the array signal temporal correlation. The temporal correlation is provided by a fast perturbation rate or receiver bandwidth reduction. Single-port adaptive unconstrained least mean square (ULMS) beamforming and multiple signal classification (MUSIC) DOA algorithms are investigated and they outperform the corresponding multi-port algorithms depending on the channel scenario.

Acknowledgements

Thanks God for being with me in another stage of my life and granting me another opportunity to know many new dignified people and to learn from them.

I would like to express my sincere appreciation to my supervisor Prof. Abdel Razik Sebak for all his technical help, supervision, and encouragement in all steps of my thesis. His patience, friendly attitude, and trust created a pleasant environment that comforted my PhD studies. I would like also to thank him for being always available for technical discussions and quick response to the correspondences. I am also truly grateful to him for supporting my studies financially as an international student. I learned many things in the courses I took with him and gained a lot of teaching experience through working with him as teaching assistant and teaching fellow.

I am very grateful to Prof. Robert Paknys as a member of my committee for his valuable comments and help in developing this work. I also thank him for his support during the implementation and measurement processes. I learned many things during technical discussions on the hardware implementation part of the thesis, and the advanced electromagnetic course I took with him. I also appreciate the time he dedicated to careful reading of this thesis.

I wish to express my warm sincere to Prof. Christopher W. Trueman as a member of the thesis committee and the department chair for his valuable comments. I also thank him for careful editing of this thesis.

I wish to thank Dr. Ibrahim Galal Hassan as a member of the thesis committee from mechanical and industrial engineering department of Concordia University for his valuable comments.

I would like to thank Prof. Gilles Y. Delisle, my external examiner, from Techno pole defence and security in Quebec for accepting to be part of the committee and for his constructive comments.

My sincere thanks to Dr. Tayeb Denidni for offering to use the INRS facilities for the measurements.

I wish to thank Alper Ozturk for his kind help during the preparation of the antenna measurement setup and performing the measurements.

I would like to thank the undergraduate students of Concordia University Nader Sharif, Essoufy Salah eddine, Hameed Dhafir, Prince Mahdi Masud, Richard Ntone Epee for their help in implementing the control hardware.

I also wish to thank Jules Gauthier the chief technician at Ecole Polytechnique de Montreal for his comments on the hardware implementation part of the thesis.

I owe my loving thanks to my wife and my son, and my parents for their love, patience, and support. They have lost a lot because of my Ph.D research. Without their understanding and support this thesis would be impossible to accomplish.

Dedicated to my parents, my wife, and my son

Table of Contents

List of Tables

List of Figures and Illustrations

List of Abbreviations and Nomenclature

Symbol	Definition
ABF	Adaptive beamforming.
ADC	Analog to digital converter.
ADS	Advanced design system.
AM	Adaptation mode.
BPF	Bandpass filter.
CDMA	Code division multiple access.
CGA	Conjugate gradient algorithm.
CLMS	Constrained least mean square.
CMA	Constant modulus algorithm.
CSI	Channel state information.
DAC	Digital to analog converter.
DBF	Digital beamforming.
DC	Direct current.
DIS	Directional interference source.
DOA	Direction of arrival.
DSD	Differential steepest descent.
DSP	Digital signal processor.
ESPAR	Electrically steerable parasitic array radiator.
FDMA	Frequency division multiple access.
FET	Field effect transistor.
HFSS	High frequency structural simulator.
HMIC	Hybrid microwave integrated circuit.
I/O	Input/output.
IF	Intermediate frequency.
LBF	Local beamforming.
LNA	Low noise amplifier.
LPF	Lowpass filter.
LRS	Linear random search.
LSB	Least significant bit.
MBF	Microwave beamforming.
MCC	Maximum cross-correlation algorithm.
MCMA	Modified constant modulus algorithm.
MMIC	Monolithic microwave integrated circuit.
MMSE	Minimum mean square error.
MSB	Most significant bit.
MSBF	Microwave sampling beamformer.
MSE	Mean square error.
MUSIC	Multiple signal classification.
NEC	Numerical electromagnetics code.
NM	Normal mode.
PPW	Positive pulse width.
RF	Radio frequency.
RFI	Radio frequency interference.

RLS	Recursive least square.
SDMA	Space division multiple access.
SINR	Signal to interference plus noise ratio.
$SINR_O$	Output signal to interference plus noise ratio
SIR	Signal to interference ratio.
SLL	Side-lobe level.
SMI	Sample matrix inversion.
SMILE	Spatially multiplexing of local elements.
SNR	Signal to noise ratio.
SP-ANF	Single-port adaptive null-forming
SPBS-MUSIC	Single-port beam-space MUSIC
TD	Time delay.
TDMA	Time division multiple access.
TTD	True time delay.
ULMS	Unconstrained least mean square.
UWB	Ultra-wideband.

List of Symbols

Symbol	Definition
$\mathbf{A}$	L by $(L+1)$ perturbation matrix.
a_l	l^{th} element amplitude attenuation.
$\mathbf{B}$	Beam-space transformation matrix.
b	Fractional bandwidth.
B_1	Signal bandwidth after expansion.
B_b	Beam broadening factor.
B_c	LPF cut-off frequency.
B_{c1} and B_{c2}	First and second LPFs cut-off frequencies.
B_N	Null bandwidth.
c	Speed of light in the free space.
c_{nl}	n^{th} Fourier series coefficient of the l^{th} element pulse train.
$\hat{c}_{nl}$	Fourier series coefficient including the effect of the combiner, LNA, and mixer.
$\text{cov}(\mathbf{g}(\mathbf{w}(n))$	Covariance of the gradient vector with a weight vector $\mathbf{w}(n)$.
d	Array element spacing.
$\mathbf{D}$	Diagonal matrix with diagonal elements $\mathbf{D}(i,i) = d_i$.
$\mathbf{E}$	L by L matrix whose columns are the eigenvectors of $\mathbf{R}$.
$\mathbf{e}_1$	A vector with all elements equal to zero except the first element.
E[.]	Statistical average (expectation operation).
$\mathbf{E}_{bn}$	Beam-space noise subspace.
$\mathbf{E}_n$	Matrix with L-M columns being the eigenvectors corresponding to the M smallest eigenvalues of $\mathbf{R}$.
$\mathbf{e}_{\text{NL}}$	The nonlinear error term in the gradient average.
$\mathbf{E}_{\text{P}}$	The error term in the gradient average.
$\mathbf{E}_s$	Matrix with M columns being the eigenvectors corresponding to the M largest eigenvalues of $\mathbf{R}$.
f	Frequency variable.
$F\{.\}$	Fourier transform operation.
f_0	Center frequency.
f_c	Carrier frequency.

f_m	Message Frequency.
f_s	Sampling frequency.
f_w	Weighting rate.
$\mathbf{g}(\mathbf{w}(n))$	Gradient vector with a weight vector $\mathbf{w}(n)$.
$\bar{g}(\mathbf{w}(n))$	Average of the gradient vector with the weight vector $\mathbf{w}(n)$.
$\hat{\mathbf{g}}(\mathbf{w}(n))$	The gradient vector with the estimated array signal vector.
h	Height of the substrate dielectric layer.
$\mathbf{I}$	Unitary matrix.
I_{D1}, I_{D2}	First and second diodes currents.
k_0	Wave number in the free space.
L	Number of antennas.
L_d	Length of the PIN diode.
$L_k, k = 1,2,3,4$	Length of the switch transmission line sections.
L_t	Beamformer ohmic loss.
$m(t)$	Message signal.
M	Number of interference sources.
MA	Misadjustment.
MA_{tot}	Total misadjustment.
$m_i(t)$	The complex modulating signal corresponding to the i^{th} source.
$\mathrm{m}_s((n+k)T_w)$	Desired signal in the k^{th} perturbation cycle of the $(n+1)^{th}$ iteration.
$m_T(t)$	Message signal multiplied by a rectangular pulse with duration T .
$M_T(f)$	Fourier transform of $m_T(t)$.
N	Number of samples used in the LRS algorithm for gradient estimation.
N_0	Number of iterations.
n_0	The smallest harmonic number larger than the image harmonic.
$n_l(t)$	White noise on the l^{th} element.
N_τ	Address bits of the pulse width control IC.
N_{td}	Address bits of the time delay control IC.
$P(\mathbf{w})$	Array output power.
$\mathbf{P}$	Projection matrix.
P	Perturbation error.
p_i	i^{th} source power.
$p_l(t)$	Sampling pulse train.

$\hat{p}_l(t)$	Sampling pulse train of the l^{th} element with finite duration.
$P_{\text{MU}}(\theta)$	Spatial spectrum of MUSIC algorithm.
P_n	Noise power.
p_{NO}	Interference plus noise beamformer output power.
p_S	Desired signal power.
p_{SO}	Desired signal beamformer output power.
$P_{SP-ANF}(\theta)$	Spatial spectrum of single-port adaptive null-forming algorithm.
$P_{\text{SPBS-MU}}(\theta)$	Spatial spectrum of single-port beam-space MUSIC.
Q	Weighting rate coefficient.
$r(t)$	Reference signal at the time instant t.
$r(n+1)$	Reference signal in the $(n+1)^{\text{th}}$ iteration cycle.
$\mathbf{R}$	Array covariance matrix.
R_0	Radius of the curved line in the switch.
$\bar{\mathbf{R}}$	The matrix that replaces $\mathbf{R}$ in the convergence of the single-port ULMS algorithm based on array signal estimation.
$\mathbf{R}_e$	*(L+1)* by *(L+1)* error matrix with zero diagonal elements.
$\hat{\mathbf{R}}$	The covariance matrix of the estimated array signal.
$\mathbf{R}_N$	Interference plus noise covariance matrix.
$\mathbf{R}_S$	Desired signal covariance matrix.
$\tilde{\mathbf{R}}$	The matrix that replaces $\mathbf{R}$ in the perturbation algorithm based on array signal estimation.
$\mathbf{R}_x^{(q)}$	Cross-correlation matrix of $\mathbf{x}_k(n+1)$ and $\mathbf{x}_{k+q}(n+1)$.
$\mathbf{R}_y$	Covariance of $\mathbf{y}$.
$\mathbf{S}$	L by M matrix whose columns are the steering vectors of the directional signal sources.
$\mathbf{s}_0$	Desired signal steering vector.
sgn()	Sign function.
$\mathbf{s}_i$	i^{th} source steering vector.
S_{ij}	The scattering matrix element determining the amount of signal transferred from port j to i when all other ports are matched.
$SINR_i$	Input signal to interference plus noise ratio.
SIR_i	Input signal to interference ratio.

SNR_i	Input signal to noise ration.
SNR_o	Output signal to noise ratio.
$\mathbf{T}$	L by $(M+1)$ matrix whose columns are the steering vector of the desired signal and the interference sources.
T	Sampling pulse train duration.
t_{inc}	The time delay increment in the time delay control IC.
t_{inh}	Inherent pulse width of the pulse width control IC.
tr(.)	Trace of a matrix.
T_s	Sampling period.
t_{sl}	Normalized time delay of the l^{th} element pulse train.
T_{tot}	Total convergence time of an adaptive algorithm.
T_w	Weighting period.
$\mathbf{u}(n)$	Random weight vector perturbation.
$\mathbf{v}(n+1)$	Weight vector in the $(n+1)^{th}$ iteration of the adaptive DOA estimation algorithm before normalization.
$\mathbf{V}$	M by M diagonal matrix whose diagonal elements are the powers of the signal sources.
V_γ	Forward bias voltage of the PIN diode.
$\mathbf{w}$	Array weight vector.
$\mathbf{w}(n)$	Array weight vector in the $(n+1)^{th}$ iteration.
$\mathbf{W}$	L by $(L+1)$ matrix whose columns are the $(L+1)$ weight vectors in the $(L+1)$ perturbation cycles.
$\mathbf{w}_1^-(n)$	First weight vector in the coherent perturbation algorithm.
W_1	Width of the 50Ω transmission line.
$\mathbf{w}_1^+(n)$	Second weight vector in the coherent perturbation.
$\bar{\mathbf{w}}(n)$	The average weight vector in the $(n+1)^{th}$ iteration.
$\hat{\mathbf{w}}$	Optimum weight vector with array signal estimation.
w_l^*	l^{th} antenna element weighting.
$\mathbf{w}_{\text{MSE}}$	Optimum weight vector for beamformer using reference signal.
$\mathbf{x}(t)$	Array signal vector.

$\mathbf{x}_1^-(n)$	Array signal in coherent perturbation algorithm when $\mathbf{w}_1^-(n)$ is applied.
$\mathbf{x}_1^+(n)$	Array signal in coherent perturbation algorithm when $\mathbf{w}_1^+(n)$ is applied.
$\hat{\mathbf{x}}(n+1)$	Estimated array signal vector in the $(n+1)^{th}$ iteration.
$\mathbf{x}_k(n+1)$	The array signal vector sampled at the end of the k^{th} perturbation cycle of $(n+1)^{th}$ iteration.
$x_l(t)$	l^{th} antenna element signal.
$X_l(f)$	Fourier transform of the l^{th} antenna element signal.
$x_{LO}(t)$	Local oscillator output signal.
$X_{ls}(f)$	Fourier transform of the l^{th} antenna element switch signal.
$x_o(t)$	The output of the I-Q vector modulator.
$y(t)$	Beamformer output.
$y(\mathbf{w}(n))$	Array output signal using a weight vector $\mathbf{w}(n)$.
$\mathbf{y}$	Vector consisting the *(L+1)* outputs of the array in the *(L+1)* perturbation cycles.
y_1^-	Beamformer output when $\mathbf{w}_1^-(n)$ is applied.
y_1^+	Beamformer output $\mathbf{w}_1^+(n)$ is applied.
$y_{\text{I}}(t)$	In phase output of the beamformer.
$y_k(n+1)$	The array output in the k^{th} perturbation cycle of the $(n+1)^{th}$ iteration.
$y_{\text{Q}}(t)$	Quadrature output of the beamformer.
$Z(f)$	Fourier transform of the mixer output signal.
$\mathbf{z}$	Correlation between the array signal and the reference signal.
$z(t)$	Mixer output signal.
Z_0	Characteristic impedance of the transmission line.
$\hat{\mathbf{z}}$	Correlation between the estimated array signal and the reference signal.
α	A parameter determining the effective width of the *sinc* function.
α_1, α_2	Transmission coefficient of the switch in two states.
β	A scalar determining the weighting duration in terms of signal bandwidth.
χ	A Scalar that depends on γ and $\rho^{(L)}$.

$\boldsymbol{\delta}(i)$	i^{th} perturbation sequence with size L in the orthogonal perturbation technique.
δ	Perturbation constant in DSD algorithm.
Δf	Array pattern bandwidth.
$\Delta \mathbf{w}_k(n)$	The perturbation vector in the k^{th} perturbation cycle of the $(n+1)^{th}$ iteration.
$\varepsilon(t)$	Error signal at the time instant t.
$\varepsilon(\mathbf{w}(n))$	Error signal using a weight vector $\mathbf{w}(n)$.
$\hat{\varepsilon}(\mathbf{w})$	The error signal using estimated array signal vector.
ε_r	Relative permittivity.
η	Perturbation factor in orthogonal perturbation technique.
γ	Perturbation factor in perturbation technique based on array signal estimation..
κ	Scalar quantity which depends on $\mathbf{R}_N, \mathbf{s}_0$, desired signal power, reference signal power, and χ.
κ_1	The scalar coefficient in the optimum weight vector based on maximum SINR criterion.
$\boldsymbol{\Lambda}$	L by L diagonal matrix whose diagonal elements are the eigenvalues of $\mathbf{R}$.
λ	Lagrange multiplier.
$\lambda(n)$	Array output power in the $(n+1)^{\text{th}}$ iteration.
$\lambda_{\max}$	Maximum eigenvalue of the covariance matrix.
$\lambda_{\min}$	Minimum eigenvalue of $\hat{\mathbf{R}}$.
$\boldsymbol{\Lambda}_n$	Diagonal matrix with M smallest eigenvalues of $\mathbf{R}$
$\boldsymbol{\Lambda}_s$	Diagonal matrix with M largest eigenvalues of $\mathbf{R}$.
λ_0	Free space wavelength.
λ_g	Wavelength inside the transmission line.
μ	Gradient step size.
$\mu(n)$	Variable gradient step size.
μ_0	Gradient step size for the DOA estimation algorithm.
$\nabla_{\mathbf{w}}\xi(\mathbf{w})$	Gradient of $\xi(\mathbf{w})$ versus $\mathbf{w}$.
ν	Number of time delay and pulse width bits.
φ_i	i^{th} source differential phase difference.
$\Pi(\cdot)$	Rectangular pulse.
$\rho_{ij}^{(q)}$	The temporal correlation coefficients of two

	samples of the j^{th} interference source which are qT_w apart.
$\rho_n^{(q)}$	The temporal correlation coefficients of two samples of the noise which are qT_w apart.
$\rho^{(q)}$	The correlation coefficient between the interference and noise samples which are qT_w apart.
σ^2	Variance of the random vector $\mathbf{u}(n)$.
σ_n^2	White noise variance.
$*$	Convolution operation.
$\tan\delta$	Loss tangent.
τ	Positive pulse width.
$\tau_l(\theta_i)$	Time delay for a wave arriving from θ_i measured on the l^{th} antenna element.
τ_l	Normalized positive pulse width of the l^{th} element pulse train.
τ_{lq}	Normalized positive pulse width of the l^{th} element pulse train which is quantized.
θ	Direction of the signal measured from the array axis.
θ_i	Direction of i^{th} impinging interference signal measured from the array axis.
$\xi(\mathbf{w})$	The mean square error.
$\hat{\xi}(\mathbf{w})$	The MSE using estimated array signal vector.
$\xi_{\min}$	Minimum mean square error.
$\hat{\xi}_{\min}$	Minimum mean square error using estimated array signal.
ζ	Null depth.
$(.)^{\text{H}}$	Hermitian of a matrix.
$(.)^{\text{T}}$	Transpose of a matrix.

Chapter 1

Introduction

1.1 Overview and Motivation

The overwhelming increase in the number of cellular communication users and services demands increasing the channel capacity. Based on the Shannon-Hartley capacity theorem, the channel bandwidth or the signal to noise ratio should be increased to increase the capacity [1]. However, a finite spectrum bandwidth is devoted to each application. Different spectrum allocation and coding techniques have been used to improve the spectral efficiency of the communication channel [2],[3]. Using multiple antennas in a wireless communication channel increases the capacity in different ways such as diversity combining [4], beamforming [5]-[8], space division multiple access [3],[5] and space time coding [5], [3], [9].

Steering beam antennas have been used for military applications since World War II in phased array radars to replace the huge mechanically rotated antennas. By using an array of antennas, each followed by a phase shifter, made it possible to rotate the array antenna beam electronically instead of by mechanical rotation [10]-[12]. Applications of phased arrays were limited to the military for years because of high implementation costs and lack of fast digital signal processor chips. However, phased arrays have been used recently in many commercial applications such as base stations in cellular communications, satellite communications, radio astronomy and bio-medication [13].

Using an antenna array as a beamformer directs the beam toward a desired user and introduces nulls in the directions of the directional interferences sources (DIS) or shape the pattern to receive the DIS in the low sidelobe region. Due to the DIS power

reduction by null-forming and/or sidelobe level (SLL) control and incoherent combination of the white noise, the signal to interference plus noise ratio (SINR) at the output of the beamformer improves. This SINR improvement increases the range and channel capacity. In addition, it is possible to communicate with users at the same frequency channel in the same cell, but in different angle sectors through space division multiplexing (SDMA)[3]. Therefore, higher number of users can be assigned to each frequency channel which increases the system capacity by frequency reuse.

One beamforming technique is the switched beamforming, where the beamformer switches to a finite number of beams and the beam with the highest output SINR is selected [3]. This technique benefits from low hardware complexity and simple signal processing. In particular, it can be implemented using passive beamforming networks in the RF domain. However because a finite number of beams is available, the beam nulls are not necessarily in the interference directions.

Another technique is adaptive beamforming that adapts itself dynamically to the channel variations. In this technique, the main beam is directed toward the desired signal and nulls are introduced in the DIS directions. Various adaptive beamforming algorithms, which are mostly suitable for digital beamforming (DBF), are available in the literature [6]. However, due to using multiple RF down-converters and analog to digital converters (ADC) in a DBF structure, it is not cost effective for commercial applications [16], [17]. In addition, due to the weighting and combining of signals in the digital domain and multiple inputs to the processor, DBF provides low throughput [18]-[21]. Moreover, integration of DBF structure with current cellular base stations as an add-on part requires major modifications in the whole system.

Another technique is microwave beamforming (MBF) where beamforming is carried out in the analog microwave domain using phase shifters and amplitude control elements [16]. This technique requires only one down-conversion and ADC circuit. However, there have been two problems associated with traditional MBF. One problem has been the lack of antenna elements' signals in the processor which prohibits using directly existing DBF algorithms for the MBF structures. Many efforts have been made to employ existing gradient-based adaptive beamforming techniques for MBF structures through perturbation techniques [22]-[30] . The major limitation in these techniques is the longer gradient estimation time. Another problem with the traditional MBF structures is the need for multiple RF weighting elements such as phase shifters and amplitude control elements which are the most expensive part of these systems.

1.2 Objectives

The main objective of this thesis has been to find techniques to reduce the hardware and signal processing complexity of beamforming. In addition, it considers both microwave and signal processing issues of the beamforming jointly into account. The focus of this research has been on the MBF structure because of its lower hardware complexity compared to the DBF structure. In particular, it investigates solutions for the two aforementioned problems of the MBF structure; complex microwave weighting elements and limitation in signal processing.

To address the first MBF problem, a new microwave beamforming structure: microwave sampling structure (MSBF) is devised. In this technique, amplitude control and phase shift are realized using fast switching of the antenna array signals. After each antenna element there is a simple switch which is driven by a control pulse train with

adjusted pulse width and time delay. By controlling the pulse width and time delay, amplitude and phase shift are controlled, respectively. One main advantage of this novel technique is that both high resolution phase shift and amplitude are controlled using one simple block. However, in this technique the signal bandwidth is limited by the switching speed of the switches. The new beamforming structure is verified by different simulations in time and frequency domains. Different issues of the MSBF structure such as switch design, finite pulse train, and image replica are investigated. A four-element microstrip antenna array with the new feeding network is constructed and the MSBF structure is verified experimentally. The implemented prototype is examined for different beamforming examples such as beam steering, SLL control, and null-forming.

To address the second problem, a new perturbation technique for a general MBF structure is developed. In this technique an estimation of the antenna array signal vector is found by fast perturbation of the antenna array signals. This estimated array signal vector is used for advanced signal processing operations such as adaptive beamforming and direction of arrival (DOA) estimation. Different simulations and analytical derivations show that adaptive beamforming and DOA estimation with the new perturbation technique can be superior to the algorithms with multi-port structures such as DBF structure, depending on the channel scenario.

1.3 Thesis Outline

In Chapter Two different beamforming issues are overviewed. First, beamforming fundamentals are presented. Then, adaptive beamforming and DOA estimation are briefly presented. Different beamforming structures are also overviewed. Next, electronically-controlled phase shifters and attenuators are discussed. Then, signal processing for

single-port structures such as MBF structure is overviewed. Finally, some issues such as mutual coupling, correlation and errors are briefly discussed.

In Chapter Three a new perturbation technique is proposed to integrate adaptive beamforming and DOA estimation with the MBF structure. The proposed algorithm is investigated under different scenarios. Different parameters of the adaptive algorithm such as gradient average, gradient variance, and misadjustment are studied analytically and with simulations. Effects of quantization errors on the algorithm performance are studied. In addition, an adaptive DOA estimation technique is presented and the results are compared with the MUSIC technique.

In Chapter Four, first the microwave sampling beamformer (MSBF) is introduced for the first time. Then, a switch design for MSBF structure is discussed. The whole structure is verified using microstrip and wire antenna arrays. Finally, the MSBF structure with finite pulse train duration and image replica is investigated.

In Chapter Five the results of the implemented MSBF structure prototype is presented. First, different RF and low frequency parts of the prototype are discussed. Then, the frequency and time domain simulations of the switch design are presented. Then the S-parameter measurement results are shown. Finally, the pattern measurement results are presented.

In Chapter Six a conclusion of the thesis and some suggestions for improvements and future work are presented. In addition, the contributions of the thesis are discussed.

Chapter 2

An Overview of Beamforming

2.1 Introduction

An antenna array is composed of multiple antenna elements distributed in space to produce a directional pattern. An antenna array using adaptive beamforming dynamically adjusts the antenna pattern to improve the signal to interference plus noise ratio. Typically, these systems use a phase shifter and an amplitude control element in each antenna branch to change the phase and amplitude of the received signal. The phase shift and amplitude gain are generally realized in microwave, intermediate frequency (IF), baseband, digital, or space domains. The optimum phase shift and amplitude for the array elements are obtained based on different criteria such as minimum output interference plus noise power, maximum output SINR, and minimum error between the beamforming output and a reference signal. When these optimum phase shifts and amplitude gains/attenuations are obtained adaptively based on the channel state information (CSI), the technique is called adaptive beamforming.

In this Chapter, several beamforming concepts are overviewed. In Section 2.2 beamforming fundamentals are presented. In Section 2.3 adaptive beamforming and DOA estimation are briefly overviewed. In Section 2.4 beamforming structures are presented. Electronically-controlled phase shifters and attenuators are presented in Section 2.5. In Section 2.6 signal processing for single-port structures are discussed. Finally, some antenna array issues such as mutual coupling, correlation and errors are briefly discussed in Section 2.7.

2.2 Beamforming Fundamentals

2.2.1 Terminology and signal model

Assume an L-element antenna array of omni-directional elements inside a homogeneous medium. The antenna array is assumed to be in the far field of M incoming signal sources $s_1(t), s_2(t), ..., s_M(t)$ with the same frequency f_0. It is assumed that these signals are impinging on the array from the same elevation angle, but from different azimuth directions $\theta_1, \theta_2, ..., \theta_M$ which are measured from the array axis. Without loss of generality, assume that all signals have the same elevation angle and that the antenna array is a linear array with element spacing d. Thus, the time taken by a plane wave arriving from a direction θ_i measured on the l^{th} antenna element is given by [6]

$$\tau_l(\theta_i) = \frac{d}{c}(l-1)\cos\theta_i \tag{2.1}$$

where c is the plane wave-front speed of propagation. The signal induced on the l^{th} antenna element can be written in the complex form as

$$x_l(t) = \sum_{i=1}^{M} m_i(t+\tau_l(\theta_i))e^{j2\pi f_0(t+\tau_l(\theta_i))} + n_l(t). \tag{2.2}$$

where $m_i(t+\tau_l(\theta_i))$ is the complex modulating signal on the l^{th} antenna element corresponding to the i^{th} source. This signal may be frequency division multiple access (FDMA), time division multiple access (TDMA), or code division multiple access (CDMA) signal [6]. $n_l(t)$ models the noise power received by the l^{th} antenna element which is a white noise signal with zero mean and variance σ_n^2.

When the modulating signal is narrowband and the size of the antenna array is not large, it can be assumed that $m_i(t+\tau_l(\theta_i)) \cong m_i(t)$ and (2.2) becomes

$$x_l(t) = e^{j2\pi f_0} \sum_{i=1}^{M} m_i(t) e^{j(l-1)k_0 d\cos(\theta_i)} + n_l(t) \tag{2.3}$$

where $k_0 = 2\pi f_0 / c$ is the wave number in the free space and $n_l(t)$ is the noise received by the l^{th} antenna element. Using (2.3), the antenna array signal vector $\mathbf{x}(t) = [x_1(t), x_2(t), ..., x_L(t)]^{\mathrm{T}}$, where $[.]^{\mathrm{T}}$ represents transpose of a matrix, can be expressed in vector form by

$$\mathbf{x} = e^{j2\pi f_0 t} \sum_{i=1}^{M} m_i(t)\mathbf{s}_i + \mathbf{n}(t) \tag{2.4}$$

where

$$\mathbf{s}_i = [1, e^{j\varphi_i}, ..., e^{(L-1)\varphi_i}]^{\mathrm{T}} \tag{2.5}$$

and $\varphi_i = k_0 d\cos\theta_i$ are the steering vector and the differential phase difference corresponding to the i^{th} source, respectively.

Figure 2.1 shows a simple beamformer structure where each element is multiplied by a complex weight vector. The output of the beamformer is expressed by

$$y(t) = \sum_{l=1}^{L} w_l^* x_l(t) \tag{2.6}$$

which $(.)^*$ denotes complex conjugate operation. It is generally preferred to express (2.6) in matrix form by $y(t) = \mathbf{w}^{\mathrm{H}}\mathbf{x}(t)$ where $\mathbf{x}(t)$ is the array signal vector given by (2.4) and

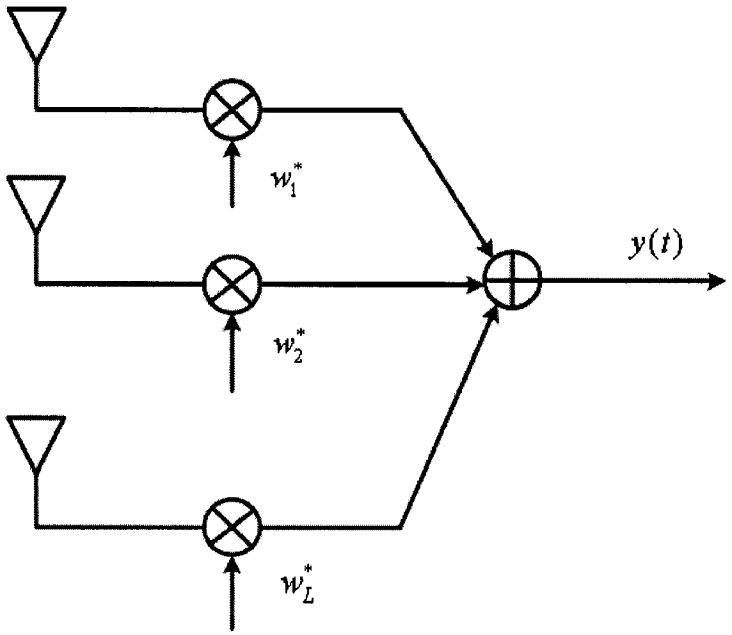

Figure 2.1 Narrowband element space processing beamformer.

$\mathbf{w} = [w_1, w_2, ..., w_L]^T$ is the array weight vector. The array average output power is given by [6]

$$\begin{aligned} P(\mathbf{w}) &= E[yy^*] \\ &= \mathbf{w}^H \mathbf{R} \mathbf{w} \end{aligned} \tag{2.7}$$

where $E[.]$ denotes expectation operation and $\mathbf{R} = E[\mathbf{x}(t)\mathbf{x}^H(t)]$ is the array correlation matrix. The array correlation matrix can be expressed in terms of the powers and the steering vectors of the incident signals on the array by [6]

$$\mathbf{R} = \sum_{i=1}^{M} p_i \mathbf{s}_i \mathbf{s}_i^H + \sigma_n^2 \mathbf{I} \tag{2.8}$$

where p_i and $\mathbf{s}_i$ are the power and the steering vector of the i^{th} source, respectively.

Now, assume that there is one desired signal with power p_S and M interference sources in the channel. Then, based on (2.8) , $\mathbf{R}$ may expressed in different forms by [6]

$$\begin{aligned}\mathbf{R} &= p_S\mathbf{s}_0\mathbf{s}_0^{\mathrm{H}} + \sum_{i=1}^{M} p_i\mathbf{s}_i\mathbf{s}_i^{\mathrm{H}} + \sigma_n^2\mathbf{I} \\ &\triangleq p_S\mathbf{s}_0\mathbf{s}_0^{\mathrm{H}} + \mathbf{R}_N \\ &\triangleq \mathbf{R}_S + \mathbf{R}_N\end{aligned} \tag{2.9}$$

In (2.9), $\mathbf{s}_0$, $\mathbf{R}_S$, and $\mathbf{R}_N$ are the steering vector of the desired signal, the correlation matrix of the desired source, and the correlation matrix of the interference plus noise, respectively. Based on (2.8) and (2.9), the signal and noise plus interference output powers are given by

$$p_{SO} = \mathbf{w}^{\mathrm{H}}\mathbf{R}_S\mathbf{w} \tag{2.10}$$

and

$$p_{NO} = \mathbf{w}^{\mathrm{H}}\mathbf{R}_N\mathbf{w}\,, \tag{2.11}$$

respectively. Therefore, the output signal to interference plus noise ratio for this beamformer can be written by

$$\begin{aligned}\mathrm{SINR}_O &= \frac{p_{SO}}{p_{NO}} \\ &= \frac{\mathbf{w}^{\mathrm{H}}\mathbf{R}_S\mathbf{w}}{\mathbf{w}^{\mathrm{H}}\mathbf{R}_N\mathbf{w}}.\end{aligned} \tag{2.12}$$

Most beamforming algorithms directly or indirectly maximize the SINR_O as shown in the next sections.

2.2.2 Element space processing

Figure 2.1 shows an element space processing beamforming structure where antenna elements signals are combined after multiplying by some adjustable weights. Weighing of signals can be carried out in different domains; microwave, intermediate frequency (IF), baseband, digital and space domains. In addition, these weights can be predefined and stored as in switched beamforming or can be found adaptively as in adaptive beamforming. In switched beamforming, there are a finite number of weight vectors among which the system processor selects one that achieves the maximum SNR or lowest BER. In adaptive beamforming, weights are calculated dynamically based on the channel dynamic situations. These weights are obtained based on different schemes, some of which are discussed in this section.

2.2.2.1 Conventional beamformer

Assume that there is only one desired signal and white noise in the channel. In a conventional beamformer, the weights are selected to have unity power response in the direction of the desired signal. In fact the weight vector is given by

$$\mathbf{w} = \mathbf{s}_0 \tag{2.13}$$

where $\mathbf{s}_0$ is the steering vector corresponding to the desired signal direction of arrival (DOA). In this beamformer, ignoring the losses in the system, the signal output power is L times the input power but the output noise power is equal to input noise power. Therefore, it provides a SNR gain equal to the number of antennas which is the maximum realizable SNR gain when no directional interference is present.

2.2.2.2 Null-steering beamformer

In a null-steering beamformer the beamformer cancels several plane waves impinging from known directions and directs the main beam toward the desired signal. Assume that a desired signal with steering vector $\mathbf{s}_0$ and M interference sources are impinging on the array. The null forming weight vector is calculated based on the unity power reception in the direction of the desired signal given by

$$\mathbf{w}^{\mathrm{H}}\mathbf{s}_0 = 1 \tag{2.14}$$

and zero power reception in the interference sources directions with steering vectors $\mathbf{s}_i, i = 1,2,..,M$ given by

$$\mathbf{w}^{\mathrm{H}}\mathbf{s}_i = 0, \quad i = 1,2,...,M\,. \tag{2.15}$$

When $M = L-1$, the weight vector that satisfy (2.14) and (2.15) is calculated using

$$\mathbf{w}^{\mathrm{H}} = \mathbf{e}_1^{T}\mathbf{T}^{-1} \tag{2.16}$$

where, $\mathbf{T} \triangleq [\mathbf{s}_0, \mathbf{s}_1, ..., \mathbf{s}_M]$ and $\mathbf{e}_1 = [1,0,...,0]^{\mathrm{T}}$. When $M < L-1$, the weight vector is calculated using pseudo inverse by [6]

$$\mathbf{w}^{\mathrm{H}} = \mathbf{e}_1^{\mathrm{T}}\mathbf{T}^{\mathrm{H}}(\mathbf{T}\mathbf{T}^{\mathrm{H}})^{-1}\,. \tag{2.17}$$

This beamformer cancels the interference sources in the absence of errors such as mutual coupling. In particular, it is effective in cancelling strong interferences with known directions. However, it needs the direction of the interference sources and does not control the white noise power [6]. Therefore the output SNR is not maximized.

2.2.2.3 Optimal minimum power beamformer

The optimal minimum power beamformer minimizes the output interference plus noise power while keeping the gain of the array in the desired signal direction fixed, i.e. unity. Mathematically, the output interference plus noise power ($p_{NO} = \mathbf{w}^{H}\mathbf{R}_{N}\mathbf{w}$) should be minimized subject to the constraint

$$\mathbf{w}^{H}\mathbf{s}_{0} = 1 \tag{2.18}$$

which can be solved using the method of Lagrange multipliers. It can be shown that the optimum weight vector is given by

$$\mathbf{w} = \frac{\mathbf{R}_{N}^{-1}\mathbf{s}_{0}}{\mathbf{s}_{0}^{H}\mathbf{R}_{N}^{-1}\mathbf{s}_{0}} \tag{2.19}$$

which maximizes the output SINR in the absence of errors.

As can be seen, this approach does not require knowledge of the directions and power levels of the interference sources as well of the background noise to maximize SNR. It just requires the direction of the desired signal. One problem in (2.19) is that $\mathbf{R}_{N}$ is not accessible in the receiver. Therefore, in practice the total array correlation $\mathbf{R}$ matrix is used:

$$\mathbf{w} = \frac{\mathbf{R}^{-1}\mathbf{s}_{0}}{\mathbf{s}_{0}^{H}\mathbf{R}^{-1}\mathbf{s}_{0}}. \tag{2.20}$$

The weight vector in (2.20) is the solution of the optimization problem that minimizes the total output signal power ($\mathbf{w}^{H}\mathbf{R}\mathbf{w}$) while constrained for unity response in the direction of the desired signal ($\mathbf{w}^{H}\mathbf{s}_{0} = 1$). In addition, it can be shown that the weight vector in (2.19) is equal to the one in (2.20) [6].

2.2.2.4 Optimal maximum SINR beamformer

The weight vector may be calculated to directly maximize the SINR using

$$\nabla_{\mathrm{w}} \frac{\mathbf{w}^{\mathrm{H}}\mathbf{R}_S\mathbf{w}}{\mathbf{w}^{\mathrm{H}}\mathbf{R}_N\mathbf{w}} = \mathbf{0} \tag{2.21}$$

where SINR from (2.12) is used. It can be shown that the optimum weight vector is given by [13]

$$\mathbf{w} = \kappa_1 \mathbf{R}_N^{-1}\mathbf{s}_0 \tag{2.22}$$

Where κ_1 is a scalar which depends on the steering vector of the desired signal, the optimum weight vector, the power of the desired signal, and the output SINR [13]. Therefore, the maximum SINR criterion gives the same weight vector as minimum output power up to a multiplicative constant.

2.2.2.5 Optimal beamformer using a reference signal

A block diagram of the beamformer using reference signal is shown in Figure 2.2 [6]. In this beamformer, which is based on Wiener filtering [14], a reference signal is used to obtain the optimum weight vector. In fact, the optimum weight vector is obtained through minimization of the mean square error (MSE) between the reference signal and the received signal when the reference signal is given to the channel. With a reference signal $r(t)$, the error signal is calculated by $\varepsilon(t) = r(t) - \mathbf{w}^{\mathrm{H}}\mathbf{x}(t)$ and the MSE is given by

$$\begin{aligned} \xi(\mathbf{w}) &= E\left[\left|\varepsilon(t)\right|^2\right] \\ &= E\left[\left|r(t)\right|^2\right] + \mathbf{w}^{\mathrm{H}}\mathbf{R}\mathbf{w} - \mathbf{w}^{\mathrm{H}}\mathbf{z} - \mathbf{z}^{\mathrm{H}}\mathbf{w} \end{aligned} \tag{2.23}$$

where, $\mathbf{z} = E\left[\mathbf{x}(t)r^*(t)\right]$. The gradient of $\xi(\mathbf{w})$ versus the weight vector is given by

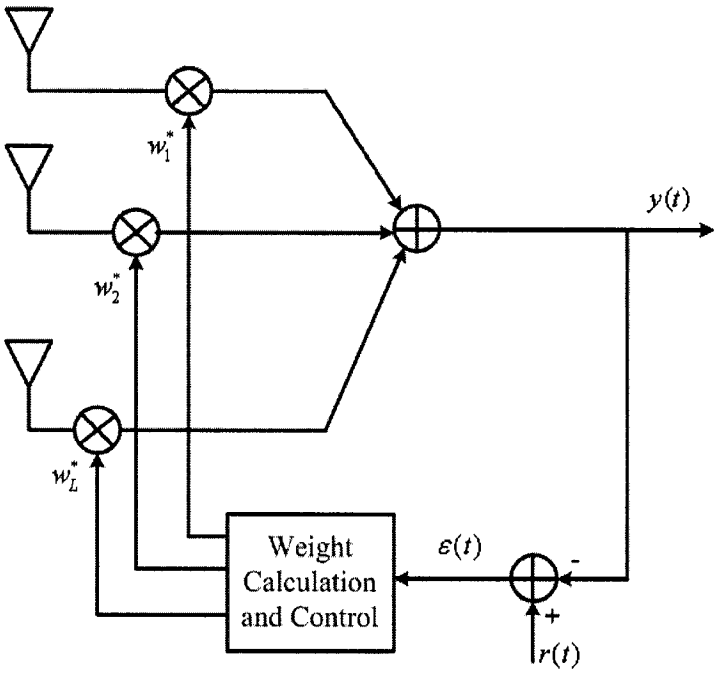

Figure 2.2 Optimum beamformer using a reference signal [6].

$$\nabla_w \xi(\mathbf{w}) = 2\mathbf{R}\mathbf{w} - 2\mathbf{z}. \tag{2.24}$$

Upon minimizing MSE in (2.23) by equating (2.24) to zero, the optimum weight vector is given by

$$\mathbf{w}_{\text{MSE}} = \mathbf{R}^{-1}\mathbf{z} \tag{2.25}$$

and the minimum mean square error (MMSE) is given by

$$\xi_{\min} = E\left[|r(t)|^2\right] - \mathbf{z}^{\text{H}}\mathbf{R}^{-1}\mathbf{z}. \tag{2.26}$$

Using $\mathbf{R} = p_S \mathbf{s}_0 \mathbf{s}_0^{\text{H}} + \mathbf{R}_N$, it can be shown that

$$\mathbf{R}^{-1} = \left[\frac{1}{1 + p_S \mathbf{s}_0^{\text{H}} \mathbf{R}_N^{-1} \mathbf{s}_0}\right] \mathbf{R}_N^{-1} \tag{2.27}$$

and $\mathbf{z} = E\left[\mathbf{x}(t)r^*(t)\right] = p_S\mathbf{s}_0$. Therefore, the optimum weight vector in **(2.25)** can be written as

$$\mathbf{w}_{\text{MSE}} = \frac{p_S}{1 + p_S\mathbf{s}_0^{\text{H}}\mathbf{R}_N^{-1}\mathbf{s}_0}\mathbf{R}_N^{-1}\mathbf{s}_0 \ . \tag{2.28}$$

Therefore, the weight vector for this beamformer has the same form as that of the last two optimal beamformers. An advantage of the Wiener method is that mutual coupling does not affect its performance compared to techniques that use steering vectors such as optimum beamformer based on maximum SNR and the null forming beamformer.

2.2.3 Beam space processing

In a beam space processing beamformer a main beam is directed towards the desired signal and a set of auxiliary beams in the directions of the interference sources. The pattern of the main beam is called quiescent pattern which can be uniform, Chebyshev, Taylor, etc... . Auxiliary beams are designed to have no signal by generating a beam with a null in the signal direction, subtracting two beams, and generating orthogonal beams. In all these schemes the secondary beams are combined and the summation is subtracted from the main beam to find an output. The mean output power is minimized to maximize the SINR. In this method, presence of the desired signal in the secondary beams results in signal cancellation. There are different structures for beam space processing such as the optimal beam space processor, generalized sidelobe canceller, and post-beamformer interference canceller [6]. These beamformers work more effectively than element space processing when there are steering vector errors.

2.2.4 Narrowband and wideband beamforming

Beamforming structures are generally classified as narrowband or wideband which is considered in the design of smart antenna systems. If the transmission bandwidth is more than one percent of the center frequency the system is wideband, otherwise the system is narrowband [31]. There are different bandwidth definitions for a wireless system such as antenna impedance bandwidth, transceiver bandwidth and antenna array pattern bandwidth. Here, the focus is on array pattern bandwidth and it is assumed that antenna impedance and receiver bandwidths are sufficient for transmission and reception of the signals.

The array pattern bandwidth refers to the signal variations received by different antenna elements. If signals are narrowband enough, signals received by different antenna elements are delayed versions of each other and there is no amplitude variation. This assumption was made in the derivation of (2.3) from (2.2). When signals are wideband, this assumption is no longer true. In fact, time variation of the signal is so fast that during the arrival time differences of the signals on different antenna elements the modulating signal also changes.

For narrowband applications in each antenna element one weight is applied as shown in Figure 2.1. In fact, each element's time delay is modeled with a frequency independent complex weight which is calculated at the center frequency. In wideband applications a constant weight can not compensate the changes in the signal. In one method, a tapped delay line or transversal filter is used in each antenna element which has multiple weights and time delays. This technique is suitable when weights are applied in the digital domain. Another approach which is implemented in microwave domain, is

to use true time delay (TTD) phase shifters. However, TTD phase shifters are generally more complex, more expensive and bulkier than the simple phase shifters [9]-[12].

2.3 Adaptive Beamforming and DOA Estimation

2.3.1 Adaptive beamforming

There are many different adaptive beamforming algorithms in the literature. Some adaptive algorithms need a training sequence or the steering vector of the desired signal for adaptation, but there are blind algorithms that do not need any direct information. In blind algorithms, some properties of the signal such as constant amplitude or cyclo-stationarity are used to find the weights.

Some of the most common algorithms are sample matrix inversion (SMI) [6], unconstrained least mean square (ULMS) and constrained least mean square (CLMS) [6], recursive least squared (RLS) [6], constant modulus algorithm (CMA) [29], modified constant modulus (MCMA) [29], conjugate gradient algorithm (CGA) [6], and maximum cross correlation (MCC) algorithm [32]. Each algorithm performance is evaluated based on convergence speed, steady state error, misadjustment, and implementation complexity. A full discussion of the adaptive algorithms is out of the scope of this work. In this part, two most common algorithms, ULMS and CLMS, are briefly discussed.

2.3.1.1 Unconstrained least mean square (ULMS)

ULMS algorithm is the adaptive implementation of the optimum beamformer using reference signal or Wiener filtering. The algorithm minimizes the error between the training sequence and the output of the beamformer adaptively. The weight vector update

equation is given by

$$\mathbf{w}(n+1) = \mathbf{w}(n) - \mu\mathbf{g}(\mathbf{w}(n)) \tag{2.29}$$

where $\mathbf{w}(n)$ is the antenna array weight in the n^{th} iteration, μ is the gradient step size, and $\mathbf{g}(\mathbf{w}(n))$ is the gradient of the error power versus the weight vector $\mathbf{w}(n)$ given by

$$\mathbf{g}(\mathbf{w}(n)) = -2\mathbf{x}(n+1)\varepsilon^*(\mathbf{w}(n)). \tag{2.30}$$

In (2.30), $\mathbf{x}(n+1)$ is the array signal vector in the $(n+1)^{th}$ iteration and $\varepsilon(\mathbf{w}(n))$ is the error signal given by

$$\varepsilon(\mathbf{w}(n)) = r(n+1) - \mathbf{w}^H(n)\mathbf{x}(n+1) \tag{2.31}$$

where $r(n+1)$ is the training sequence in the $(n+1)^{th}$ iteration. The advantage of this algorithm is its simplicity, but the algorithm has some flaws with its convergence and its convergence rate is slow. For this algorithm to converge, the gradient step size should satisfy the condition $0 \le \mu \le 1/(2\lambda_{\max})$ where $\lambda_{\max}$ is the maximum eigen-value of the array signal covariance matrix $\mathbf{R}$.

An important property of the gradient-based adaptive algorithms is the gradient average. The average of the gradient in (2.30) is given by

$$\bar{g}(\mathbf{w}(n)) = 2\mathbf{R}\mathbf{w} - 2\mathbf{z} \tag{2.32}$$

which is equal to the gradient of MSE in (2.24). Therefore, the gradient estimation is an unbiased estimation. Beside the gradient average, the gradient covariance affects the algorithm's performance. The gradient covariance is defined by

$$\mathrm{cov}(\mathbf{g}(\mathbf{w}(n)) = E\{[\mathbf{g}(\mathbf{w}(n)) - \bar{\mathbf{g}}(\mathbf{w}(n))][\mathbf{g}(\mathbf{w}(n)) - \bar{\mathbf{g}}(\mathbf{w}(n))]^{\mathrm{H}}\}. \tag{2.33}$$

After few iteration cycles, the gradient average can be ignored and the gradient covariance at a point close to the optimum point is given by [6]

$$\text{cov}(\mathbf{g}(\mathbf{w}(n)) = 4\xi_{\min}\mathbf{R} \tag{2.34}$$

where $\xi_{\min}$ is given by (2.26).

In order to measure the performance of an adaptive algorithm the misadjustment is generally used which is defined by [6]

$$MA = \lim_{n\to\infty} \frac{\xi(\mathbf{w}(n)) - \xi_{\min}}{\xi_{\min}} \tag{2.35}$$

where,

$$\xi(\mathbf{w}(n)) = E\{|\,(r(n) - \mathbf{w}^{\mathrm{H}}(n)\mathbf{x}(n+1)\,|^2\} \tag{2.36}$$

which is the error between the training sequence and the output of the beamformer in each iteration. It can be shown that the misadjustment factor for ULMS algorithm is given by

$$MA = \mu tr\{[\mathbf{I} - \mu\mathbf{R}]^{-1}\mathbf{R}\} \tag{2.37}$$

which is reduced to $MA = \mu tr\{\mathbf{R}\}$ for small μ values. There are different forms of the ULMS algorithm depending on the choice of the gradient step size and the way the correlation matrix is formed [6].

2.3.1.2 Constrained least mean square (CLMS)

This algorithm is the adaptive implementation of the optimum beamformer based on SNR maximization. In this algorithm it is assumed that the desired signal direction is known but no training signal is required for this algorithm. The algorithm minimizes the total output power and keeps the direction of the main beam toward the desired signal direction. The update equation for CLMS algorithm is expressed by

$$\mathbf{w}(n+1) = \mathbf{P}\{\mathbf{w}(n) - \mu\mathbf{g}(\mathbf{w}(n))\} + \mathbf{s}_0 / L \tag{2.38}$$

where $\mathbf{w}(n)$ is the antenna array weight vector in the n^{th} iteration, μ is the gradient step size, $\mathbf{s}_0$ is the steering vector of the desired signal, and **P** is given by

$$\mathbf{P} = \mathbf{I} - \frac{\mathbf{s}_0\mathbf{s}_0^{\mathrm{H}}}{L}. \tag{2.39}$$

$g(\mathbf{w}(n))$ is the gradient of the output power versus the weight $\mathbf{w}(n)$ given by

$$\mathbf{g}(\mathbf{w}(n) = 2\mathbf{x}(n+1)y^*(\mathbf{w}(n)) \tag{2.40}$$

where

$$y(\mathbf{w}(n)) = \mathbf{w}^{\mathrm{H}}(n)\mathbf{x}(n+1) \tag{2.41}$$

is the output of the beamformer output. The gradients step size for this algorithm should be small enough to satisfy $\mu < 1/\lambda_{\max}$ where, $\lambda_{\max}$ is the maximum eigenvalue of **PRP**. This algorithm is faster than ULMS, but the steady state signal to noise ratio is less than that of ULMS algorithm.

2.3.2 DOA estimation

Another application of the antenna arrays is DOA estimation where the direction of the signal impinging on the array is estimated using a processor. There are numerous applications for DOA estimation. One application is to find the direction of the desired user which is used for CLMS adaptive beamforming. In null steering beamformer directions of the interference sources and the desired signal are obtained by DOA estimation. In addition, in space division multiple access (SDMA) the direction of different users in a cell should be estimated in the base station to direct different beams

toward different users. Moreover, for emergency situations the location of the people with a cell phone can be found using DOA estimation. Furthermore, DOA estimation may be used to estimate the flow of traffic by tracking a user with a cell phone.

There are many different DOA estimation techniques [6], [7],[33]. One class of methods is spectral techniques which are based on scanning the beam direction and estimating the maxima of the spatial spectrum. However, these methods' resolution is proportional to the beamwidth of the array. Therefore, for small arrays, the angle resolution is low. Another class of DOA estimation methods is based on eigen-structure of the array which is generally called high resolution techniques. One of the most common techniques in this category is multiple signal classification (MUSIC) which is studied in this thesis.

2.3.2.1 Spectral MUSIC technique

Assume that there are M directional sources and white noise in the communication channel. The array correlation matrix $\mathbf{R}$ can be written as a function of directional signals power and steering vectors and noise power by (2.8) which may be written in matrix form by

$$\mathbf{R} = \mathbf{S}\mathbf{V}\mathbf{S}^{\mathrm{H}} + \sigma_n^2\mathbf{I} \tag{2.42}$$

where columns of the matrix $\mathbf{S}$ are the steering vectors of the directional sources and $\mathbf{V}$ is a diagonal matrix whose diagonal elements are equal to the directional source powers.

The correlation matrix may be also written in terms of the eigenvalues and eigenvectors by

$$\mathbf{R} = \mathbf{E}^{\mathrm{H}}\mathbf{\Lambda}\mathbf{E} \tag{2.43}$$

where $\mathbf{\Lambda}$ is a diagonal matrix whose diagonal elements are the eigenvalues of $\mathbf{R}$ arranged in descending order. $\mathbf{E}$ is a square matrix whose columns are the corresponding eigenvectors of the eigenvalues in $\mathbf{\Lambda}$. The eigenvalues can be divided in two sets of noise and signal eigenvalues. There are M signal eigenvalues whose values depend on the number of sources and source powers, source steering vectors. There are L-M noise eigenvalues which are all equal to the noise power. Because the eigenvectors of $\mathbf{R}$ form an orthonormal set, it becomes

$$\begin{aligned}\mathbf{R} &= \mathbf{E}_s\mathbf{\Lambda}_s\mathbf{E}_s + \mathbf{E}_n\mathbf{\Lambda}_n\mathbf{E}_n \\ &= \mathbf{E}_s\mathbf{\Lambda}_s\mathbf{E}_s + \sigma_n^2\mathbf{I}\end{aligned} \tag{2.44}$$

where $\mathbf{E}_s$and $\mathbf{\Lambda}_s$ are signal eigenvector and eigenvalue matrices, formed similar to $\mathbf{E}$ and $\mathbf{\Lambda}$, respectively. Likewise, $\mathbf{E}_n$, and $\mathbf{\Lambda}_n$ are noise eigenvector and eigenvalue matrices. Based on (2.42) and (2.44), $\mathbf{SVS}^{\mathrm{H}} = \mathbf{E}_s\mathbf{\Lambda}_s\mathbf{E}_s^{\mathrm{H}}$. Multiplying both sides by $\mathbf{E}_n$ becomes

$$\begin{aligned}\mathbf{SVS}^{\mathrm{H}}\mathbf{E}_n &= \mathbf{E}_s\mathbf{\Lambda}_s\mathbf{E}_s^{\mathrm{H}}\mathbf{E}_n \\ &= \mathbf{0}\end{aligned} \tag{2.45}$$

which is because $\mathbf{E}_n$ and $\mathbf{E}_s$ are orthogonal. Thus,

$$\mathbf{S}^{\mathrm{H}}\mathbf{E}_n = \mathbf{0} \tag{2.46}$$

which means, the noise sub-space is normal to the steering vectors of the directional sources. Therefore for any channel, first the noise sub-space is found and then the steering vectors that are normal to noise sub-space are obtained. The MUSIC spectrum is given by

$$P_{MU}(\theta) = \frac{1}{\left|\mathbf{s}^{\mathrm{H}}(\theta)\mathbf{E}_n\right|^2} \tag{2.47}$$

where $\mathbf{s}(\theta)$ is a steering vector in the direction θ. The angles θ that maximize $P_{MU}(\theta)$ are the direction of incident signals. The MUSIC spectrum given by (2.47) is spectral MUSIC. There are other forms of MUSIC [6],[7],[33] such as root-MUSIC, constrained MUSIC, and beam-space MUSIC.

2.4 Beamforming Structures

An important issue about beamforming is the domain that weight vector is applied to the array. The choice of the domain affects the smart antenna structure in hardware and signal processing. In this section some of the most well-known beamforming structures are reviewed. For each structure the benefits and drawbacks from RF and signal processing point of views are discussed.

2.4.1 Digital beamforming (DBF)

Figure 2.3 shows a digital beamforming structure. In this structure one full receiver composed of BPF, LNA, mixer, LPF and ADC, is used for each antenna element. As can be seen in

Figure 2.3 the beamforming weights are applied in the digital signal processor (DSP) after RF down-conversion and analog to digital conversion (ADC). An important feature of this structure is that advanced signal processing operations such as adaptive beamforming, direction of arrival (DOA) estimation, multi-beam performance, and etc. [13] can be integrated with the structure, thanks to availability of fast DSP chips. In a DBF structure the signal samples from all antennas are stored after ADCs. To apply the weight vectors, the signal samples are shifted by multiples of the sampling period. To increase the weighting resolution, the sampling frequency should be much higher than the Nyquist rate or digital interpolation is used

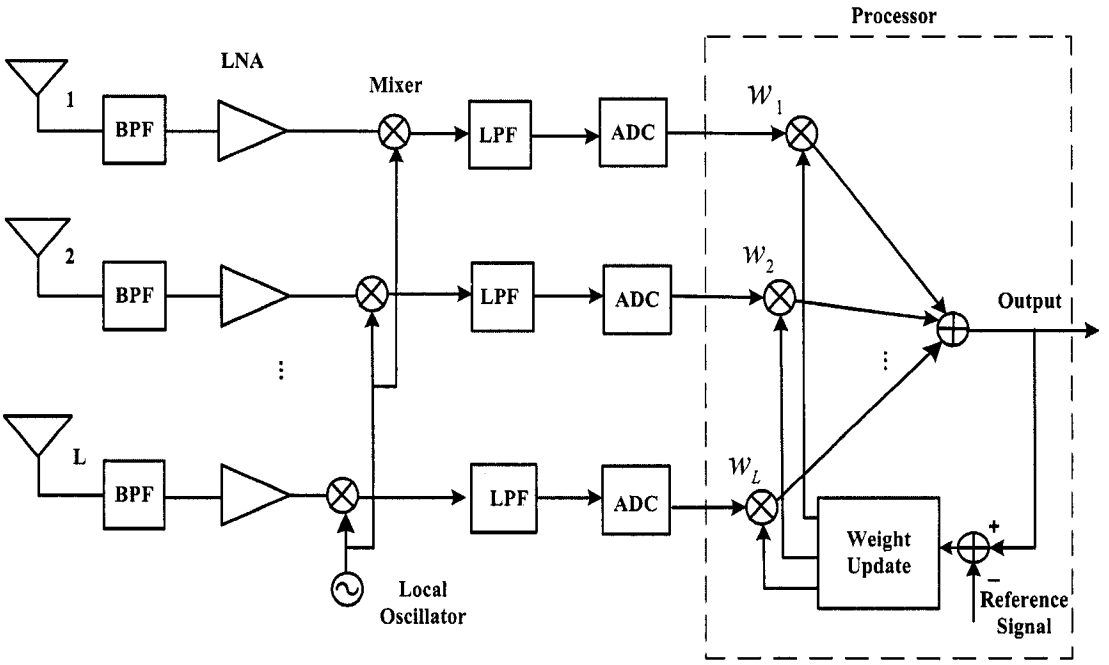

Figure 2.3 A digital beamforming structure.

[34]-[37]. In [38],[39] digital beamforming is used for ultrasonic imaging.

Despite aforementioned advantages of the DBF structure, there are some major disadvantages that limit their commercial applications. First, due to using one full receiver per antenna element the implementation cost of the smart antenna system is N-fold. This problem has limited the application of the DBF structure to military applications [16]. Second, the throughput is limited because multiple signals should be transferred to DSP in parallel [18]-[21]. Though the processing speed of the DSPs is quite high, their I/O data transfer rates are very limited. In particular, the maximum total data that are transferred from all ports are limited. Therefore, by increasing the number of antennas this problem becomes more stringent. Third, there are quantization errors due to weighting and combining of signals after conversion to digital [16]. This problem reduces

the dynamic range of the beamforming structure which prohibits making deep nulls for interference cancellation. To improve this problem, high resolution ADCs should be used which further increases the implementation cost. In addition, high resolution ADCs demand high DC power which is not desirable for mobile battery dependent users [16].

2.4.2 Microwave beamforming (MBF)

Figure 2.4 shows a microwave beamforming (MBF) structure where antenna elements are weighted in the microwave domain using phase shifters and or gain or attenuation control elements. In [40], the whole MBF structure is integrated using monolithic microwave integrated circuit (MMIC) technology. The optimum weights are obtained digitally in the processor. One problem with the MBF structure is the need for one phase shifter and amplitude control element per antenna. Another problem is the lack of the antenna array signal vector in the processor which makes it impossible to use advanced signal processing such as ABF and DOA estimation directly. However, the overall hardware complexity is lower than the DBF structure. In addition, due to transferring only one signal to the processor, higher throughput is feasible. Moreover, for many cellular applications it is desirable to add beamforming to the existing base stations instead of changing the whole system. For these add-on applications it is preferred to add an MBF structure to an existing system because only the beamforming part needs to be exchanged. MBF structures using true time delay phase shifters have recently been of interest for ultra-wideband (UWB) beamforming applications because of their broadband weighting. In [41], [42], integrated phased arrays for UWB applications are constructed using true time delay phase shifting.

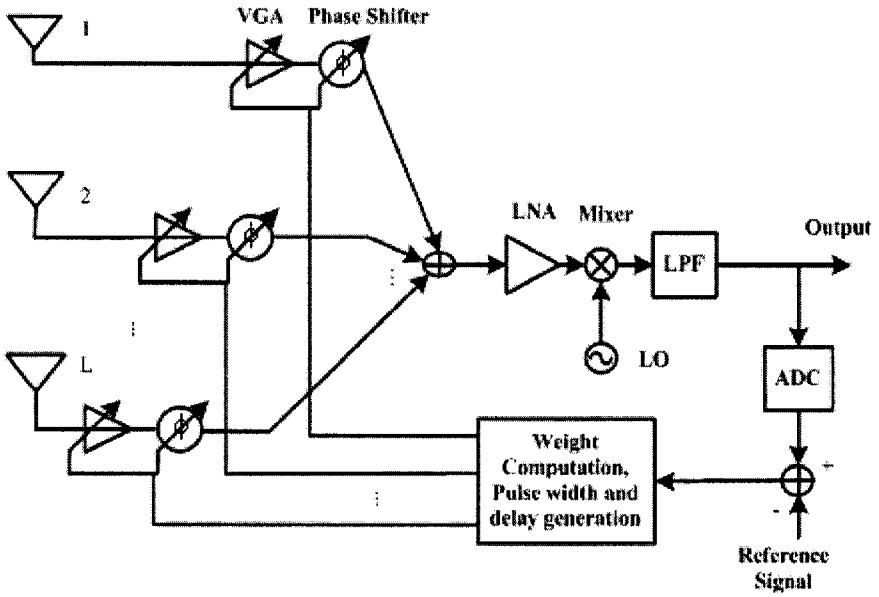

Figure 2.4 A microwave beamforming structure.

2.4.3 Local beamforming (LBF)

In local beamforming, phase shifters are located in the local oscillators rather than in the direct RF branches [43],[44]. Phase shifters may be located in the RF or IF local oscillators. The main advantage of this structure is removing the effects of phase nonlinearities in the phase shifters by passing a signal with constant amplitude and phase. Variable amplifiers in the RF or IF domains are used for amplitude control. The main drawback of this structure is that multiple down-conversion circuits should be employed which increases the cost of the structure. Furthermore, when the phase shifters and variable amplifiers are realized in the IF domain, the system bandwidth is limited due to lowering the center frequency of these circuits. In [45],[46] a local beamforming structure is integrated in silicon.

2.4.4 Hybrid analog-digital beamforming

The hybrid analog-digital beamforming structure is proposed to increase the data throughput of the DBF structure [18]-[21]. In this technique, for the purpose of weight calculation, the signals of different antennas are sampled in the IF domain with a data rate which can be lower than the Nyquist rate. Therefore, DSPs with lower I/O data rate can be used. In practice, the time variant property of the channel determines the sampling rate. This technique is efficient for slow fading channels where the speeds of the mobile units are not very high. In this technique, the weight vector is applied to the antenna array in the analog IF domain. In [47] a new beamforming structure is proposed which applies the weight vector in the IF domain, but a single output is transferred to the processor. Despite the throughput improvement similar to DBF structure, for each branch separate RF amplification and downconversion stages are employed.

2.4.5 Electrically steerable parasitic array radiator (ESPAR)

ESPAR beamforming is based on electromagnetic coupling between antenna elements [47]-[54]. In this structure one active element is surrounded by some parasitic elements which are loaded with adjustable loads such as varactor diodes. Upon changing the adjustable loads with DC control voltages, the elements' currents change, which modify the induced voltages in the main element through mutual coupling. Therefore, by adjusting the parasitic elements currents the pattern of the antenna can be adjusted to maximize the SINR. The main advantage of this structure is its low complexity. However, there are some limitations in this structure compared to a general MBF structure. First, the weight resolution is lower than a system that uses a general MBF

structure. Second, due to reception and amplification of the signals with only one element the dynamic range is lower than that of an MBF structure. This becomes more serious when the antenna is employed in the transmit mode where all the system power should be handled by one element.

2.4.6 Spatially multiplexing of local elements (SMILE) structure

In an SMILE structure, signals of different antenna elements are sampled in the microwave domain and downconverted to IF or baseband sequentially [55]. In this technique the sampling rate should be more than the signal transmission bandwidth multiplied by the number of antennas to avoid aliasing effects. The downconverted signals are separated using a demultiplexer block and are converted to digital signals. These digital signals are weighted, combined and processed in the digital domain using a digital processor. In this structure, in each time interval only one antenna is ON and the rest are OFF. In [56] an SMILE structure using series feed is presented. In [57] an SMILE is presented which uses switching amplifiers instead of PIN diodes to solve the low output power problem. In [58] the location of switches in the SMILE structure are adjusted to control the mutual coupling.

The advantage of this structure is the possibility of using advanced digital signal processing algorithms due to availability of all antenna signals in the receiver. However, due to having only one active antenna in this structure the total output power is at most equal to the power received by one antenna. Furthermore, the SMILE structure cannot be used in the transmit mode fundamentally. There are also problems with fall time of PIN diodes and the matching of combiners with antennas which distorts the detected signal.

2.4.7 Optical beamforming

Optical beamforming is similar to MBF, but beam weighting and combining are carried out in the optical domain [5]. Received signals over antenna elements are converted to optical signals using electrical to optical converters such as laser diodes and the optical signals are carried using optical fibers. After weighting and combining the signals in the optical domain, the optical signals are converted to electrical signals using optical to electrical converters such as avalanche diodes or PIN diodes. This structure has low loss, low weight, and radio frequency interference (RFI) immunity that make it suitable for applications that antenna elements and the receiver are far from each other [16]. In addition, due to the higher center frequency, higher bandwidth can be achieved. However, the implementation cost of this structure is high. Several optical beamforming techniques are presented in [59]-[61].

2.5 Electronically-Controlled Phase Shifters and Attenuators

2.5.1 Phase shifters

A phase shifter modifies the phase of the RF input signal by a certain amount. Phase shifters may be fixed or variable, but variable phase shifters are desired for phased arrays. A variable phase shifter may be controlled mechanically, electrically or magnetically [62]. Phase shifters are classified as analog or digital phase shifters. In analog phase shifters the phase shift changes continuously using a control voltage or current. Generally a varactor diode is used as a voltage-controlled capacitor to change the phase shift. Digital phase shifters have discrete phase values which are achieved by switching between different blocks. Each block may be a section of transmission line, a component, or a filter. These phase shifters are more common because of immunity of

control voltage to the noise. A digital phase shifter is determined by the number of phase bits. For a ν bits phase shifter there is 2^{ν} phase states. The highest order bit is 180°, the next bit is 90°, the next 45° and so on.

There are different phase shifter designs such as switched delay line, loaded line, reflection type, I-Q vector modulator, switched filter, ferrite type and etc. An overview of different phase shifters designs may be found in [59], [62],[63]. The I-Q vector modulator has been attractive because of its low complexity and possibility of integrating both phase shift and amplitude tapering in one block. In [64]-[67] I-Q vector modulator are used to implement low cost beamforming.

2.5.2 Time delay or phase scanning

Phase shifters may be also classified as simple phase shifters and true time delay (TTD) phase shifters. In a phased array the time delay between elements should be compensated which can be done by TTD phase shifters. However, TTD phase shifters are used for broadband phased arrays. A simple phase shifter can model the time delay over a narrow frequency band. When frequency changes, the required phase shifts change, but a simple phase shifter is fixed. Therefore, the beam direction changes by changing frequency, or beam squinting happens. The array bandwidth defined by the frequency range that the array power is reduced to the half power beamwidth point is given by [9]

$$\frac{\Delta f}{f} = 0.866 B_b \left(\frac{\lambda}{(L-1)d \sin\theta_0} \right) \tag{2.48}$$

where, B_b is beam broadening factor which is unity for uniform amplitude distribution. Therefore, the amount of beam squinting increases as the size of the array increases. A

rule of thumb relation between the 3-dB bandwidth and 3-dB beamwidth is that bandwidth in percent is equal to two times the beamwidth in degrees [9].

Design of a beamformer for wideband nulling is even more challenging. In fact, the main beam direction is frequency-independent, but the null locations and depths are frequency-dependent. It can be shown that if nulls are to be deeper than $-\zeta$, then the null bandwidth is limited to [5]

$$B_N = \frac{10^{-\zeta/10}}{2^{2L-1}} . \tag{2.49}$$

Therefore, deeper nulls and larger arrays lower the null bandwidth. This issue should be considered if wideband interference sources are to be mitigated.

2.5.3 Attenuators

Attenuation can be created by using a proper resistive network. In order to modify the attenuation electronically, PIN diodes or field effect transistors (FET) may be used in place of the resistors. A PIN diode is different from a PN junction by having a thin layer of intrinsic (I) semiconductor between the P and N layers. The addition of this layer decreases the junction capacitance by increasing the distance between the P and N regions. It also makes PIN conductivity a linear function of the diode bias current. This is due to the injection of charge carriers in the intrinsic region which is proportional to the bias current. Therefore, the PIN diode resistance will be inversely proportional to the bias current. In an FET transistor, when the voltage difference between the drain and source is zero, the channel resistance can be controlled by the gate voltage [68] .

Therefore, in an attenuator made of a resistive network one or more resistors are replaced by FET transistors or PIN diodes to control the attenuation electronically. FET

transistors are generally preferred to PIN diodes for monolithic microwave integrated circuit (MMIC) design, but PIN diodes are preferred for hybrid microwave integrated circuit (HMIC) design. There are different types of attenuator circuits which are classified as reflective and matched attenuators. In a matched attenuator input and output ports are kept matched for different attenuation levels. An overview of different attenuator designs is given in [62].

2.6 Signal Processing for Single-Port Structures

Most signal processing operations such as adaptive beamforming and DOA estimation are devised for multi-port structures where array signal vector is available in the processor. The array signal vector is used in the processor to estimate the gradient vector or array correlation matrix. However, in some beamforming structures such as MBF, LBF, and ESPAR structures, only one signal which is the beamformer output is transferred to the processor. In order to apply advanced signal processing operations to the single-port structures, perturbation techniques are used. In any perturbation technique the gradient vector or array correlation matrix are estimated by perturbing the array weight vector and recording multiple outputs. In this section, several most common techniques are discussed.

2.6.1 *Differential steepest descent (DSD)*

For a beamforming algorithm based on a training signal the mean square error is given by (2.23). In the steepest decent algorithm, the optimum solution of (2.23) is obtained adaptively by [68]

$$\mathbf{w}(n+1) = \mathbf{w}(n) - \mu(\nabla_{\mathbf{w}(n)}\xi(\mathbf{w}(n)) \tag{2.50}$$

where n is the iteration number, μ is the gradient step size, and $\nabla_{\mathbf{w}(n)}\xi(\mathbf{w}(n)$ is the gradient of $\xi(\mathbf{w}(n))$ in (2.23) versus the weight vector which is given in (2.24). In order to implement (2.50), the gradient vector should be estimated. Calculating the gradient vector using (2.24) requires estimating **R** and **z** which is complex with a single-port structure.

In the DSD algorithm, the gradient vector is estimated in $2L$ perturbation cycles using numerical differentiation and direct measurements. For example, with a present weight vector $\mathbf{w}(n)=[w_1(n), w_2(n), ..., w_L(n)]$, the first element of the gradient vector is calculated using

$$\frac{\partial \xi}{\partial w_1} \cong \frac{\xi(w_1+\delta, w_2, ..., w_L)-\xi(w_1-\delta, w_2, ..., w_L)}{2\delta} . \qquad (2.51)$$

In each perturbation cycle N samples may be recorded for averaging. Therefore, for estimating each element of the gradient vector $2N$ measurements are needed. It is shown in [68] that the perturbation error in estimating the gradient vector with this method is given by

$$P=\frac{\delta^2}{\xi_{\min}}\frac{tr(\mathbf{R})}{L} \qquad (2.52)$$

where $tr(.)$ is the trace function and $\xi_{\min}$ is the minimum error when perfect gradient estimate is used. As can be seen in (2.52) the perturbation error is proportional to the square of the weight perturbation δ. In [68], different parameters of the algorithm such as gradient measurement noise, weight vector noise and misadjustment are studied

thoroughly. In particular, it is shown that the misadjustment for the algorithm due to noisy weight vector is given by

$$MA = \frac{\mu L \xi_{\min}}{4N\delta^2} \tag{2.53}$$

which is inversely proportional to the square of the weight perturbation. This is in contrast to the perturbation error in (2.52). The total misadjustment is given by $MA_{tot} = MA + P$ which takes into account both perturbation error and weigh vector variance.

2.6.2 ***Random search***

In the random search algorithm the weight vector is perturbed by a random perturbation vector. If the error is improved, the new weight vector is recorded, otherwise another random vector is tried. The weight update equation for this algorithm is given by [68]

$$\mathbf{w}(n+1) = \mathbf{w}(n) + \frac{1}{2}\left[1 + \operatorname{sgn}\left\{\xi(\mathbf{w}(n)) - \xi(\mathbf{w}(n) + \mathbf{u}(n))\right\}\right]\mathbf{u}(n) \tag{2.54}$$

where $\mathbf{u}(n)$ is a random perturbation vector and $\xi(\mathbf{w}(n))$ is an estimation of the MSE through averaging over N samples of error and sgn(.) is the sign function. One problem with this algorithm is that only those weight vectors plus random perturbation vectors that decrease the MSE are recorded [68]. Therefore, nothing is learned by the algorithm from the bad random changes. Linear random search (LRS), another variation of RS algorithm, is proposed in [68] whose update equation is expressed by

$$\mathbf{w}(n+1) = \mathbf{w}(n) + \mu[\xi(\mathbf{w}(n)) - \xi(\mathbf{w}(n) + \mathbf{u}(n))]\mathbf{u}(n)\,. \tag{2.55}$$

In this algorithm, $\mathbf{u}(n)$ is a random vector generated to have a covariance matrix $\sigma^2\mathbf{I}$ with σ a design constant. Because the variation in the weight vector is proportional to the change in the MSE, this algorithm is called linear random search (LRS). A detailed analysis of this algorithm can be found in [68] which is out of the scope of this thesis. In particular, the normalized perturbation error and misadjustment are derived in [68] which are given by

$$P = \frac{\sigma^2 tr(\mathbf{R})}{2\xi_{\min}} \tag{2.56}$$

and

$$MA = \frac{\mu L}{N}\xi_{\min} \ . \tag{2.57}$$

As can be seen, the perturbation error is proportional to the variance of the random noise vector used for the weight perturbation.

2.6.3 Gradient estimation using orthogonal perturbation sequences

In this method, in each iteration cycle of the adaptive algorithm the gradient vector is estimated in *4L* perturbation cycles. In [22], this gradient estimation method is proposed for the CLMS algorithm. As discussed in sub-section 2.3.1.2, the weight vector update equation for the CLMS algorithm is given by (2.38). Because the array signal vector is not accessible, the gradient vector can not be calculated directly. In [22] an estimation of the gradient vector is obtained by

$$\mathbf{g}(\mathbf{w}(n)) = \frac{1}{4\eta L}\sum_{i=1}^{4L} y_i(n) y_i^*(n)\boldsymbol{\delta}(i) \tag{2.58}$$

where

$$y_i(n) = \mathbf{w}_i^{\mathrm{H}}(n)\mathbf{x}(n) \tag{2.59}$$

and

$$\mathbf{w}_i(n) = \mathbf{w}(n) + \eta\boldsymbol{\delta}(i)\,. \tag{2.60}$$

In (2.58) and (2.60) $\boldsymbol{\delta}(i)$ is the i^{th} perturbation sequence which has a size L which is chosen form a complex orthogonal set $S = \{\boldsymbol{\delta}(1), \boldsymbol{\delta}(2), ..., \boldsymbol{\delta}(4L)\}$ [22]. It is shown in [22] that when set S has odd symmetry, the gradient estimation is unbiased. The set S has odd symmetry if for any $\boldsymbol{\delta}(i)$ in S, there is an $\boldsymbol{\delta}(j) = -\boldsymbol{\delta}(i)$. In addition, it is shown in [22] that the perturbation error power is given by

$$P = 2\eta^2 tr[\mathbf{R}]\,. \tag{2.61}$$

Other modifications of this technique are presented in [22] which uses two receivers or two receivers with a reference receiver. Another modification of this technique is presented in [25] that uses less number of perturbation sequences. A detailed performance analysis of this algorithm is carried out in [26],[27].

2.6.4 Coherent perturbation algorithm

This algorithm is based on the temporal correlation of the antenna array signals. In this method, the gradient vector is estimated sequentially in $2L$ perturbation cycles [23]. Assume the array weight vector in the n^{th} iteration to be $\mathbf{w}(n) = [w_1, w_2, ..., w_L]^{\mathrm{T}}$. Two weight vectors $\mathbf{w}_1^+(n) = [w_1 + \Delta w_1, w_2, ..., w_L]^{\mathrm{T}}$ and $\mathbf{w}_1^-(n) = [w_1 - \Delta w_1, w_2, ..., w_L]^{\mathrm{T}}$ are applied to the array in a short period of time to estimate the first element of the gradient vector. The outputs of the array with these weight vectors are given by $y_1^+(n) = \mathbf{w}_1^+(n)\mathbf{x}_1^+(n)$ and $y_1^-(n) = \mathbf{w}_1^-(n)\mathbf{x}_1^-(n)$ where, $\mathbf{x}_1^+(n)$ and $\mathbf{x}_1^-(n)$ are the array

signals when two weight vectors are applied. Then, the first element of the gradient vector is estimated by

$$g_1 = \frac{(y_1^+ - y_1^-)(y_1^+ + y_1^-)^*}{2\Delta w_1^*} \quad . \tag{2.62}$$

Other elements of the gradient vector can be calculated in the same manner. The fundamental limitation of this technique is that the two outputs should be recorded in a short time interval to increase the temporal correlation between the array signal samples. When temporal correlation increases, it can be assumed that $\mathbf{x}_1^+(n) = \mathbf{x}_1^-(n)$ and the gradient estimate in (2.62) approaches the gradient estimate using multi-port structures. However, this requires fast weighting of the array signals which is limited by the switching speed of the devices used in the phase shifters and attenuators. A detailed analysis of this algorithm is presented in [23].

2.6.5 Other algorithms

There are several adaptive beamforming and DOA estimation algorithms that are developed for the ESPAR structure [47]-[51]. In these algorithms it is assumed that a training sequence which is fixed during different perturbation cycles exists in the channel. For DOA estimation it is assumed that every signal source in the channel has a training signal that is fixed during different perturbation cycles. In most perturbation algorithms the gradient vector or array covariance matrix are estimated in $L+1$ perturbation cycles. However, in [47] a perturbation technique is proposed which estimates the gradient vector in two perturbation cycles.

There are some other algorithms that are devised for structures that use phase shifters alone. In [70] a nonlinear adaptive algorithm is developed through output power

maximization that adjusts the phase shifters. This algorithm does not require any training signal or steering vectors. In [71] this algorithm is extended for interference and fading reduction. In [30] two gradient-based phase only algorithms are developed. In these algorithms, the phase shifter values are updated instead of weight vectors. One algorithm is non-coherent phase perturbation which does not make any assumption about the rate that phase shifts are applied. The other technique is based on coherent perturbation technique which requires fast perturbation. Another phase only algorithm is developed in [28],[29] which is based on constant modulus algorithm. In this method, the output of the beamformer is also controlled using a variable gain amplifier. In each iteration cycle, both the phase shift values and the gain of this amplifier are updated using two updated equations. In general algorithms using phase shift alone are slower than algorithms that use both amplitude and phase shift control.

2.7 Mutual Coupling, Errors and Calibration

2.7.1 Mutual coupling

When antenna elements are close to each other, there is some mutual coupling between elements which changes the current distribution of each element compared to a single element. This current variation modifies the input impedance and radiation pattern of the antennas. Each antenna element input impedance changes with the scan angle and the antenna array resonant frequency is shifted. In particular, at some scan angles scan blindness may happen [11]. The radiation pattern is affected through some increase in sidelobe level and some variation in the beamwidth. Mutual coupling level differs from one type of antenna to another, but by increasing the distance between antennas the effects are reduced.

Mutual coupling affects the performance of beamforming and DOA estimation algorithms. The effects of mutual coupling on the performance of adaptive beamforming are investigated in [8], [72]-[75]. In [76], [77] the SNR optimization is investigated by including the mutual coupling effect. This mutual coupling effect originates from the dependence of beamforming and DOA estimation algorithms on the steering vectors. A steering vector is generally defined by assuming uniform amplitude distribution and linear progressive phase shift between elements. However, this assumption is not the case when there is strong mutual coupling between elements. Therefore, in beamforming algorithms that require steering vectors of the signals such as null-forming beamformer or CLMS algorithm, the calculated beamforming weights are erroneous. Similarly, for DOA estimation algorithms which are based on steering vectors such as spectral MUSIC, the DOA estimation is erroneous. In [78], [79] electromagnetic (EBG) materials are used to reduce the mutual coupling. Several mutual coupling compensation techniques methods are proposed in [80]-[83].

The effect of mutual coupling can be reduced by increasing array spacing. However, increasing array spacing form half wavelength can lead to grating lobes which is not desired. In addition, increasing the array spacing reduces the spatial correlation of signals on different antenna elements. However, for beamforming applications the antenna elements signals should be fully correlated. Moreover, it is generally desired to decrease the size of the array. Therefore, for a beamforming system on one side the element spacing should be increased for mutual coupling reduction and on the other side it should be decreased to have enough correlation, to avoid grating lobes and to decrease array size.

2.7.2 Errors

There are many different errors in smart antenna system. Errors originate from hardware imperfection and failure, processor limitations and simplifying assumptions. Hardware errors are due to errors in phase shifters, amplifiers, matching circuits, combiners, ADCs, DACs and so on. In a phased array antenna, the combined effects of the errors deviates the phase and amplitude of the weights in each element from ideal case. The phase error decreases the array gain, increases the sidelobe level (SLL) and lowers the pointing accuracy [9]. The main effect of amplitude errors is SLL increase [9]. In a DBF structure, quantization errors exist in the ADCs and DACs. On the other hand, in an MBF structure, there are quantization errors in the phase shifters and attenuators. Element failure can happen for any of the active components partially or totally. Processor errors are due to discrete and finite word lengths which happen through quantization and truncation errors.

In [84] the effect of errors on adaptive weights are studied. In [85], the effect of finite weight resolution on the performance of beamforming is studied. In [86] , the effect of phase shifter errors on adaptive beamforming is investigated. In [87] the effect of element failure in an active phased array is investigated and an iterative technique is proposed to remove the effects based on the Fourier transform relation between the array pattern and the excitations.

2.7.3 Calibration

As discussed in last two sub-sections, there are errors and mutual coupling in a beamforming system. In practice, it is tried to reduce the error sources and mutual coupling in the design process. However, there are some errors that can not be removed

totally and their effects should be compensated by calibration. Calibration may be carried out either off-line or on-line. Off-line calibration refers to measurement of different smart antenna components such as antennas, transmission lines, active components etc. in the design process. These measurement results are recorded and considered in the processor in the weight vector calculations. On-line calibration is generally used to compensate for the variation in the system during its normal operation. For example active components drifts and temperature variations degrade the system performance. Calibration is an important phase of the smart antenna design and there are many online and off-line calibration techniques available in the literature [80]-[83], [89]-[91].

2.8 Conclusion

An overview of beamforming was presented in this chapter to build a background for the next chapters. Beamforming fundamentals such as beamforming methodology, element-space, beam-space, and bandwidth were presented first. Then, adaptive beamforming and DOA estimation was briefly discussed. Afterwards, different methods to implement beamforming were presented. The microwave beamforming (MBF) structure as the main focus of this thesis was discussed with more detail. In this regard, phase shifters and attenuators as the main component in the MBF structure were discussed. In addition, signal processing for the single-port structures which is used for the MBF structure was presented. Finally, different nonideal issues such as mutual coupling, spatial correlation, and errors were discussed briefly.

Chapter 3

Single-Port Adaptive Beamforming and DOA Estimation

3.1 Introduction

In this chapter a new perturbation technique for single-port adaptive beamforming and DOA estimation is presented. The proposed technique is based on estimation of the array signal vector by making the array signal vector temporally correlated. Some variations of this technique are presented in [92]-[96]. The algorithm is studied in different scenarios with unconstrained least mean square (ULMS) algorithm. It is observed that the single-port algorithm achieves higher SINR gain than other single-port techniques and even multi-port algorithms. Moreover, the convergence speed of the new algorithm is much faster than other single-port structures and very close to the corresponding algorithms with multi-port structures. Moreover, compared to other single-port algorithms this algorithm converges with higher gradient step size which makes the convergence rate even faster.

A new single-port direction of arrival (DOA) estimation technique using adaptive null-forming is proposed. This technique is based on adaptive minimization of the array output power. The array weights are perturbed sequentially to find the array covariance matrix in each iteration cycle. A new LMS-like adaptive algorithm is developed for the DOA estimation. The proposed single-port structure is compared with the multiple signal classification (MUSIC) and single-port beam space multiple signal classification (SPBS-MUSIC) techniques. It is observed that the proposed technique can be superior to the MUSIC depending on the SNR level.

In Section 3.2 the new perturbation technique is introduced. In Section 3.3, the perturbation technique is applied to the optimal beamformer using a reference signal. In Section 3.4, the perturbation technique is applied to the adaptive ULMS algorithm. Adaptive beamforming simulation results and discussions are presented in Section 3.5. In Section 3.6 the single-port DOA estimation is introduced. DOA estimation simulation results are presented in Section 3.7. Finally, the summary and conclusions are given in Section 3.8.

3.2 New Perturbation Technique

In this technique, in each iteration cycle $L+1$ perturbations are used to obtain an approximation of the array signal vector. Suppose the computed weight vector by the adaptive algorithm in the n^{th} iteration is $\mathbf{w}(n)$. Then, the perturbed weight vector in the k^{th} perturbation cycle of the $(n+1)^{\text{th}}$ iteration is given by

$$\mathbf{w}_k(n) = \mathbf{w}(n) + \Delta\mathbf{w}_k(n), \qquad k = 1,2,...,L+1 \tag{3.1}$$

where, $\Delta\mathbf{w}_k(n)$ is the perturbation vector in the k^{th} perturbation cycle. The array output at the k^{th} perturbation cycle of the $(n+1)^{\text{th}}$ iteration is given by

$$y_k(n+1) = \mathbf{w}_k^{\mathrm{H}}(n)\mathbf{x}_k(n+1) \tag{3.2}$$

where, the superscript $(.)^{\mathrm{H}}$ denotes the conjugate transpose or Hermitian of an array. $\mathbf{x}_k(n+1)$ represents the array signal vector sampled at the end of the k^{th} perturbation cycle, which is given by

$$\mathbf{x}_k(n+1) = \mathrm{m}_s((n+k)T_w)\mathbf{s}_0 + \sum_{j=1}^{N_I} \mathrm{m}_{ij}((n+k)T_w)\mathbf{s}_j + \mathbf{n}((n+k)T_w) \tag{3.3}$$

where, T_w is the time spacing between different weighting intervals. Here, it is assumed that the sampling rate is equal to the weighting rate. In (3.3), $m_s((n+k)T_w)$ is the desired signal, $\mathbf{s}_0$ is the desired signal steering vector, $m_{ij}((n+k)T_w)$ and $\mathbf{s}_j$ are the j^{th} interference source and its steering vector, and $\mathbf{n}((n+k)T_w)$ is the Gaussian white noise on the antenna array. In order to find a proper estimation of the array signal vector, array signal estimation $\hat{\mathbf{x}}(n+1)$ is obtained by choosing $\Delta\mathbf{w}_1 = \mathbf{0}$, $\Delta\mathbf{w}_2 = [\Delta w_1, 0, ..., 0]^T$, and $\Delta\mathbf{w}_{L+1} = [\Delta w_1, \Delta w_2, ..., \Delta w_{L-1}, \Delta w_L]^T$. With these perturbations, the approximate array signals are obtained sequentially by

$$\hat{x}_k = \frac{y_{k+1} - y_k}{\Delta w_k^*}, k = 1,2,...,L \tag{3.4}$$

which decreases the computational burden on the processor. It is shown later by different simulations that variable perturbations work better than fixed perturbations. In particular, with $\Delta w_k = \gamma w_k$ and proper values for γ, the algorithm converges very well. Using $\Delta w_k = \gamma w_k$, (3.4) may be written in matrix form as $\hat{\mathbf{x}} = \mathbf{A}\mathbf{y}$, where $\mathbf{A}$ is given by

$$\mathbf{A}(i,j) = \begin{cases} -1/(2\gamma w_i^*), & j = i, \\ 1/(2\gamma w_i^*), & j = i+1, \\ 0, & otherwise \end{cases} \qquad 1 \le i \le L,\ 1 \le j \le L+1. \tag{3.5}$$

It is shown in the next subsection that an optimum value for γ is -2. In addition, with $\gamma = -2$, no calculation of the updated weights in each perturbation cycle is required and weights are perturbed by just inverting the elements weights phases sequentially. Therefore, the variable perturbation and specifically $\gamma = -2$ lowers the computational burden of the processor and simplifies the beamforming control hardware. Besides choos-

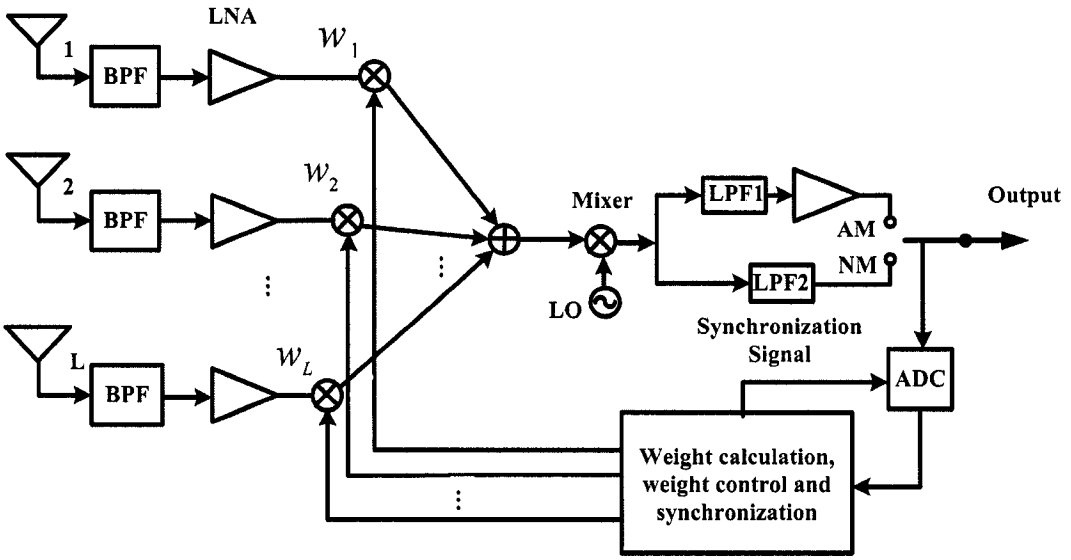

Figure 3.1 Single-port MBF structure with new perturbation technique.

-ing proper perturbation vectors, the signal samples in different perturbation cycles should be temporally correlated. Temporal correlation is related to the signal bandwidth and the sample spacing. Consider a white noise signal which is band-limited to a transmission bandwidth B_T. If the weighting rate is $f_w = 1/T_w$, the correlation coefficient between the samples which are qT_w apart ($\rho^{(q)}$) is given by

$$\rho^{(q)} = \text{sinc}(qT_wB_T). \tag{3.6}$$

Therefore, by increasing the weighting rate and decreasing the noise bandwidth B_T, correlation coefficient increases. In practice, the weighting rate is limited by the switching time of the semiconductor devices which limits the maximum achievable signal bandwidth. Another way to increase the temporal correlation is by lowering the LPF bandwidth. Based on (3.6) , lowering B_T increases $\rho^{(q)}$. Filtering the antenna array output signal modifies the temporal variation of the output signal. However, for

narrowband applications it does not change the spatial nature of the signal which is important for adaptive beamforming and DOA estimation. In Figure 3.1, two different LPFs are used in the normal mode (NM) and adaptation mode (AM). However, by lowering the LPF bandwidth, the signal, noise and interference power levels are reduced. For the output signal to be in the dynamic range of the ADC, a simple baseband amplifier should be used in the output of the LPF which is shown in Figure 3.1.

3.2.1 Optimization using a reference signal

In this part, the optimization problem using a reference signal and the new perturbation technique is investigated. The mean square error to be minimized is given by

$$\hat{\xi}(\mathbf{w}) = E[|\hat{\varepsilon}(\mathbf{w})|^2] \tag{3.7}$$

where

$$\hat{\varepsilon}(\mathbf{w}) = r - \mathbf{w}^{\mathrm{H}}\hat{\mathbf{x}}. \tag{3.8}$$

$\hat{\mathbf{x}}$ and r are the estimated array signal vector in the processor and the reference signal, respectively. For a multi-port structure the array signal vector is available in the processor which is used in determining the error signal. However, for the single-port structure, the estimated array signal vector is used. In addition, it is assumed that the desired signal during different perturbation cycles is the same. Expanding (3.7), it can be shown that

$$\hat{\xi}(\mathbf{w}) = E[|r|^2] - \mathbf{w}^{\mathrm{H}}\hat{\mathbf{z}} - \hat{\mathbf{z}}^{\mathrm{H}}\mathbf{w} + \mathbf{w}^{\mathrm{H}}\hat{\mathbf{R}}\mathbf{w} \tag{3.9}$$

where, $\hat{\mathbf{z}} = E\{\hat{\mathbf{x}}r^*(n+1)\}$ and $\hat{\mathbf{R}} = E\{\hat{\mathbf{x}}\hat{\mathbf{x}}^{\mathrm{H}}\}$. Here, $\hat{\mathbf{R}} = E[\hat{\mathbf{x}}\hat{\mathbf{x}}^{\mathrm{H}}] = \mathbf{A}\mathbf{R}_y\mathbf{A}^{\mathrm{H}}$ where the covariance matrix $\mathbf{R}_y = E[\mathbf{y}\mathbf{y}^{\mathrm{H}}]$ is given by

$$\mathbf{R}_y(i,j) = \mathbf{w}_i^{\mathrm{H}}\mathbf{R}_{\mathbf{x}}^{(q)}\mathbf{w}_j, \quad L+1 \le i,j \le L+1, \quad q = |i-j| \tag{3.10}$$

and

$$\mathbf{R}_x^{(q)} = E[\mathbf{x}_k \mathbf{x}_{k+q}^{\mathrm{H}}] \tag{3.11}$$

which is expanded to

$$\mathbf{R}_x^{(q)} = P_s \mathbf{s}_0 \mathbf{s}_0^{\mathrm{H}} + \sum_{j=1}^{N_j} \rho_{ij}^{(q)} P_j \mathbf{s}_j \mathbf{s}_j + \rho_n^{(q)} \sigma_n^2 \mathbf{I}. \tag{3.12}$$

In (3.12), P_S, P_j and σ_{n}^2 are the powers of the desired signal, the j^{th} interference source, and the noise in each antenna element, respectively. $\rho_{ij}^{(q)}$ and $\rho_n^{(q)}$ are the temporal correlation coefficients of two samples of the j^{th} interference source and the noise, respectively, which are spaced by q samples. The correlation coefficients depend on the noise and interference bandwidth, the bandpass filter (BPF) frequency response and the weighting rate. Assuming the interference bandwidth for all sources are equal and for the worst case, assume that the interference bandwidth is higher than or equal to the filter bandwidth, (3.12) may be rewritten as

$$\mathbf{R}_x^{(q)} = P_s \mathbf{s}_0 \mathbf{s}_0^{\mathrm{H}} + \rho^{(q)} (\sum_{j=1}^{N_j} P_j \mathbf{s}_j \mathbf{s}_j + \sigma_n^2 \mathbf{I}) = P_s \mathbf{s}_0 \mathbf{s}_0^{\mathrm{H}} + \rho^{(q)} \mathbf{R}_{\mathrm{N}}. \tag{3.13}$$

Using the fact that $\mathbf{R} = P_s \mathbf{s}_0 \mathbf{s}_0^{\mathrm{H}} + \mathbf{R}_{\mathrm{N}}$, where, $\mathbf{R}_{\mathrm{N}}$ is the covariance matrix of the noise plus interference, $\mathbf{R}_x^{(q)}$ is simplified to

$$\mathbf{R}_x^{(q)} = \begin{cases} \mathbf{R}, & q = 0 \\ \mathbf{R} + (\rho^{(q)} - 1)\mathbf{R}_{\mathrm{N}}, & q \neq 0 \end{cases} \tag{3.14}$$

Therefore, $\mathbf{R}_y$ is given by

$$\mathbf{R}_y = \mathbf{W}^{\mathrm{H}} \mathbf{R} \mathbf{W} + \mathbf{R}_e \tag{3.15}$$

where

$$\mathbf{R}_e(i,j)=\begin{cases}0, & i=j\\ (\rho^{(|i-j|)}-1)\mathbf{w}_i^{\mathrm{H}}\mathbf{R}_N\mathbf{w}_j, & i\neq j\end{cases} \qquad 1\le i,j\le L+1\,. \tag{3.16}$$

By increasing the correlation coefficients in (3.16), $\mathbf{R}_e$ approaches a null matrix. For this purpose, the output array signals through the BPF are sampled with a rate higher than the BPF or signal bandwidth. Using (3.15) and (3.16), the optimization equation in (3.9) is expressed by

$$\hat{\xi}(\mathbf{w})=E[|r|^2]-\mathbf{w}^{\mathrm{H}}\hat{\mathbf{z}}-\hat{\mathbf{z}}^{\mathrm{H}}\mathbf{w}+\mathbf{w}^{\mathrm{H}}\mathbf{R}\mathbf{w}+\mathbf{w}^{\mathrm{H}}\mathbf{A}\mathbf{R}_e\mathbf{A}^{\mathrm{H}}\mathbf{w}\,. \tag{3.17}$$

For stationary channels it can be shown that $\hat{\mathbf{z}}=\mathbf{z}=E[\mathbf{x}r^*(n+1)]$ and

$$\mathbf{w}^{\mathrm{H}}\mathbf{A}\mathbf{R}_e\mathbf{A}^{\mathrm{H}}\mathbf{w}=\frac{2(\gamma+1)}{\gamma^2}(1-\rho^{(L)})\mathbf{w}^{\mathrm{H}}\mathbf{R}_N\mathbf{w}\,. \tag{3.18}$$

Therefore, (3.17) is converted to

$$\hat{\xi}(\mathbf{w})=E[|r(n+1)|^2]-\mathbf{w}^{\mathrm{H}}\mathbf{z}-\mathbf{z}^{\mathrm{H}}\mathbf{w}+\mathbf{w}^{\mathrm{H}}\tilde{\mathbf{R}}\mathbf{w} \tag{3.19}$$

where

$$\begin{aligned}\tilde{\mathbf{R}}&=\mathbf{R}+\frac{2(\gamma+1)}{\gamma^2}(1-\rho^{(L)})\mathbf{R}_N\\ &=\mathbf{R}_S+\chi\mathbf{R}_N\end{aligned} \tag{3.20}$$

and

$$\chi=1+\frac{2(\gamma+1)}{\gamma^2}(1-\rho^{(L)})\,. \tag{3.21}$$

Equation (3.19) is the same as the optimization problem for the multi-port structure. Similar to the optimization for the multi-port algorithm, the optimum solution for (3.19) is given by

$$\hat{\mathbf{w}}=\tilde{\mathbf{R}}^{-1}\mathbf{z} \tag{3.22}$$

which may be written as

$$\hat{\mathbf{w}} = \frac{\sqrt{P_s P_r}}{\chi + \kappa} \mathbf{R}_N^{-1} \mathbf{s}_0 \tag{3.23}$$

where P_r is the reference signal power and $\kappa = P_s \mathbf{s}_0^{\mathrm{H}} \mathbf{R}_N^{-1} \mathbf{s}_0$. Therefore, the optimum solution is the same as the optimum solution for the multi-port structure. In (3.20) perturbation of the weights has changed the noise and interference power by the factor β. By a proper choice for γ, the noise and interference power can be reduced and as a result the error power can be minimized. The minimum error using the weight vector in (3.19) is given by

$$\begin{aligned} \hat{\xi}_{\min} &= E\left\{ \left| r(n+1) \right|^2 \right\} - \mathbf{z}^{\mathrm{H}} \tilde{\mathbf{R}}^{-1} \mathbf{z} \\ &= \frac{P_r \chi}{\kappa + \chi}. \end{aligned} \tag{3.24}$$

Since $P_s \mathbf{s}_0^{\mathrm{H}} \mathbf{R}_N^{-1} \mathbf{s}_0$ is always a positive number, the minimum error in (3.24) is a monotonically increasing function of χ. Therefore, decreasing χ decreases the error. For a multi-port structure χ is unity. For the single-port technique χ can be controlled by the perturbation factor γ and the temporal correlation $\rho^{(L)}$. Minimizing $\chi(\gamma)$, an optimum value of $\gamma = -2$ is obtained which is also interesting from a hardware implementation point of view as discussed in the last sub-section. Furthermore, it is interesting to see that by decreasing the temporal correlation $\rho^{(L)}$ the error is increased. However, reducing $\rho^{(L)}$ from a limit deteriorates the transient performance of the adaptive algorithm.

3.3 Adaptive Single-Port ULMS

As shown in Chapter 2, for the standard ULMS algorithm the weights are updated by

$$\mathbf{w}(n+1) = \mathbf{w}(n) - \mu\hat{\mathbf{g}}(\mathbf{w}(n)) \tag{3.25}$$

where the gradient vector $\hat{\mathbf{g}}(\mathbf{w}(n))$ is given by

$$\hat{\mathbf{g}}(\mathbf{w}(n)) = -2\hat{\mathbf{x}}(n+1)\hat{\varepsilon}^*(\mathbf{w}(n)) \tag{3.26}$$

and

$$\hat{\varepsilon}(\mathbf{w}(n)) = r(n+1) - \mathbf{w}^{\mathrm{H}}\hat{\mathbf{x}}(n+1). \tag{3.27}$$

An important measure of the algorithm's performance is the gradient average which is discussed in the next sub-section.

3.3.1 Gradient Average

The gradient average for the single-port ULMS algorithm is obtained by averaging (3.26) which is given by

$$E[\mathbf{g}(\mathbf{w}(n))] = -2E[\hat{\mathbf{x}}(n+1)r^*(n+1)] + 2E[\hat{\mathbf{x}}(n+1)\hat{\mathbf{x}}^{\mathrm{H}}(n+1)\mathbf{w}(n)] \ . \tag{3.28}$$

The first term is given by

$$E[\hat{\mathbf{x}}(n+1)r^*(n+1)] = E[\mathbf{x}(n+1)r^*(n+1)] = \mathbf{z} \tag{3.29}$$

where the correlation between the $\mathbf{x}_k(n+1)$ and $\mathbf{w}_k(n), k = 1,2,...,L$ as well as $\mathbf{A}(n)$ is ignored. This is acceptable as long as the signals in the consequent iterations are not very correlated. In most ULMS analysis it is assumed that the array signal vector and $\mathbf{w}(n)$ are uncorrelated. In [92]-[101], the ULMS algorithm with correlated data has been studied and it is shown that very high correlation values and large gradient step size

degrade the ULMS performance. In this work, due to the high weighting rate, consequent array signal vectors are correlated. In addition, due to the dependence of $\mathbf{w}(n)$ on the array signal vector in the previous iteration, $\mathbf{x}_k(n)$, $\mathbf{x}_k(n+1)$ and $\mathbf{w}_k(n)$ are somehow correlated. However, while the correlation between consequent samples in different perturbations are high, it is very low between different iterations. To avoid the correlation effect between signals of adjacent iteration cycles, a time margin may be left between the iterations. Therefore, the expectation operation can be applied to $\mathbf{x}_k(n+1)$ and $\mathbf{w}_k(n)$ separately.

The term $\hat{\mathbf{x}}(n+1)\hat{\mathbf{x}}^{\mathrm{H}}(n+1)$ in (3.28) is correlated with $\mathbf{w}(n)$ and can not be simplified easily. However, since $\mathbf{x}(n+1)$ and $\mathbf{w}(n)$ can be assumed uncorrelated, the expectation operation over terms related to $\mathbf{x}(n+1)$ and $\mathbf{w}(n)$ can be applied separately. Therefore the second term in (3.28) is given by

$$\begin{aligned} E[\hat{\mathbf{x}}(n+1)\hat{\mathbf{x}}^{\mathrm{H}}(n+1)\mathbf{w}(n)] &= E[\mathbf{A}\mathbf{y}(n+1)\mathbf{y}^{\mathrm{H}}(n+1)\mathbf{A}^{\mathrm{H}}\mathbf{w}(n)] \\ &= \mathbf{R}\bar{\mathbf{w}}(n) + E[\mathbf{A}(n)\mathbf{R}_e(n)\mathbf{A}^{\mathrm{H}}(n)\mathbf{w}(n)] \\ &= \mathbf{R}\bar{\mathbf{w}}(n) + \mathbf{E}_{\mathrm{P}} \end{aligned} \tag{3.30}$$

where the expectation operation is applied on the signals first and the matrix $\mathbf{R}_e$ is given by (3.16). Using (3.16) and (3.30), the vector $\mathbf{E}_{\mathrm{P}}$ may be written as

$$\mathbf{E}_{\mathrm{P}} = \mathbf{D}\mathbf{R}_{\mathrm{N}}\bar{\mathbf{w}}(n) + \mathbf{e}_{\mathrm{NL}} \tag{3.31}$$

where $\mathbf{D}$ is a diagonal matrix with elements

$$\mathbf{D}(i,i) = d_i = \frac{1}{\gamma}\begin{cases} -\rho^{(1)} + (\gamma+1)\rho^{(L-1)} - \gamma, & i = 1 \\ (\gamma+1)\rho^{(L-i)} - \rho^{(i)} - \gamma, & 1 < i < L \\ -\rho^{(L-1)} + (\gamma+1)\rho^{(1)} - \gamma, & i = L \end{cases} \tag{3.32}$$

and $\mathbf{e}_{\mathrm{NL}}$ is a nonlinear vector function of the weights, whose elements are given by

$$\mathbf{e}_{\mathrm{NL}}(j)=\begin{cases}\dfrac{1-\rho^{(1)}+(\gamma+1)(\rho^{(L-1)}-\rho^{(L)})}{\gamma^2}E\left[\dfrac{\mathbf{w}(n)\mathbf{R}_N\mathbf{w}(n)}{w_1^*}\right], & j=1\\ \dfrac{\rho^{(j-1)}-\rho^{(j)}+(\gamma+1)(\rho^{(L-j)}-\rho^{(L-j+1)})}{\gamma^2}E\left[\dfrac{\mathbf{w}_j(n)\mathbf{R}_N\mathbf{w}(n)}{w_j^*}\right], & j\neq 1,L\\ \dfrac{(\gamma+1)(\rho^{(L-1)}-\rho^{(L)})+(\gamma+1)^2(1-\rho^{(1)})}{\gamma^2}E\left[\dfrac{\mathbf{w}(n)\mathbf{R}_N\mathbf{w}(n)}{w_L^*}\right], & j=L\end{cases} \quad (3.33)$$

As can be seen from (3.33), the elements of $\mathbf{e}_{\mathrm{NL}}$ are proportional to $1/\gamma^2$, $(1+\gamma)/\gamma^2$ or $(1+\gamma)^2/\gamma^2$ factors. A proper value of γ which reduces all the three factors should be used. Using values of γ with small absolute value ($|\gamma|<1$) increases the three factors. Besides, using positive values, though large values, increases the second and third factors. Using negative values of γ with $|\gamma|>>2$ is not a good choice because of the terms with factors $(1+\gamma)/\gamma^2$ or $(1+\gamma)^2/\gamma^2$. The optimum value may slightly change but is close to $\gamma=-2$. Besides, since with $\gamma=-2$ there is no amplitude perturbation and only phase is inverted, it is the most desired value. With $\gamma=-2$, each term in $\mathbf{e}_{\mathrm{NL}}(j)$ is proportional to $(\rho^{(j-1)}-\rho^{(j)}+\rho^{(L-j+1)}-\rho^{(L-j)})/4$, $1\le j\le L$ which is very small for a high weighting rate. For example, for a four-element array and $f_s=5B_T$, these coefficients are [-0.0515,-0.0184, 0.0184, 0.0515]. In general, the maximum terms are the first and the L^{th} elements which are equal. However, since the first element and the L^{th} element of $\mathbf{e}_{\mathrm{NL}}$ are also proportional to $\mathbf{w}(n)\mathbf{R}_N\mathbf{w}(n)$ which is minimized during adaptation, these terms are small. In fact, the adaptive algorithm is minimizing the term $\mathbf{w}(n)\mathbf{R}_N\mathbf{w}(n)$ and after few iteration cycles it becomes very small compared to other

terms. Therefore, the factor $\mathbf{e}_{\mathrm{NL}}$ which is the nonlinear term can be ignored after few iteration cycles. Ignoring $\mathbf{e}_{\mathrm{NL}}$ and using (3.30) and (3.31), Equation (3.28) reduces to

$$E[\mathbf{g}(\mathbf{w}(n))] = -2\mathbf{z} + 2\mathbf{R}\overline{\mathbf{w}}(n) + 2\mathbf{D}\mathbf{R}_N\overline{\mathbf{w}}(n) \tag{3.34}$$

Using $\mathbf{z} = [\mathbf{R}_s + (1 + 2\frac{\gamma+1}{\gamma^2}(1-\rho^{(L)})\mathbf{R}_N]\hat{\mathbf{w}}$ from (3.22) in (3.33) we have

$$\begin{aligned} E[\mathbf{g}(\mathbf{w}(n))] &= -2\mathbf{z} + 2[\mathbf{R}_s + (\mathbf{I}+\mathbf{D})\mathbf{R}_N]\overline{\mathbf{w}}(n) \\ &= 2[\mathbf{D} - 2\frac{\gamma+1}{\gamma^2}(1-\rho^{(L)})\mathbf{I}]\mathbf{R}_N\overline{\mathbf{w}}(n) \end{aligned} \tag{3.35}$$

In (3.35), the gradient bias is very small because the elements of the matrix term $[\mathbf{D} - 2\frac{\gamma+1}{\gamma^2}(1-\rho^{(L)})\mathbf{I}]$ become very small by controlling the perturbation and sampling factors. In addition, the factor $\mathbf{R}_N\overline{\mathbf{w}}(n)$ is decreasing as the adaptive algorithm converges. Moreover, if the elements of the diagonal matrix $[\mathbf{D} - 2\frac{\gamma+1}{\gamma^2}(1-\rho^{(L)})\mathbf{I}]$ are equal, the gradient bias does not affect the steady state weight vector as shown in the next sub-section.

3.3.2 Convergence analysis and convergence speed

In this part the transient performance of the ULMS with the proposed perturbation algorithm is investigated. Averaging (3.25) and using (3.34) gives

$$\overline{\mathbf{w}}(n+1) = \overline{\mathbf{w}}(n) - \mu(-2\mathbf{z} + 2[\mathbf{R}_s + (\mathbf{I}+\mathbf{D})\mathbf{R}_N]\overline{\mathbf{w}}(n) + \mathbf{e}_{\mathrm{NL}}) \tag{3.36}$$

or

$$\overline{\mathbf{w}}(n+1) = (\mathbf{I} - 2\mu\overline{\mathbf{R}})\overline{\mathbf{w}}(n) + 2\mu\mathbf{z} + 2\mu\mathbf{e}_{\mathrm{NL}} \tag{3.37}$$

where

$$\overline{\mathbf{R}} = [\mathbf{R}_s + (\mathbf{I} + \mathbf{D})\mathbf{R}_N]. \tag{3.38}$$

The vector $\mathbf{e}_{\mathrm{NL}}$ has small entries which are decreasing as the weight vector approaches the optimum weight vector. Noting that the coefficient μ is also very small, the third term in (3.37) can be ignored. Therefore, similar to the analysis of the multi-port algorithm [1], when $\mu < 1/(2\lambda_{\max})$ and $\lambda_{\max}$ is the largest eigenvalue of $\overline{\mathbf{R}}$, the algorithm converges to $\overline{\mathbf{w}}(\infty) = \overline{\mathbf{R}}^{-1}\mathbf{z}$. When temporal correlation is high, $\overline{\mathbf{R}}$ is very close to $\mathbf{R}$ and the single-port algorithm converges to the same weight vector as the multi-port algorithm. Moreover, the single-port algorithm converges to the same weight vector when the elements of the diagonal matrix $\mathbf{D}$ are the same ($d_1 = d_2 = \ldots = d_L$). With this assumption, $\overline{\mathbf{R}}$ is given by

$$\overline{\mathbf{R}} = [\mathbf{R}_s + (1 + d_1)\mathbf{R}_N]. \tag{3.39}$$

Therefore, the algorithm converges to

$$\overline{\mathbf{w}}(\infty) = \frac{\sqrt{P_s P_r}}{1 + d_1 + \kappa}\mathbf{R}_N^{-1}\mathbf{s}_0 \tag{3.40}$$

which is different from the multi-port weight vector only by a multiplicative constant. By choosing proper values for γ, the elements of the matrix $\mathbf{D}$ can be controlled to be almost equal. For example, with $L = 4, Q = 3$ and $\gamma = -2$, $d_1 = d_2 = \ldots = d_L = -0.5865$. The effect of the factor $2\mu\mathbf{e}_{\mathrm{NL}}$ in (3.37) can be controlled using small μ values at the beginning and increasing them after few iterations.

The convergence speed of the algorithm is controlled by the eigenvalues of $\overline{\mathbf{R}}$ and μ. When the elements of $\mathbf{D}$ have negative values, the eigenvalues of $\overline{\mathbf{R}}$ are smaller

than the corresponding eigenvalues of $\mathbf{R}$. It can be shown that for $\gamma < (\rho^{(L-1)} - \rho^{(1)})/(1-\rho^{(L-1)})$ all the diagonal elements of $\mathbf{D}$ are negative. Lower eigenvalues lower the convergence speed of the new technique compared to the multi-port algorithm for a fixed gradient step size μ. However, since the largest eigenvalue of $\overline{\mathbf{R}}$ is smaller than that of $\mathbf{R}$, higher values of μ may be used to increase the convergence speed of the new algorithm. The maximum permissible μ is also limited by the nonlinear term (third term) in (3.37). Different simulations show that the maximum permissible μ is lower but close to that of the multi-port algorithm. However, if variable μ is used with small initial values and large final values, the single-port structure converges with larger final μ values.

3.3.3 Gradient covariance and misadjustment

Gradient covariance affects the transient performance of the adaptive algorithm. It can be shown that the gradient covariance for the single-port algorithm is given by

$$\mathrm{cov}(\hat{\mathbf{g}}(\mathbf{w}(n)) \cong 4\hat{\xi}_{\min}\mathbf{R}. \tag{3.41}$$

where $\hat{\xi}_{\min}$ is given by (3.24) which is similar to that of multi-port algorithm ($4\xi_{\min}\mathbf{R}$), but $\xi_{\min}$ is changed to $\hat{\xi}_{\min}$. It can be shown that for $\gamma = -2$ and $Q = L$, $\hat{\xi}_{\min} < \xi_{\min}$. Thus, the proposed structure achieves lower gradient covariance.

As discussed before, the misadjustment is generally used to measure the algorithm's performance. It can be shown that the misadjustment for the single-port algorithm is given by

$$MA = \frac{\mu\chi(\chi+\kappa)}{\chi^2+\kappa} tr\{[\overline{\mathbf{R}} - \mu\overline{\mathbf{R}}^2]^{-1}\mathbf{R}^2\} \tag{3.42}$$

which for small μ values reduces to

$$MA = \frac{\mu\chi(\chi+\kappa)}{\chi^2+\kappa} tr\{\bar{\mathbf{R}}^{-1}\mathbf{R}^2\}. \tag{3.43}$$

When the elements of the diagonal matrix **D** are close $(d_1 \cong d_2 \cong ... \cong d_L), \bar{\mathbf{R}} \cong [\mathbf{R}_s + (1+d_1)\mathbf{R}_N]$ a simpler formula for the misadjustment is obtained. In this case it can be shown that

$$\begin{aligned} \bar{\mathbf{R}}^{-1}\mathbf{R}^2 &= \frac{\kappa+2d_1+1}{(1+d_1)(\kappa+1+d_1)}\mathbf{R}_S + \frac{1}{(1+d_1)}\mathbf{R}_N \\ &= \frac{(\kappa+1+d_1)+d_1}{(1+d_1)(\kappa+d_1+1)}\mathbf{R}_S + \frac{1}{(1+d_1)}\mathbf{R}_N. \end{aligned} \tag{3.44}$$

Using the fact that $\kappa+1+d_1 \gg d_1$, $\bar{\mathbf{R}}^{-1}\mathbf{R}^2 \cong \frac{1}{(1+d_1)}\mathbf{R}$ and using $\kappa \gg d_1+1$, misadjustment in (3.44) is given by

$$MA = \frac{\mu\chi}{(d_1+1)} tr\{\mathbf{R}\}. \tag{3.45}.$$

Different simulations show that for γ around -2 and Q around L, $\chi < (d_1+1)$ which lowers the misadjustment of the proposed technique compared to the multi-port technique. For example, with $\gamma = -2$, $\chi = (1+\rho^{(L)})/2$ and $d_k = (\rho^{(k)} + \rho^{(L-k)} - 2)/2$ which using $Q = L = 4$, results in $\chi = 0.5$, $d_1 = d_3 = -0.4$ and $d_2 = -0.36$, $d_4 = -0.5$. Setting d_1 the average of d_k values, which is equal to -0.415, the misadjustment for the single-port technique is lowered by 1.36dB compared to the multi-port structure.

3.4 Simulation Results and Discussions

3.4.1 Steady state analysis

In this part the steady state performance of the proposed perturbation technique is investigated. A four element array with half wavelength spacing is considered. Three directional Gaussian interference sources with equal average power impinging from $-60^{\circ}, 10^{\circ}$ and 50° and a non-directional Gaussian white noise source are considered in the channel. The desired signal is also a Gaussian signal with unity average power which is impinging from -20° direction. The signal to interference ratio (SIR) for each source and signal to noise ratio (SNR) are considered -10dB and 10dB, respectively.

Figure 3.2 shows the MMSE obtained using (3.24) as a function of perturbation factor (γ) for different perturbation rates. The MMSE obtained using (3.24) with $\beta = 1$ for the multi-port structure is also shown. As can be seen, the single-port structure's MMSE is less than that of the multi-port structure for $\gamma \leq -1$ and the minimum MMSE happens for $\gamma = -2$. In addition, by decreasing the perturbation rate (Q), the MMSE is lowered which agrees with the discussion in Section 3.3. While the single-port MMSE is not an actual MMSE, but since the gradient covariance is proportional to this error, it lowers the gradient covariance. Figure 3.3 shows the multi-port MMSE which is the actual MMSE using the optimum single-port weight vector obtained by (3.23) and multi-port MMSE. As can be seen for $\gamma \leq -1$ the actual MMSE using single-port weight vector is equal to the multi-port MMSE.

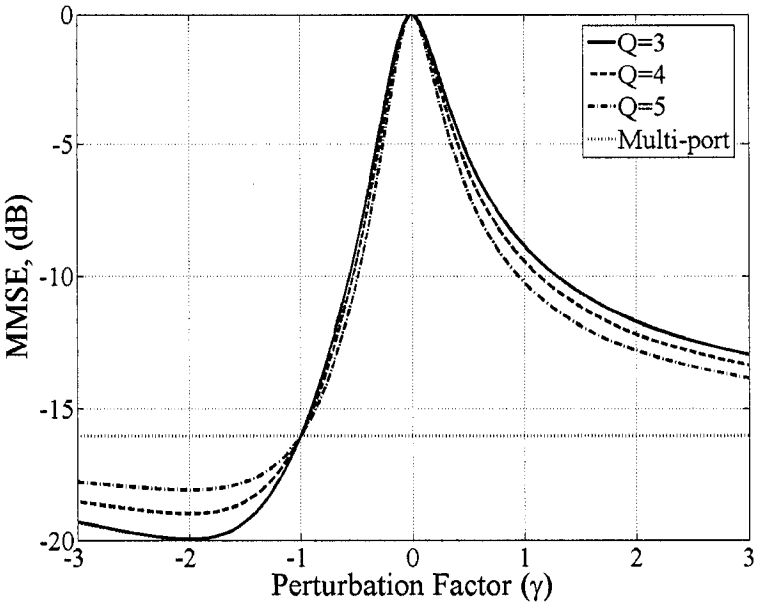

Figure 3.2 A comparison of steady state MMSE for single-port HM-DBF ($\hat{\xi}_{\min}$) and multi-port structures ($\xi_{\min}$).

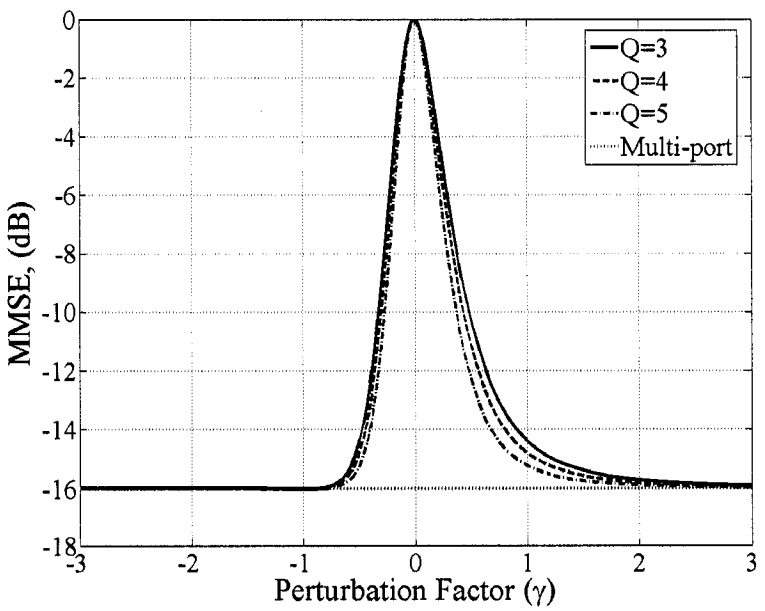

Figure 3.3 Multi-port MMSE with optimum single-port weight vector and optimum multi-port weight vector.

Figure 3.4 compares the steady state error by the optimum weight vector $\hat{\mathbf{w}}$ given by (3.23) and by the converged weight vector given by $\overline{\mathbf{w}}(\infty) = \overline{\mathbf{R}}^{-1}\mathbf{z}$. For this purpose, the ratio of errors ($\xi(\hat{\mathbf{w}}) / \xi(\overline{\mathbf{w}}(\infty))$) is plotted as a function of γ and for different Q values. As can be seen for γ values close to -2 the ratio in dB approaches zero which shows that the converged weight vector is the same as the optimum single-port weight vector. For $\gamma \geq -1$ and especially at $\gamma = 0$ there are spiky points in the curve which shows that using γ in this range is not suitable.

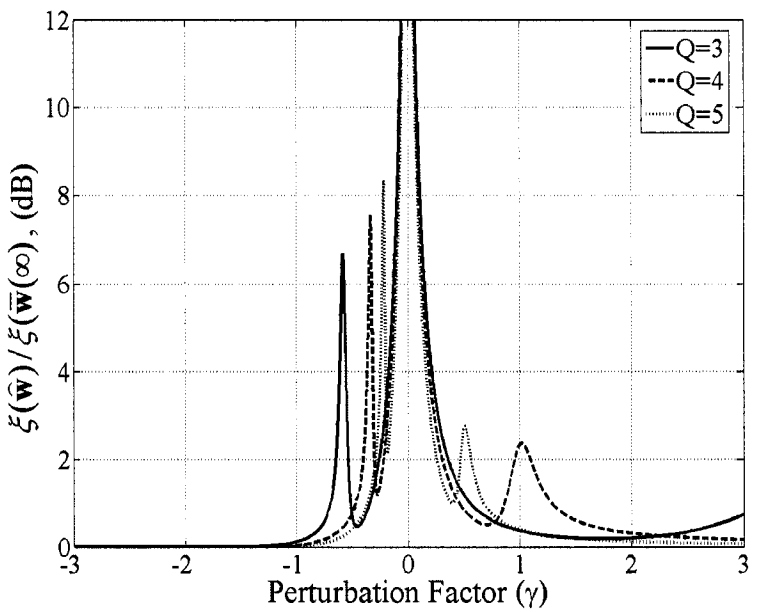

Figure 3.4 Ratio of single-port MMSE with optimum single port weight vector over single-port MMSE with converged single-port weight vector.

3.4.2 Adaptive single-port ULMS algorithm

3.4.2.1 Effect of weighting rate

The same array with the scenario described in the last sub-section is used in the simulations. Adaptive ULMS is simulated with the multi-port and single port structures.

The gradient step size (μ) and γ are 0.001 and -2, respectively. The results are averaged over 1000 realizations. Figure 3.5 (a),(b) compare the performance of the single-port algorithm with different perturbation rates and the multi-port algorithm. It is assumed that the BPF bandwidth is equal to the bandwidth of the signal and interference sources. An ideal BPF is used in the simulations.

Figure 3.5 (a) shows the excess MSE normalized to the actual MSE using optimum single-port weight vector as a function of iteration numbers. The excess MSE normalized to actual MSE is the misadjustment factor when the algorithm converges. As can be seen the single-port structure achieves lower misadjustment compared to the multi-port structure. By increasing the weighting rate, the misadjustment does not necessarily improve. For the shown scenario, the optimum case is $Q=4$. The results agree with (3.42) as shown later using analytical derivations of the misadjustment. Furthermore, the convergence speed of the single-port structure is close to that of multi-port structure and the convergence speed improves by increasing the weighting rate. There are some jumps in the beginning for lower Q values, which is due to the term $2\mu\mathbf{e}_{\mathrm{NL}}$ in (3.37). However, due to the decreasing nature of $\mathbf{e}_{\mathrm{NL}}$ through the iterations, the effect of this term is not major as the algorithm converges. Figure 3.5 (b) shows the average SINR gain as a function of the iteration number. The SINR gain for the single-port structure is higher, but close to that of the multi-port structure.

Figure 3.6 shows the average power pattern which is obtained by

$$P(\theta)=E\left[\mathbf{w}^{\mathrm{H}}(N_0)\mathbf{s}(\theta)\mathbf{s}^{\mathrm{H}}(\theta)\mathbf{w}(N_0)\right] \tag{3.46}$$

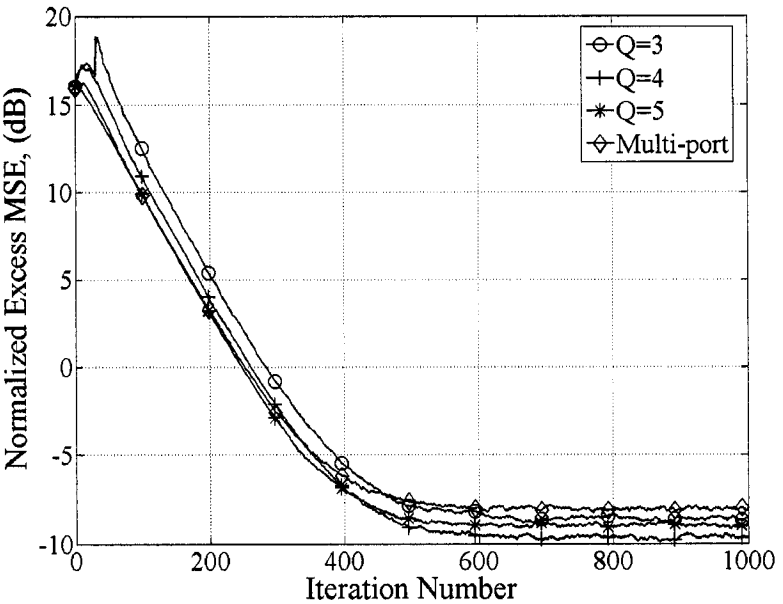

(a)

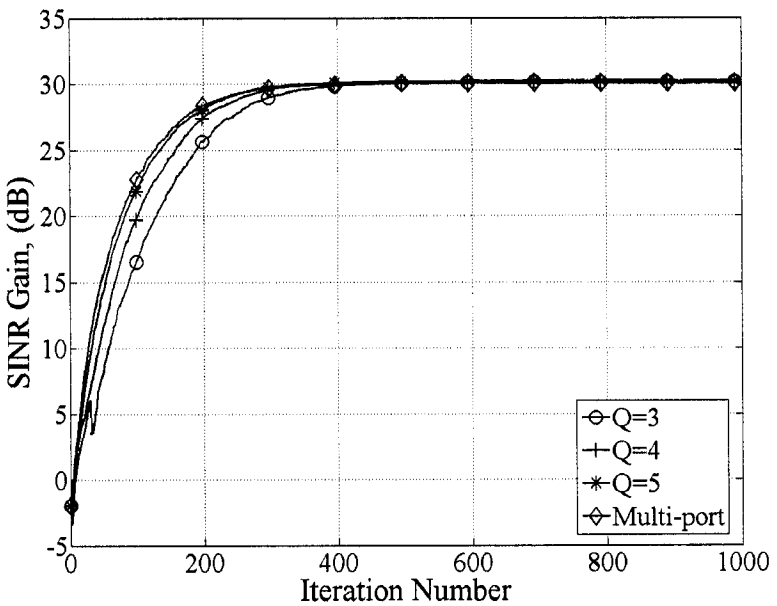

(b)

Figure 3.5 A comparison of single-port and multi-port adaptive algorithm performance. (a) Excess MSE (b) SINR gain.

where $\mathbf{S}(\theta)$ is the steering vector in the θ direction and N_0 is the last iteration number. By averaging in this manner the effect of weight variance is also included. As can be seen, the nulls are deeper with the single-port structure than with the multi-port structure which agrees with the lower misadjustment for the single-port structure in Figure 3.5 (a). The null depths in each case are much deeper if the effect of weight variance is not considered.

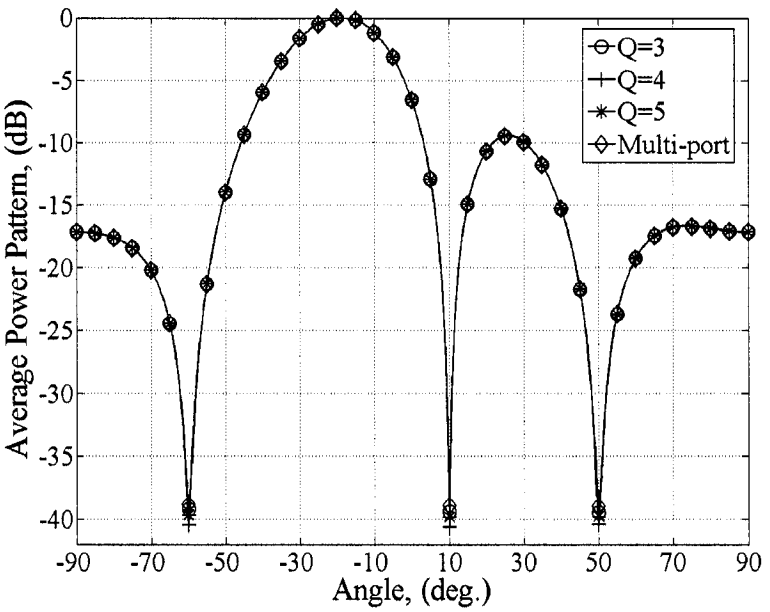

Figure 3.6 A comparison of single-port and multi-port adaptive algorithm performance using average power pattern.

3.4.2.2 Different SIR and SNR values

In this part the adaptive algorithm performance is investigated with different SIR and SNR values to show how the algorithm works in different scenarios. Figure 3.7 shows the normalized excess MSE with SIR=-20dB and different SNR values for single-

port and multi-port structures. $\mu = 0.0002$ and $Q = 4$ are used. As can be seen in all cases the single-port misadjustment is lower than multi-port misadjustment. The convergence speed in each case is very close to that of multi-port algorithm. Again, there are jumps in the initial iterations of the single-port algorithm which is due to the term $2\mu e_{NL}$ in (3.37) and can be avoided by using smaller μ values at the beginning of iterations. Figure 3.8 shows the same curves as in Figure 3.7, but with *SIR=0dB* and $\mu = 0.01$. The same trend as in Figure 3.7 can be observed. Based on Figure 3.7 and Figure 3.8, the adaptive algorithm with the single-port structure is slower in convergence, but achieves higher steady state SINR gain and lower misadjustment for all channel scenarios.

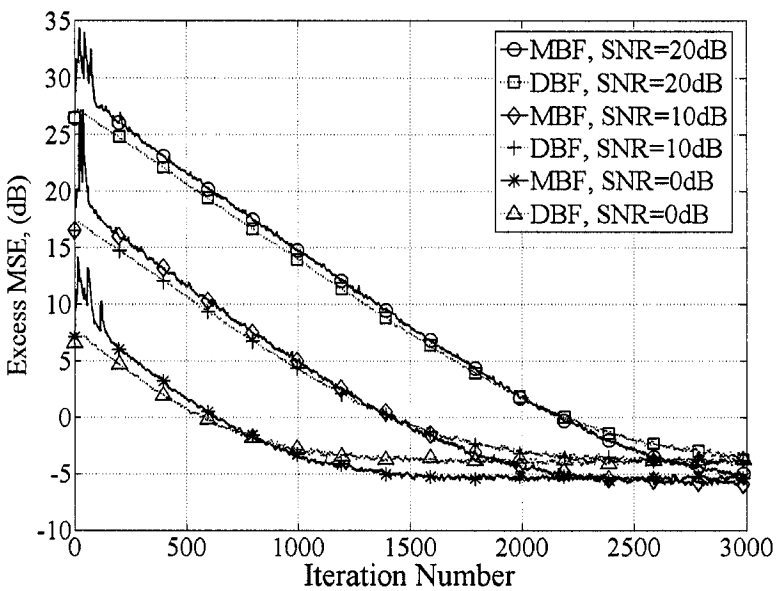

Figure 3.7 A performance comparison of single-port and multi-port algorithms with SIR=20dB different SNR values using normalized excess MSE with $\mu = 0.0002$ and $Q = 4$.

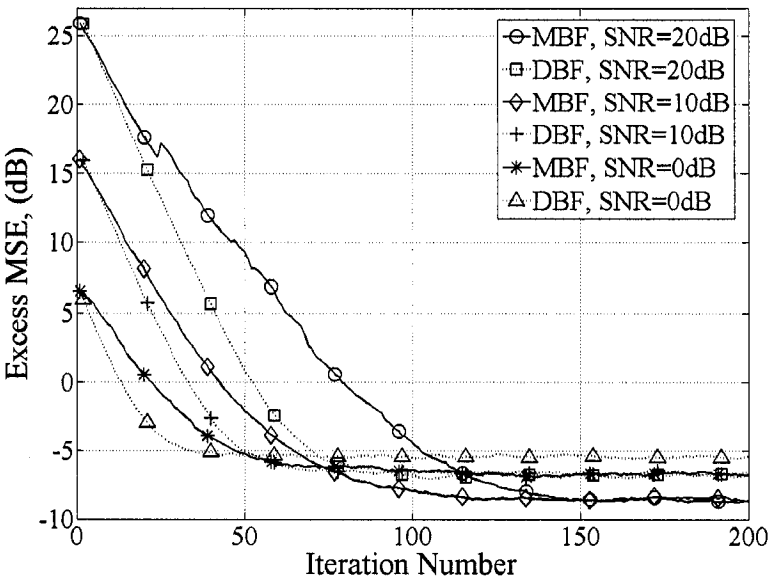

Figure 3.8 A performance comparison of single-port and multi-port algorithms with SIR=0dB different SNR values using normalized excess MSE and $\mu = 0.01$ selected.

3.4.2.3 Effect of perturbation quantization error

In the single-port structure, weight perturbation is carried out using phase shifters and gain control elements. In practice, the phase shifter and gain control elements have limited resolutions. It is well-known that finite phase and amplitude resolutions increase the side-lobe level (SLL) and lowers the null depths. In this part the finite resolution effects on the adaptive algorithm's performance are investigated. The new structure is simulated with finite resolution perturbations. However, in the weight update equation, the calculated weights instead of quantized weights are used. Figure 3.9 shows the SINR gain achieved using calculated weights as a function of iteration number for different perturbation quantization bits. For this simulation $\mu = 0.001$ and $Q = 4$ are considered with the same channel scenario as that for Figure 3.2. As can be seen, decreasing the res-

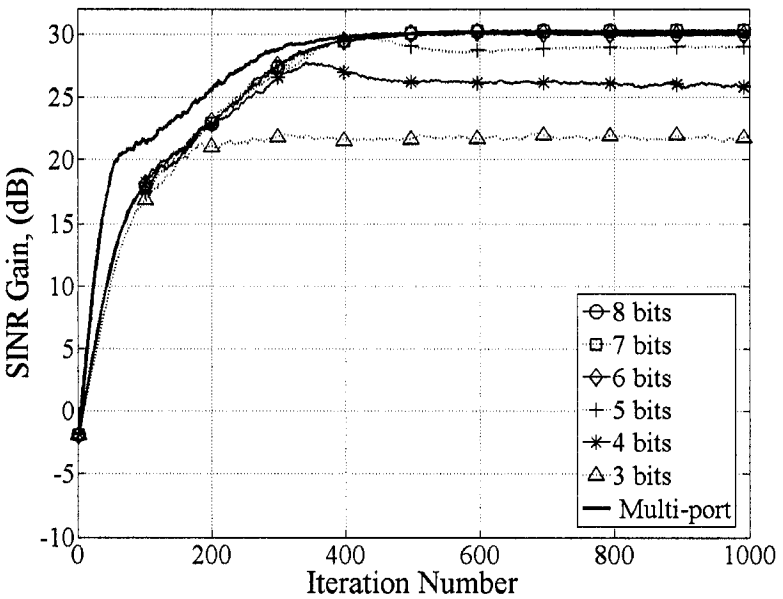

Figure 3.9 SINR gain with different phase and amplitude quantization levels.

-olution results in slight performance deterioration for resolutions of more than five bits. Using a three bits resolution achieves more than 20 dB SINR gain for the given scenario. It should be noted that SINR gain is plotted using calculated weight vectors which are not quantized. In this work the effect of quantized weight on adaptive algorithm performance is of concern. Quantizing the final calculated weights reduces the SINR gain which is independent of the adaptive algorithm.

Figure 3.10 shows the SINR gain with different amplitude quantization bits (n_a). As can be seen the adaptive algorithm performance is not sensitive to the perturbation amplitude quantization as long as the number of bits is more than three. For the scenario used for Figure 3.10, using less than three bits resolution the algorithm does not converge.

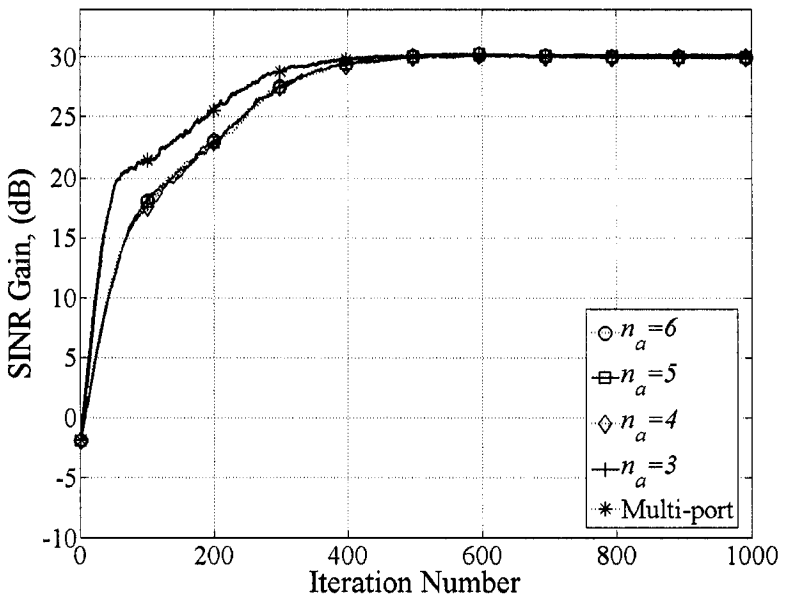

Figure 3.10 SINR gain with six bits phase shifters and different amplitude quantization.

3.4.3 Misadjustment analysis using analytic formulas

In this part the misadjustment for a single-port structure is compared with that of a multi-port structure based on an analytic formulation. Figure 3.11 shows the ratio of the single-port misadjustment to the multi-port misadjustment obtained using analytic formulas as a function of γ for different values of Q. For a single-port structure, the misadjustment is obtained using (3.45) and for multi-port structure using (2.37). The same channel scenario used for Figure 3.6, is used for this simulation. As can be seen for $\gamma \cong -2$ the single-port structure misadjustment is lower than that of the multi-port structure. For $Q = 4$ the misadjustment ratio is the best and as Q increases, the single-port misadjustment approaches that of the multi-port structure over a wider range of γ. This trend agrees with the adaptive simulation results in Figure 3.6 (a). The misadjustment im-

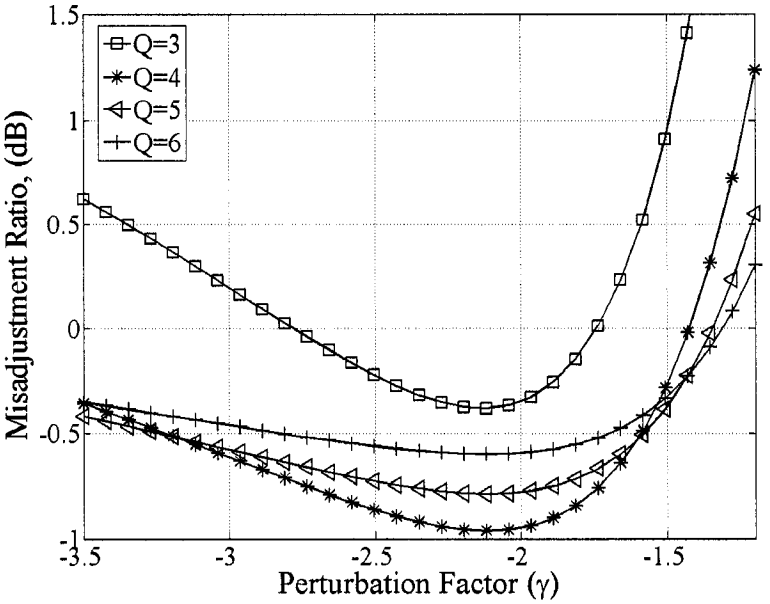

Figure 3.11 Misadjustment ratio using analytical formula for different perturbation factors and perturbation rates.

-provement observed using adaptive simulation as shown in Figure 3.6 (a) for Q=3, 4 and 5 are 0.5dB, 0.9dB and 1.6dB respectively. The corresponding values using Figure 3.11 are 0.35dB, 0.78dB and 0.95dB, respectively. Therefore, the analytic formula in (3.42) overestimates the misadjustment, but it gives a correct trend. Different channel scenarios are investigated and it is observed that the misadjustment estimated by (3.42) gives slightly higher values than those obtained by the adaptive algorithm. Therefore, the misadjustment in (3.42) can be considered as an upper bound for the single-port structure's misadjustment.

Figure 3.12 shows the misadjustment ratio as a function of Q for different SIR and SNR values. For this simulation $\gamma = -2$ and $\mu = 0.0005$. As can be seen the optimum

Q happens somewhere between Q=3 and Q=4, depending on the channel SIR and SNR. Furthermore, as Q increases the single-port misadjustment approaches the multi-port misadjustment. However, this misadjustment improvement depends on the SNR and SIR values. By increasing the SNR the improvement increases, but by increasing the SIR the trend is more complicated.

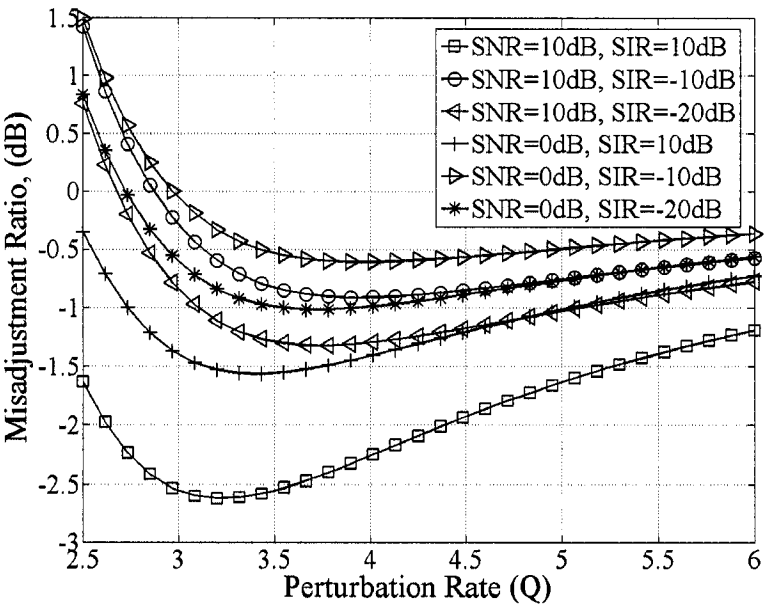

Figure 3.12 Misadjustment ratio using analytical formula versus perturbation rate for SIR and SNR values.

Figure 3.13 shows the misadjustment ratio for Q=4, $\mu = 0.0001$ and $\gamma = -2$ as a function of SIR for different SNR values. As can be seen for very low and very high SIR values misadjustment improvement is high, but it is low for moderate SIR values. The same trend is observed for each SNR value.

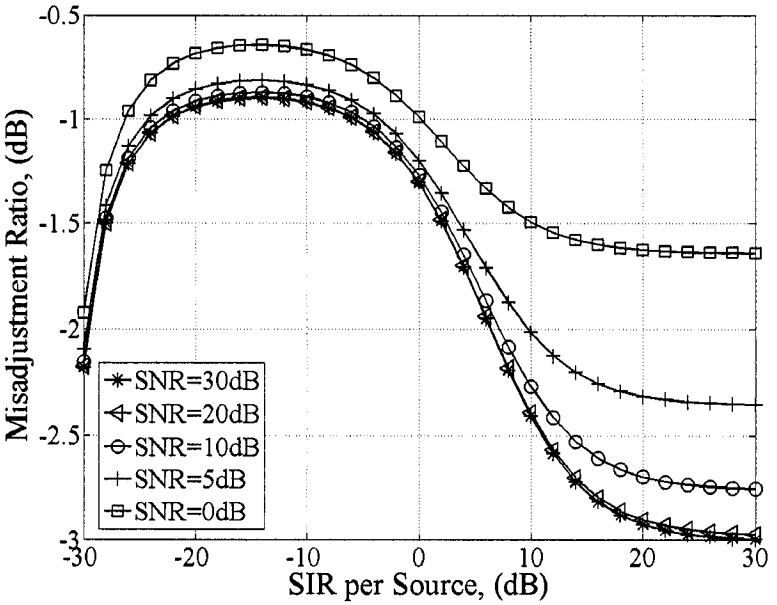

Figure 3.13 Misadjustment ratio versus SIR for different SNR values.

Figure 3.14 shows the misadjustment ratio for the channel used to generate Figure 3.6 results as a function of μ for different values of Q. As can be seen, as μ increases, the misadjustment improvement increases. In addition, for smaller values of Q the improvement with μ is faster.

Figure 3.15 shows the misadjustment ratio when single-port misadjustment is obtained using small μ formula in (3.43) and the derived approximation in (3.45) for different Q and SIR values. In this figure, the curves labelled "accurate" refer to the result by (3.43) and approximate ones refer to the result correspond (3.45). $\mu = 0.0001$ is used for the small μ approximation to be valid. The same channel scenario as in Figure 3.6 is considered. As can be seen, for SIR=-10dB and -20dB, corresponding curves are in good agreement. For SIR= 0dB the maximum difference between curves is 0.5 dB which happ-

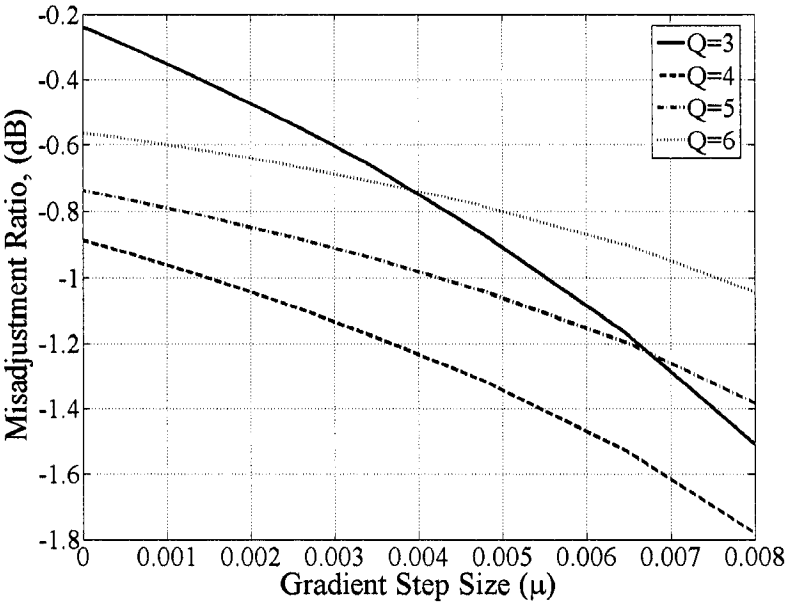

Figure 3.14 Misadjustment ratio versus μ for different Q values.

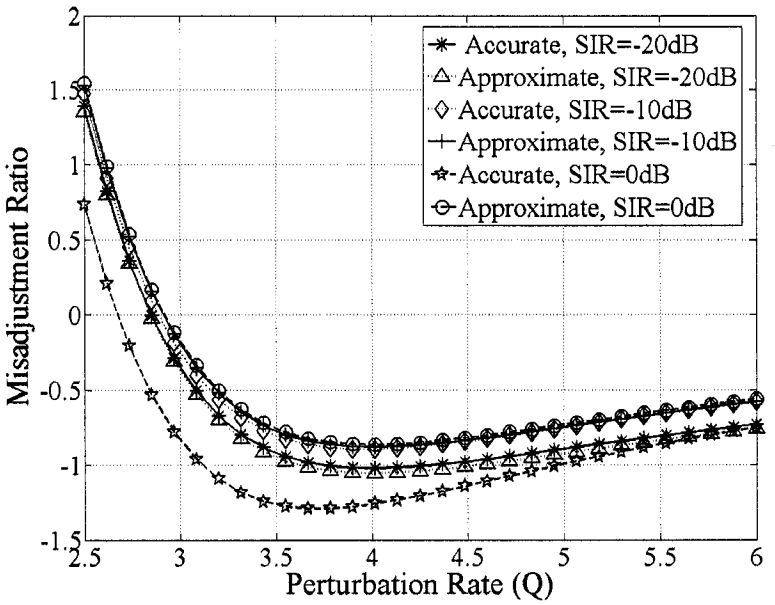

Figure 3.15 Study of misadjustment using simplified closed form formula.

-ens for a misadjustment value of -30 dB (not shown in the figure) which is a small error. Therefore, the approximate formula in (3.45) is a good misadjustment approximation especially for low SIR values.

3.5 Direction of Arrival Estimation

The perturbation technique of this chapter is used for a single-port DOA estimation. Consider an antenna array with L elements used to estimate N_i directional sources. If the antenna array is weighted with the weight vector $\mathbf{w}^{\mathrm{H}}$, the average output power is $P = \mathbf{w}^{\mathrm{H}}\hat{\mathbf{R}}\mathbf{w}$, where $\hat{\mathbf{R}} = E\{\hat{\mathbf{x}}\hat{\mathbf{x}}^{H}\}$ is the covariance matrix of the array and $\hat{\mathbf{x}}$ is the estimated array signal vector. The weight vector $\hat{\mathbf{w}}$ that minimizes P, nulls the directional sources. Therefore, the source directions can be obtained by finding the maxima of the spatial spectrum $1/\left|\mathbf{w}^{H}\mathbf{s}(\theta)\right|^{2}$ where $\mathbf{s}(\theta)$ is the steering vector in the direction θ. To avoid the trivial solution $\mathbf{w} = \mathbf{0}$, $P = \mathbf{w}^{\mathrm{H}}\hat{\mathbf{R}}\mathbf{w}$ is minimized under the constraint $\|\mathbf{w}\|^{2} = 1$, where $\|\cdot\|$ represents the second norm operator. Thus, using the Lagrange multiplier λ, the optimization problem is given by

$$P = \mathbf{w}^{\mathrm{H}}\hat{\mathbf{R}}\mathbf{w} + \lambda(1 - \|\mathbf{w}\|^{2}). \tag{3.47}$$

Based on (3.47) the optimum solution $\hat{\mathbf{w}}$ should satisfy $\hat{\mathbf{R}}\hat{\mathbf{w}} = \lambda_{\min}\hat{\mathbf{w}}$ where $\lambda_{\min} = \hat{\mathbf{w}}^{\mathrm{H}}\hat{\mathbf{R}}\hat{\mathbf{w}}$. Therefore, the minimum output power is equal to the smallest eigenvalue ($\lambda_{\min}$) of $\hat{\mathbf{R}}$ which is the noise eigenvalue. The optimum weight vector is the corresponding eigenvector. The optimum weight vector can be calculated adaptively using the update equation

$$\begin{aligned}\mathbf{v}(n+1) &= \mathbf{w}(n) - \mu(n)g(\mathbf{w}(n)) \\ &= \mathbf{w}(n) - 2\mu(n)\hat{\mathbf{x}}(n+1)\hat{\mathbf{x}}^H(n+1)\mathbf{w}(n) + 2\mu(n)\lambda(n)\mathbf{w}(n)\end{aligned} \tag{3.48}$$

$$\mathbf{w}(n+1) = \mathbf{v}(n+1) / \left\|\mathbf{v}(n+1)\right\| \tag{3.49}$$

where $\mu(n)$ is the gradient step size and $\lambda(n) = \mathbf{w}^H(n)\hat{\mathbf{x}}(n+1)\hat{\mathbf{x}}^H(n+1)\mathbf{w}(n)$. The factor $\lambda(n)$ is a large number in the beginning of iterations and approaches the minimum eigenvalue as adaptive algorithm converges. By choosing a variable gradient step size $\mu(n) = \mu_0 / 2(1 - \mu_0\lambda(n))$, the gradient step size is large in the beginning of iterations and decreases as adaptive algorithm converges. In this way, the convergence speed of the algorithm is increased and the misadjustment noise is lowered. However, $\mu(0)$ should not be too large to assure the algorithm's convergence. In addition, by choosing $\mu(n) = \mu_0 / 2(1 - \mu_0\lambda(n))$, the computational complexity of the algorithm can be lowered. Using $\mu(n) = \mu_0 / 2(1 - \mu_0\lambda(n))$, (3.48) is given by

$$\mathbf{v}(n+1)\mu(n) / \mu(0) = (\mathbf{w}(n) - 2\mu_0\hat{\mathbf{x}}(n+1)\hat{\mathbf{x}}^H(n+1)\mathbf{w}(n)). \tag{3.50}$$

Since the left side of (3.50) is normalized in each iteration cycle, the term $\mu(n) / \mu(0)$ can be dropped in (3.50) and the adaptive equation is simplified to

$$\mathbf{v}(n+1) = (\mathbf{w}(n) - 2\mu_0\hat{\mathbf{x}}(n+1)\hat{\mathbf{x}}^H(n+1)\mathbf{w}(n)). \tag{3.51}$$

Therefore, the weight vector that is obtained from the adaptive algorithm is used to find the direction of the directional signal sources.

3.6 Simulation Results

For comparison purposes, three receiver structures are used for DOA estimation:

1. The proposed adaptive DOA estimation is considered for the single-port structure. The array signals are estimated using the variable perturbation technique through making the antenna array signals temporally correlated. The spatial spectrum is obtained using

$$P_{SP-ANF}(\theta) = 1/\left|\hat{\mathbf{w}}^{H}\mathbf{s}(\theta)\right|^{2} \tag{3.52}$$

where $\hat{\mathbf{w}}$ is the weight vector calculated using the adaptive algorithm.

2. For the second receiver, the array signals are available in the processor. A multi-port structure is considered and element-space spectral MUSIC is employed. The MUSIC spatial spectrum is calculated by

$$P_{\mathrm{MU}}(\theta) = 1/\mathbf{s}^{\mathrm{H}}(\theta)\mathbf{E}_{n}\mathbf{E}_{n}^{\mathrm{H}}\mathbf{s}(\theta) \tag{3.53}$$

where $\mathbf{E}_{n}$ is the noise subspace consisting of noise eigenvectors.

3. For the third case, a single-port structure similar to case 1 is considered but the weight vector is calculated using beam-space MUSIC [102]-[104]. In addition, it is assumed that the array signals are temporally correlated similar to the case 1. $M \leq L$ orthogonal beams are generated sequentially and the beam space covariance matrix of the array is estimated. The noise subspace is calculated from the beam space covariance matrix and the beam-space MUSIC spectrum is calculated using beam-space noise eigenvectors using

$$P_{\mathrm{SPBS\text{-}MU}}(\theta) = \mathbf{B}\mathbf{s}^{\mathrm{H}}(\theta)\mathbf{s}(\theta)\mathbf{B}^{\mathrm{H}} / \mathbf{B}\mathbf{s}^{\mathrm{H}}(\theta)\mathbf{E}_{bn}\mathbf{E}_{bn}^{\mathrm{H}}\mathbf{s}(\theta)\mathbf{B}^{\mathrm{H}} \tag{3.54}$$

where $\mathbf{B}$ is the beam-space transformation matrix consisting the weight vectors of different beams and $\mathbf{E}_{bn}$ is the beam-space noise subspace. A six-element array is used in

the simulations. Five independent sources are impinging on the array from $-50^{\circ}, -30^{\circ}, -10^{\circ}, 10^{\circ}$ and 30° directions. The SNR for each source is considered to be 10dB, $f_w = 6B_T$, and $\mu_0 = 0.01$ are used for SP-ANF. The array covariance matrix for MUSIC and SPBS-MUSIC are calculated in 1000 snapshots and the adaptive weight vector for SP-ANF is also calculated in 1000 iterations. The spectral spectrums in (3.52)-(3.54) are averaged over 100 realizations to have more accurate evaluation of each technique. For the SPBS-MUSIC six orthogonal beams are generated in the directions $\theta_k = \cos^{-1}((2k - L - 2)/L), \quad k = 1, 2, ..., 6$.

Figure 3.16 compares the spatial spectrum for the three techniques. As can be seen both MUSIC and SP-ANF can estimate the directions of sources, but SPBS-MUSIC fails to find the source directions accurately. This shows that temporal correlation alone is not sufficient, but proper beams or perturbation should be used. It should be noted that the array signals have the same temporal correlation for SPBS-MUSIC and SP-ANF. In addition, three of the peaks in the spatial spectrum of SP-ANF are higher than that of MUSIC. This shows that SP-ANF is even superior to MUSIC in this case. Figure 3.17 shows the spatial spectrum of three methods when there are two close sources in the directions -20° and -15°. As can be seen again, both MUSIC and SP-ANF estimate the source directions but SPBS-MUSIC can not discriminate between two sources.

Figure 3.18 illustrates the spatial spectrum of the SP-ANF and MUSIC for SNR=0dB and 5dB, where peak points of the spectrum is shown for clear observation. As can be seen, both SP-ANF and MUSIC estimate the signals DOAs accurately. In addition, the

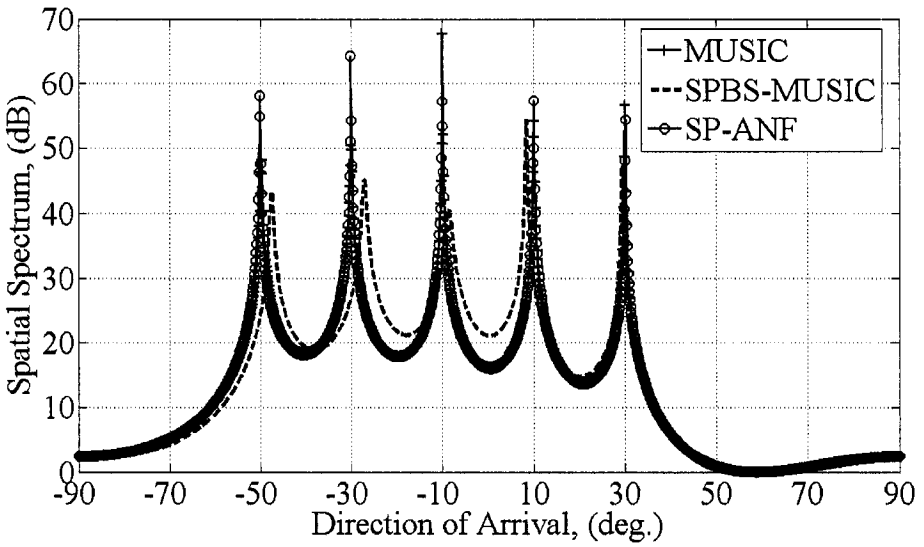

Figure 3.16 A comparison of the spatial spectrums of MUSIC, SPBS-MUSIC and SP-ANF in a channel with five independent sources in the $-50°, -30°, -10°, 10°$ and $30°$ directions.

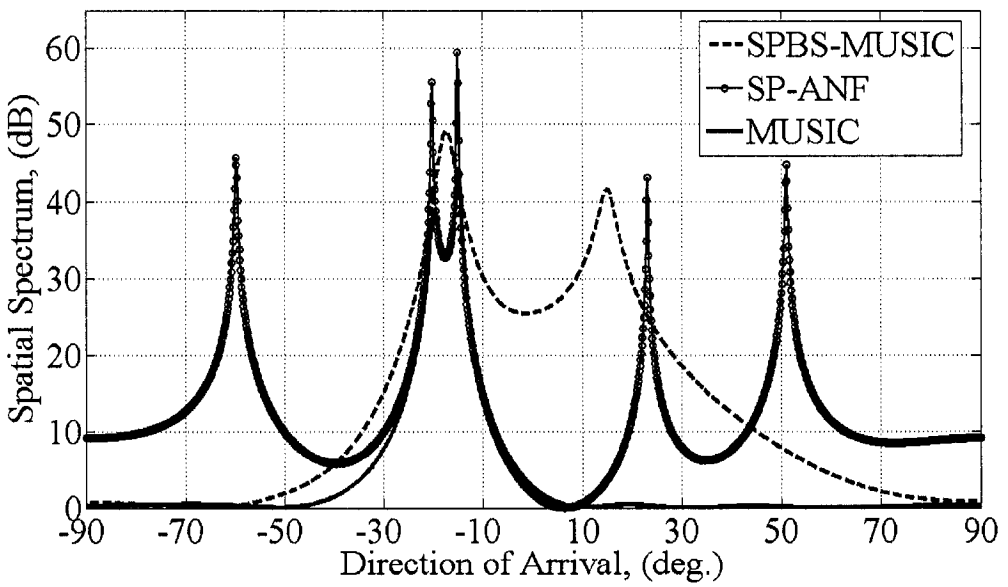

Figure 3.17 A comparison of spatial spectrum for MUSIC, SPBS-MUSIC and SP-ANF in a channel with two independent sources in $-20°$ and $-15°$ directions.

maxima in the spectrum of SP-ANF is higher for SNR=5dB and lower for SNR=0dB than that of the MUSIC spectrum. Studying different SNR values it is observed that the proposed technique is superior to MUSIC for higher SNR values and inferior for lower SNR values.

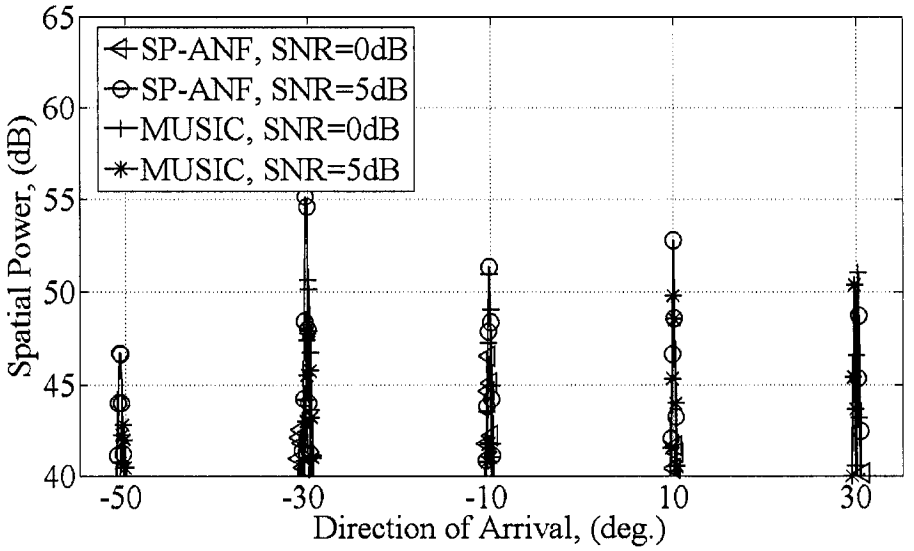

Figure 3.18 Spatial spectrum of SP-ANF with $f_w = 6B_T$ and MUSIC for different SNR values.

Figure 3.19 studies the spatial spectrum of SP-ANF for the scenario in Figure 3.16, but with different weighting rates. As can be seen by increasing the weighting rate from $f_w = 3.5B_T$ to $f_w = 4B_T$, the performance of the technique is significantly improved, but a further increase does not affect the performance considerably. Therefore for this scenario $f_w = 4B_T$ is sufficient to estimate the source directions.

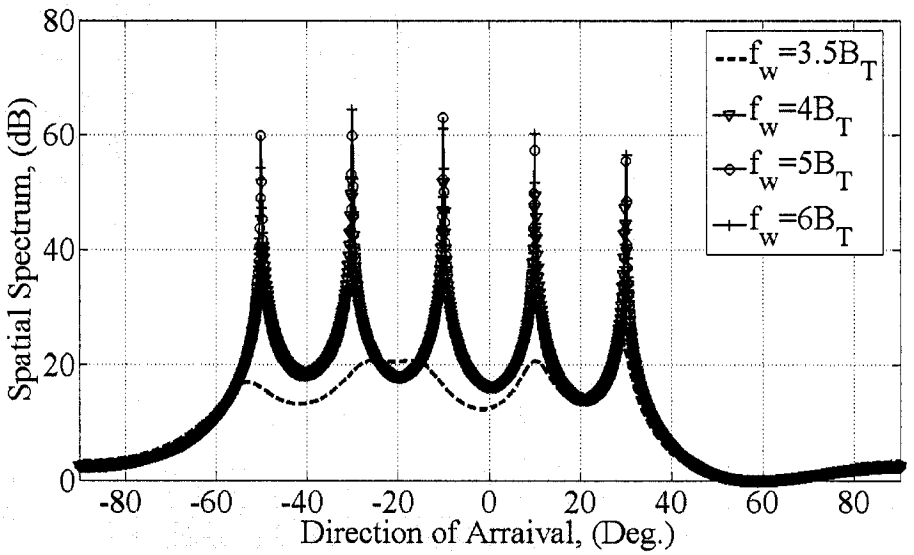

Figure 3.19 Spatial spectrum of the SP-ANF with SNR=10dB and different weighting rates.

3.7 Conclusion

A new perturbation technique for single-port adaptive beamforming and DOA estimation is proposed. The proposed technique is simulated in the steady state and with the adaptive ULMS algorithm. The new technique provides a higher SINR gain than the multi-port structure. The convergence speed of the single-port MBF algorithm is also very close to that of multi-port algorithms. The effect of quantized perturbations on the performance of the algorithm is investigated. It is observed that a weighting resolution more than five bits does not affect the adaptive algorithm performance. In addition, the amplitude gain quantization error does not affect the algorithm performance. Different parameters of the adaptive algorithm such as gradient average, gradient variance, weight covariance matrix and misadjustment factor are analytically investigated and approximate formulas are derived for the algorithm misadjustment. The misadjustment of the

algorithm is compared with that of a multi-port algorithm under different scenarios. It is observed that the proposed technique achieves lower misadjustment than the multi-port structure for $\gamma = -2$ and $Q \cong L$. The proposed perturbation technique is suitable for structures with few antenna elements and for narrowband applications.

A single-port adaptive DOA estimation based on temporally-correlated array signal samples is also proposed. The proposed technique can estimates the DOAs of multiple independent sources in very low SNR levels. The adaptive algorithm weight vector converges to the eigenvector corresponding to the minimum eigenvalue of the array covariance matrix. The proposed technique is compared with the MUSIC and single-port beam space MUSIC technique. The proposed technique outperforms the MUSIC for higher SNR values.

Chapter 4

Microwave Sampling Beamformer

4.1 Introduction

In this chapter a new microwave beamforming technique, the microwave sampling beamformer (MSBF) [105]-[110], is presented. In this technique, both phase and amplitude weightings are accomplished in one block independently. The technique is based on fast switching of the antenna element signals in the microwave domain. Signals received over different antenna elements are switched with a higher rate than the Nyquist rate with control signals whose pulse width and time delays are adjusted. In each element, adjusted time delay and pulse width control the phase shift and amplitude attenuation, respectively. Because the switching rate follows the Nyquist sampling rate, the term sampling is repeatedly used in this thesis instead of switching and the technique is named microwave sampling beamformer (MSBF). The combination of the first replicas of the sampled signals is reconstructed after down conversion. The sampling circuit is designed to increase the power efficiency and to maintain impedance matching.

The chapter is organized as follows. In Section 4.2 the system fundamentals are introduced [106]. Then, the structure of a feed network and always-matched switch are discussed in Section 4.3 [106], [107]. In Section 4.4, validation using microstrip antennas are presented [106]. A validation of the structure using wire antennas is presented in Section 4.5 [105]. A SNR analysis of the structure is presented in Section 4.6 [106]. The effect of the finite pulse train duration is presented in Section 4.7 [109]. The image replica issue and its rejection technique are presented in Section 4.8 [110]. In Section 4.9

some simulation results about the finite duration pulse train and image replica rejection are presented. Finally, a conclusion of the chapter is presented in Section 4.10.

4.2 MSBF Fundamentals

4.2.1 Fundamental idea

The fundamental idea behind the proposed structure is based on the properties of signal sampling. Based on Nyquist's sampling theorem, if a signal with bandwidth B is sampled with a sampling rate $f_s > 2B$, it can be reconstructed again. Sampling of the signals in the microwave frequency range has been accomplished in [53]-[58] for space time multiplexing. In this work, phase and amplitude weighting are synthesized using sampling of antenna elements' signals with sampling pulses which have controlled pulse widths and delays. Different replicas of the original signal, each phase shifted and attenuated by the phase and the amplitude of the corresponding harmonics of the sampling pulse train are produced at the output of the sampling circuit. Therefore, by proper choice of the sampling pulse time delay and duty cycle and filtering the proper replica of the signal at the output, it is possible to apply a proper phase shift and attenuation to the signal. The choice of zeroth replica which is generally the case in communication systems is not applicable for this structure because it does not experience any phase shift. Among other replicas, the first replica of the sampled signal is recovered due to its highest power and its proper amplitude and phase dependence on pulse width and time delay. In the next sections, this idea is applied to the receiver and transmitter of a phased array.

4.2.2 Receiver structure

The proposed receiver structure is shown in Figure 4.1(a). This structure is composed of L antenna elements, electronic switches along with their driving circuits, one combiner, one low noise amplifier (LNA), one mixer, one LPF, one ADC and the processor. The required weights are computed by the processor in the digital domain and the proper signals to control the weights are delivered to the switch driver circuits. As is shown later, the weighting control can be realized using proper sampling of the signals over different antenna elements. Suppose the desired signal vector received over antenna elements is given by

$$\mathbf{x} = [x_1(t), x_2(t), ..., x_L(t)]^T \tag{4.1}$$

where, $x_1(t)$, $x_2(t)$, $....x_L(t)$ are the bandpass amplitude modulated signals received by antenna elements 1,2,...L , respectively. Ignoring the interference, noise, and fading, the signal received by the l^{th} antenna element can be written as,

$$x_l(t) = \mathrm{Re}\{m(t)e^{j2\pi f_c t}e^{j(l-1)\varphi}\} \tag{4.2}$$

where, $m(t)$, f_c and φ are the message signal, the carrier frequency and the differential carrier phase change between two consecutive antenna elements, respectively. The phase angle φ can be written in the from,

$$\varphi = k_0 d\cos\theta \tag{4.3}$$

where, k_0, d , θ are the free space wave number, element spacing and angle of arrival measured from the array axis. In (4.2) it is assumed that the received signal is narrowband enough to assume that message signals received by different antenna

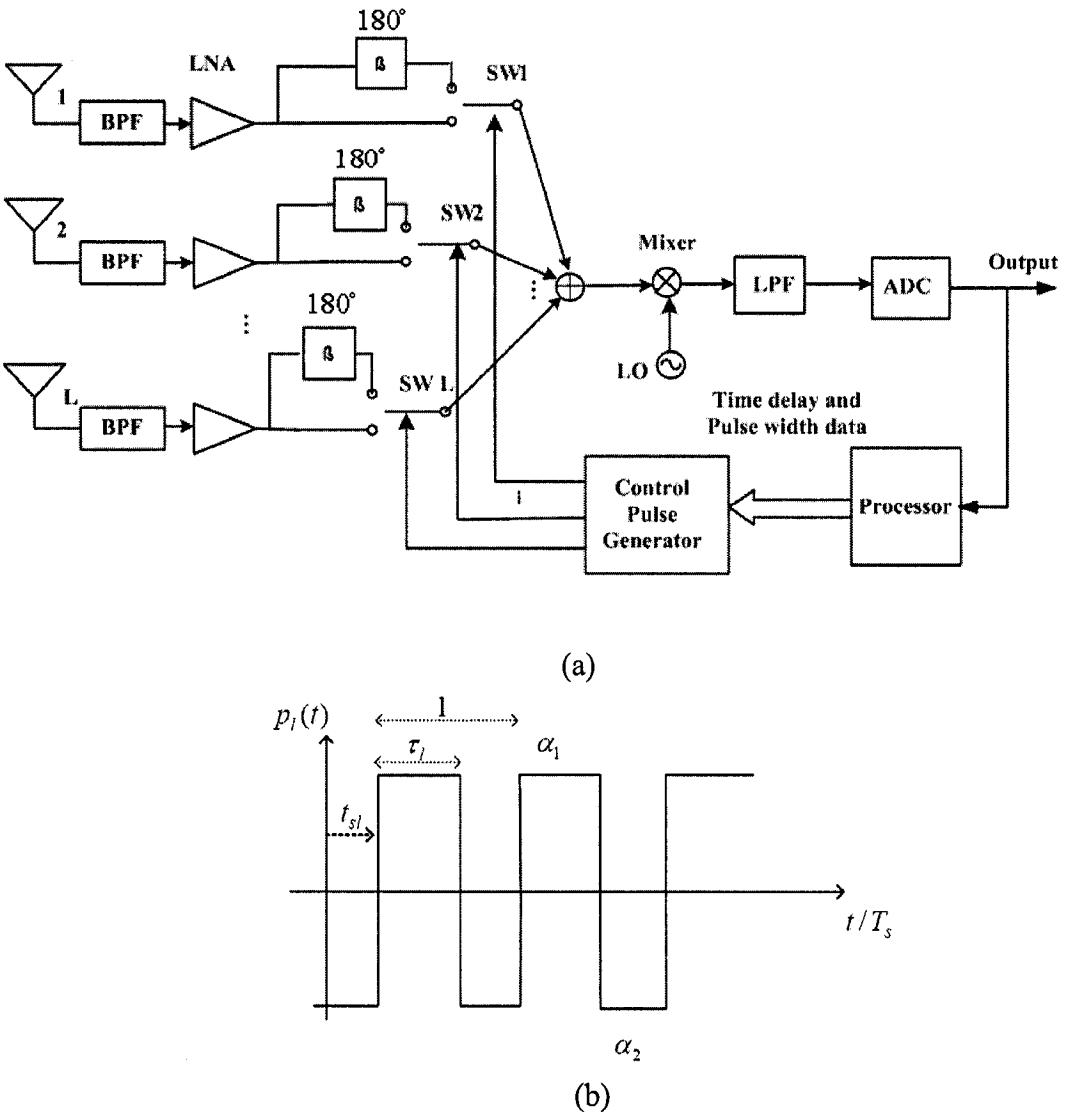

Figure 4.1 (a) An MSBF receiver structure. (b) Equivalent sampling pulse train.

elements does not change and only the high frequency carrier experiences a time delay or phase shift. The general form of the equivalent sampling pulse train on the l^{th} antenna element in one period can be written as

$$p_l(t) = \begin{cases} \alpha_1, & t_{sl} \le t/T_s \le t_{sl} + \tau_l \\ \alpha_2, & Otherwise \end{cases} \tag{4.4}$$

where, T_s is the pulse train period, t_{sl} is the starting time or time delay of the pulse and τ_l is the duty factor of the pulse as shown in Figure 4.1(b). All time parameters are normalized to T_s . α_1 and α_2 model the transmission coefficient of the switch in each time interval. It should be noted that this signal is not exactly the signal that drives the switches, but is the multiplicative equivalence of the switch and the driving circuit. The signal $p_l(t)$ is of finite duration in practice, but in this part is assumed to have infinite duration. The effect of finite duration is investigated in Section 4.6. Therefore, a Fourier series representation for $p_l(t)$ can be written in the form,

$$p_l(t) = \sum_{n=-\infty}^{\infty} c_{nl} e^{j2n\pi f_s t} \tag{4.5}$$

where, c_{nl} is given by,

$$c_{nl} = \begin{cases} \dfrac{\alpha_1 - \alpha_2}{2n\pi} e^{-jn\pi(2t_{sl}+\tau_l)} \sin(n\pi\tau_l), & n \neq 0 \\ (\alpha_1 - \alpha_2)\tau_l + \alpha_2, & n = 0 \end{cases} \tag{4.6}$$

Considering the sampled signals over all antenna elements, the output of the combiner is given by

$$y(t) = \sum_{l=1}^{L} p_l(t) x_l(t) \tag{4.7}$$

which, can be written using (4.2) and (4.6) as

$$y(t) = \sum_{l=1}^{L} \left\{ \mathrm{Re}\left\{ m(t) e^{j2\pi f_c t + (l-1)\varphi} \right\} \sum_{n=-\infty}^{\infty} c_{nl} e^{j2n\pi f_s t} \right\} . \tag{4.8}$$

Suppose the local oscillator output is set to

$$x_{LO}(t) = A_{LO} \cos(2\pi(f_c - f_s)t) . \tag{4.9}$$

Upon assuming the mixer as a multiplier and ignoring the terms that contains frequency f_c, the output of the mixer is given by,

$$z(t)=\frac{m(t)}{4}\sum_{l=1}^{L}\left\{e^{j(l-1)\varphi}\sum_{n=-\infty}^{\infty}\hat{c}_{nl}e^{j2\pi(n+1)f_s t}+e^{-j(l-1)\varphi}\sum_{n=-\infty}^{\infty}\hat{c}_{nl}e^{j2\pi(n-1)f_s t}\right\} \tag{4.10}$$

where $\hat{c}_{nl}$ is the new coefficients due to the frequency dependence of the combiner, LNA and mixer. When $z(t)$ is passed through a LPF with bandwidth B_c where $B < B_c < f_s/2$, the only harmonics that pass through, are $n = \pm 1$ harmonics. Let us define the steering vector $\mathbf{s}$ by

$$\mathbf{s} = [1 \quad e^{j\varphi} \quad e^{2j\varphi} \ldots \quad e^{j(L-1)\varphi}]^T \tag{4.11}$$

and, $\mathbf{w}$ the weight vector by,

$$\mathbf{w} = [w_1 \quad w_2 \quad .... \quad w_L]^H \tag{4.12}$$

where w_l is equal to $\hat{c}_{-1,l}$ and using (4.6) it is given by

$$w_l = \frac{\rho(\alpha_1 - \alpha_2)}{\pi}\sin(\pi\tau_l)e^{j\pi(2t_{sl}+\tau_l)} \tag{4.13}$$

Then, the output of the LPF is given by

$$m_o(t) = m(t)\,\mathrm{Re}\{\mathbf{w}^{\mathrm{H}}\mathbf{s}\} \tag{4.14}$$

where, the factor ρ takes into account the effect of the combiner, the LNA, the mixer and the LPF. The normalized magnitude and phase of the weight w_l are, respectively, given by,

$$|w_l|_n = \sin(\pi\tau_l) \tag{4.15}$$

and

$$\angle w_l = (2t_{sl} + \tau_l)\pi . \tag{4.16}$$

As can be seen, τ_l may be adjusted to control the weight amplitude and with a fixed τ_l, t_{sl} can be adjusted to realize the weight phase. The unity normalized amplitude happens with $\tau_l = 1/2$ and to realize the amplitude variation in the range $0 \le |w_l|_n \le 1$, τ_l should be varied in the range $0 \le \tau_l \le 1/2$. The delay time of the pulses (t_{sl}) is allowed to vary in the interval $[0,1]$ to realize the phase shift in the range $[\pi\tau_l, \pi(2+\tau_l)]$. The pulse width τ_l should be accounted for in determining t_{sl} when realizing the phase shift. Therefore, the pulse width and starting time for the sampling pulse on the antenna elements $l = 1,2,...,L$ can be obtained as

$$\tau_l = \frac{1}{\pi}\sin^{-1}(|w_l|_n) \tag{4.17}$$

and

$$t_{sl} = \frac{\angle w_l}{2\pi} - \frac{\tau_l}{2} . \tag{4.18}$$

Figure 4.2 from top to bottom shows the spectrum of the signal arriving over the l^{th} element, the switched signal, and the signal at the mixer's output, respectively. As can be seen, different replicas of the signal are generated after switching. The amplitude of each harmonic depends on the pulse width. In Figure 4.1(a) the power combiner, the LNA and the mixer center frequency are tuned to $f_c - f_s$ rather than f_c. Therefore, in Figure 4.2, the replicas other than $f_c - f_s$ at the output of the mixer are attenuated due to the frequency dependence of the combiners, the LNA and the mixer.

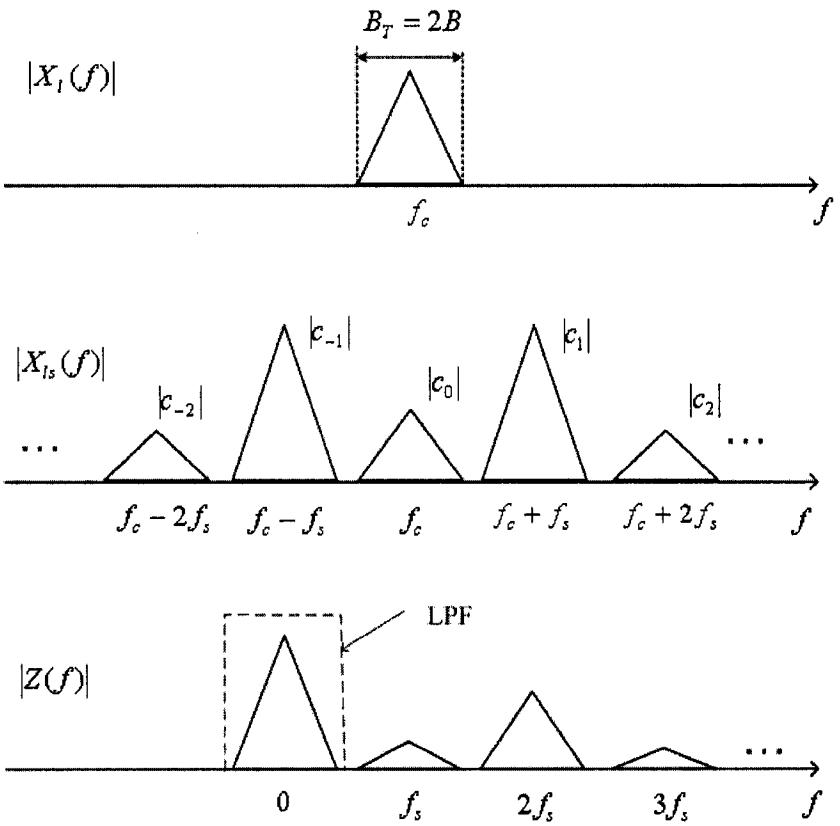

Figure 4.2 Frequency domain representation of the signals.

The amount of power in each replica depends on the harmonic number and the parameters τ_l, α_1 and α_2. The maximum output power for the desired harmonic ($n = \pm 1$) happens when $\alpha_1 = 1$ and $\alpha_2 = -1$. This switch is not a common one, i.e. $\alpha_2 = -1$ instead of 0. In the Sub-section 4.2.4, a new switch design is proposed to accomplish such a switching. Considering the harmonics in the lower sideband, when $\alpha_1 = 1$ and $\alpha_2 = -1$, the maximum output power happens for signal replicas around frequencies $f_c - f_s$ and f_c when $\tau_l \geq 0.17$ and $\tau_l \leq 0.17$, respectively. When $\tau_l \geq 0.2$, the

replica around $f_c - 2f_s$ has more power than the replica around f_c. In the design of the LPF, it should be noted that for $\tau_l \leq 0.17$ a replica stronger than the desired replica should be cancelled. Since the center frequency of the power combiner, LNA and mixer is on $f_c - f_s$ rather than on f_c, this will lower the burden of the LPF. There is a limitation on the bandwidth of the proposed structure. As mentioned earlier the switching frequency should be higher than the transmission bandwidth of the impinging signal. Therefore, existence of switches with small switching time is critical for the proposed structure. Currently, PIN diodes with switching time of the order of few nanoseconds are available which allows bandwidth of the order of tens of MHz.

4.2.3 Transmitter structure

In the transmit mode the same principle works. Figure 4.3 shows the transmitter. In this structure at first the message signal $m(t)$ is modulated by the carrier frequency $f_c - f_s$ rather than f_c. This signal is divided between antenna elements using power divider. Each signal is switched by a proper pulse train to apply the required phase shift and amplitude weighting. Similar to the receiver structure the first harmonic of the switched signal is used for weighting, but the center frequency is up-converted to f_c in this case. At the output of switches, BPFs select the replica around f_c as the desired transmitted signal. It is important that the overall frequency response of the antenna and/or BPF effectively rejects other harmonics to prevent interference with other communication systems.

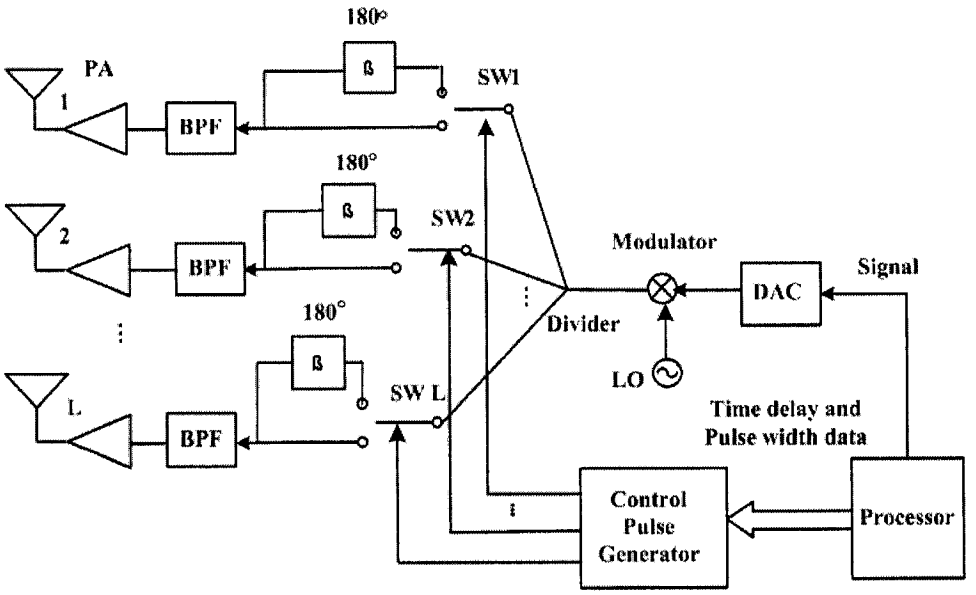

Figure 4.3 An MSBF transmitter structure.

4.2.4 Switch design

In each antenna element, shown in Figure 4.1 (a) and Figure 4.3, a single pole double throw switch (SPDT) combined with a 180° phase shift in one branch is used. In this part the reason for this design is discussed. Using a single-pole single-throw (SPST) switch such as a single PIN diode it is possible to switch the RF signal from zero level ($\alpha_2 = 0$) to a high level ($\alpha_1 = 1$) and vice versa. However, with $\alpha_2 = 0$ there is a loss factor of around -10dB in the proposed structure due to the factor $1/\pi$ in (4.13), which is a high loss. When $\alpha_2 = -1$, from (4.13) the amplitude of the desired harmonic is doubled and the loss factor decreases to -3.9dB. It should be noted that this loss factor is applied to both the signal and noise and it does not lead to a noise figure increase similar to the common attenuators. Details of the effect of this loss on the signal to noise ratio are discussed in Section 4.4.

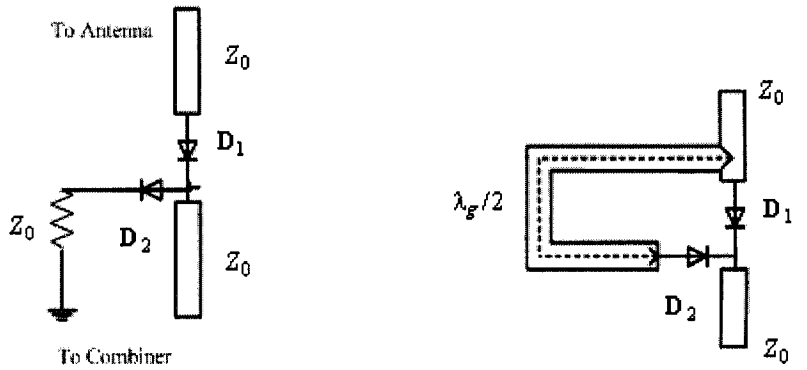

(a) (b)

Figure 4.4 Always matched switches. (a) Passes the RF signal in one state. (b) Passes RF signal in both states.

In addition, it is important that the combiner terminals always should be matched. When one antenna is OFF the corresponding combiner terminal loses matching and this reduces the overall performance of the system. Figure 4.4 (a) shows a switch design that satisfies the "always matched" condition. In Figure 4.4 (a) diode $\mathbf{D}_1$ and $\mathbf{D}_2$ are biased oppositely. Diode $\mathbf{D}_2$ is connected to the ground using impedance Z_0. When $\mathbf{D}_1$ is OFF the other diode connects the impedance Z_0 to the combiner port. While the switch circuit in Figure 4.4(a) satisfies the always matched condition, it still exerts the aforementioned -10dB loss on the desired replica.

Figure 4.4 (b) shows another switch design that satisfies the "always matched" condition. In this circuit both diodes are connected in parallel and they are biased oppositely and one diode is in series with a 180° phase shifter. When $\mathbf{D}_1$ is ON, it passes the RF signal, but when $\mathbf{D}_2$ is ON, it passes the phase shifted RF signal. In fact, this switch is a phase switch. The overall performance of this phase switch can be modeled

with a multiplicative pulse shown in Figure 4.1(b) which has $\alpha_1 = 1, \alpha_2 = -1$. Therefore, this switch design has the loss factor of around -3.9dB. In Figure 4.4 (b) for 180° phase shift a $\lambda_g / 2$ transmission line is used, but any type of phase shifter could be used. Also, in Figure 4.4 (b), to maintain the "always matched" condition, both diodes are located at the end or beginning of two parallel arms and the length difference between two arms should be $\lambda_g / 2$. With this condition, when one diode is off, the equivalent impedance seen from the other end of the corresponding line is infinity or open circuit and so the impedance seen by the ON diode is always Z_0.

4.3 Validation using Microstrip Antenna Array

A four-element inset-feed microstrip antenna array is used to validate MSBF structure in the transmit mode. The four-element microstrip patch antenna with inset feed is designed to work at f=5.8GHz. Element spacing is considered to be $\lambda_0 / 2$ where λ_0 is the free space wavelength. The substrate used for the antenna and combiner is Duroid with parameters $\varepsilon_r = 2.33, h = 62\text{mil}, \tan\delta = 0.002$. The antenna elements are designed and optimized using Ansoft HFSS software to obtain good matching at the center frequency.

The effect of switches and combiner are modeled by switching pulses. For the up-converting mixer a multiplier is used. The switching frequency is assumed to be 10MHz and a single frequency message signal at $f_m = 2\text{MHz}$ is used. For the bandpass filters, Butterworth filters with bandwidth of 4MHz, band stop of 10MHz and 30dB loss at the stopband are used. Except the antenna array that is simulated using HFSS, the rest of the system is simulated using ADS harmonic balance analysis.

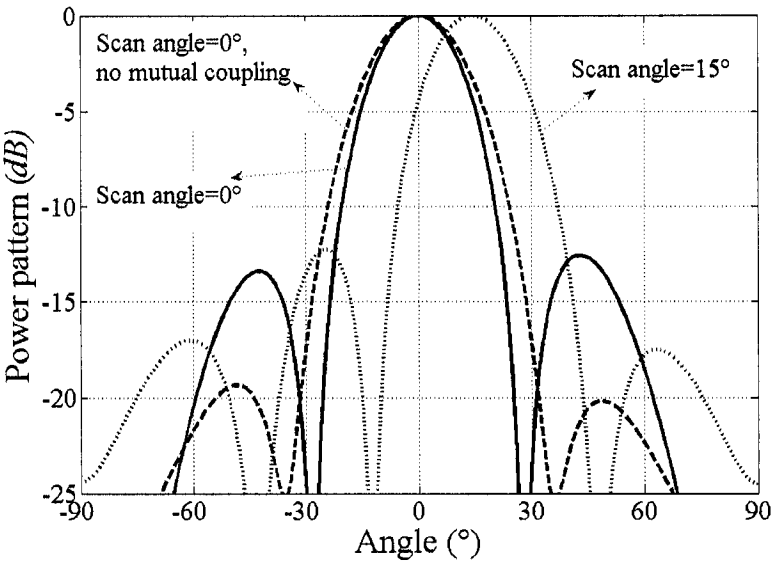

Figure 4.5 Uniform amplitude array radiation pattern of the four element microstrip patch array for two scan angles.

Pulse width and delay are computed to model a four-element uniform and Chebyshev array with -30 dB sidelobe level at two different scan angles of 0° and 15°. Figure 4.5 shows the radiation pattern for the uniform array when proper pulses are produced and applied to the switches. The increase in sidelobe level by scanning in Figure 4.5 is due to the mutual coupling between antenna elements and the error in the weight calculations. The radiation pattern without mutual coupling effect is also plotted to demonstrate the ability of maintaining the amplitude weighting using the adjusted pulse widths. The decrease in sidelobe level in this curve is due to the element pattern. The little asymmetry in this curve is due to the error in the weight calculation; while a rise time of $2ns$ and a fall time of $3ns$ are considered for the sampling pulse, for the weight calculations it is ignored. Figure 4.6 shows that pattern for -30dB Chebyshev SLL

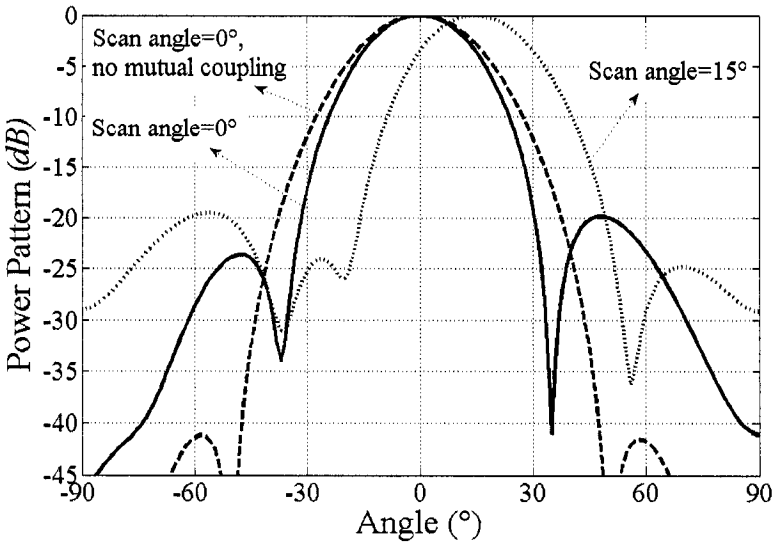

Figure 4.6 Radiation pattern of the four element microstrip patch array for two scan angles with -30dB Chebyshev amplitude excitation.

control. The same trend as in Figure 4.5 can be observed in this figure; the pattern is scanned to the proper angle; SLL is increased by mutual coupling; SLL is reduced by the element pattern.

4.4 Validation Using Wire Antennas

In this part an eight element $\lambda_0/2$ dipole array with element spacing of $\lambda_0/2$ is considered to verify the MSBF performance in the receive mode. The array antenna is modeled with the NEC2 software [111]. A plane wave with varying incident angle is impinging over the antenna array. The current induced in the antenna elements for different incident angles are transferred to the Matlab software where the receiver is modeled. The carrier, sampling and message frequencies considered are 2.48GHz, 20MHz, and4MHz, respectively. The control pulses are generated using Matlab to realize -30dB Chebyshev patterns for three scan angles $-20^\circ, 0^\circ$ and 30° using an eight-element

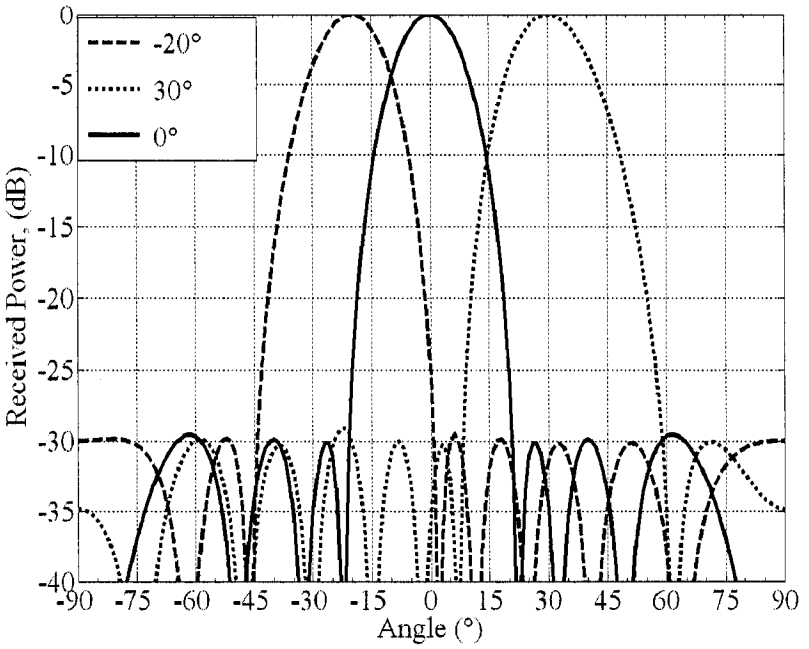

Figure 4.7 Synthesized radiation patterns using isotropic array elements.

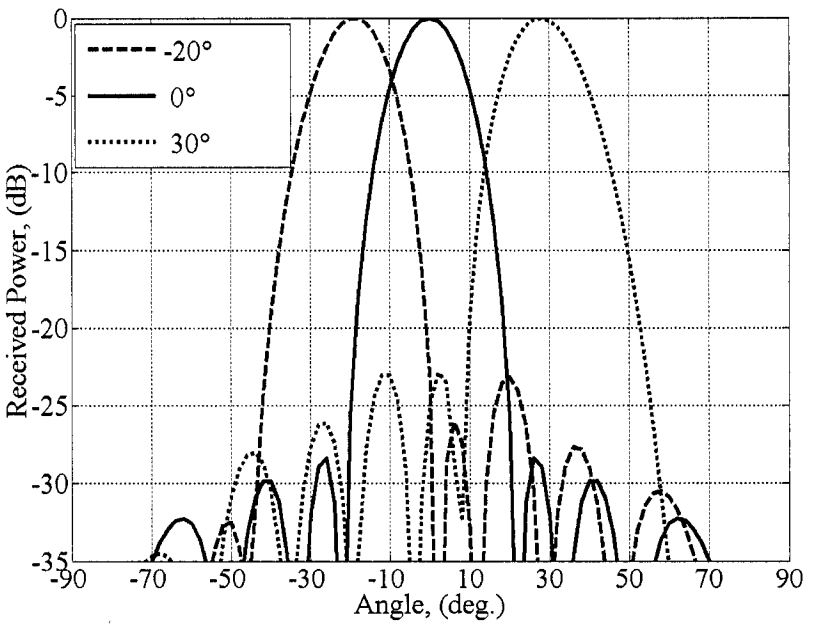

Figure 4.8 Synthesized radiation patterns including the mutual coupling effect.

MSBF structure. Figure 4.7 shows the synthesized patterns for the three scan angles. Figure 4.8 shows the same patterns as in Figure 4.7, but the effect of mutual coupling is also included. As can be seen, in both figures the patterns are scanned to the proper angles. The increase in side lobe level with scan angle in Figure 4.8 is due to mutual coupling between elements.

In this part, the SNR performance of the MSBF structure is compared with that of a single antenna system and a multiple antenna system without coherent signal combining (simple combining). In each case the impinging signal on each antenna element has a desired signal and a white noise component. The weight vector for a conventional beamformer is applied to the array in the MSBF structure for coherent combining. Figure 4.9 shows the transmitted message signal (desired signal) and the received signal for the three receiver structures when desired signal is impinged from 30° measured from the broadside. The loss of the MSBF structure in each branch is considered 6dB, but that of the other two receivers is considered 3dB. Higher loss encompasses the loss in switches after each element. In Figure 4.9, the top curve shows the message signal which is the summation of the three harmonics of a 500kHz rectangular pulse. The second curve from the top shows the output of single antenna receiver. The third curve from the top shows the output of multiple antenna system without coherent combining and the last one shows the output of the MSBF structure with coherent combining. As can be seen from Figure 4.9, the new structure has completely recovered the message, but the other systems have been affected by noise.

4.5 SNR Analysis and Weight Quantization

4.5.1 SNR

In this part the MSBF structure signal to noise ratio performance is investigated for different channel scenarios. A parameter that determines the SNR performance of any receiver is the insertion loss. In the MSBF structure there are two different kinds of losses that should be differently considered. The first kind of loss includes transmission lines,

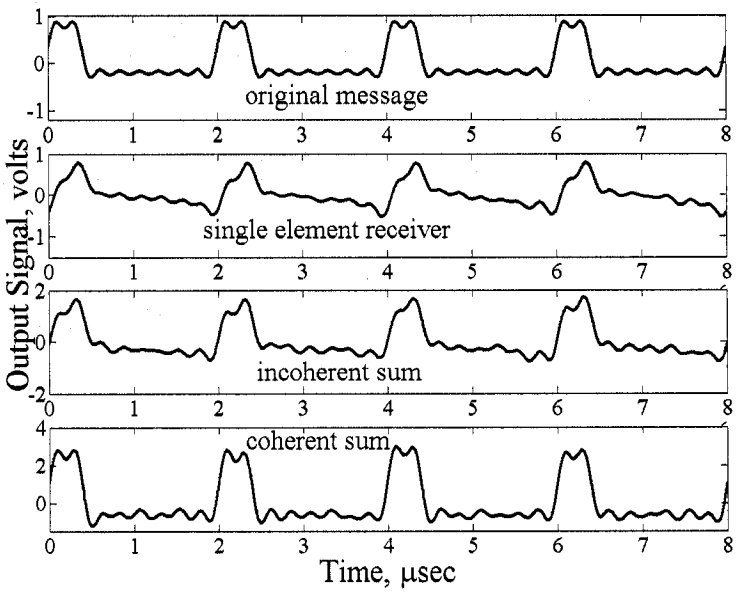

Figure 4.9 Output signals of the three receivers with an impinging angle of 30°.

combiner and switches losses. These losses exist for any MBF structure and clearly increase the noise figure of the system by the amount of loss (assuming that system is in thermal equilibrium and complete match) [113]. However, due to using just one PIN diode at each time interval the loss in the weighting element is very low.

The second kind of loss is the loss due to the amplitude weighting in each element, where each element signal is attenuated by $2\sin(\pi\tau)/\pi$ where τ is the pulse

width. The effect of this loss is quite different from the first one. For this type of loss, all signals including input noise and even noise produced in the switches experience the same attenuation due to the switching of both signal and noise. Therefore, this loss does not directly lead to a noise figure increase. This is an important property of the MSBF structure that the controlled attenuation attenuates the input noise as well. This is not the case for other attenuators.

The following analysis is based on using passive switches. While in this work PIN diodes have been studied as switches to validate the proposed "always matched" condition, they are not fundamental to the proposed technique. In [57], active switches have been used to introduce some gain in the switching and also to increase the switching speed. Using these switches may result in integrating the process of amplification and phase-amplitude weighting in one block. In this analysis, it is assumed that PIN diodes and Wilkinson combiners are employed in the system as switches and combiners, respectively. Also, it is assumed that the noise of each switch can be modeled by its insertion loss. The total power loss factor from the antenna to the combiner output can be represented by L_t. It is assumed that the antenna noise temperature is equal to the physical temperature of the receiver. This assumption is acceptable for systems whose antenna's look direction is toward ground [2]. For applications such as satellite communication, active switches with some gain should be employed instead of passive switches.

Assume that the signal and noise over antenna elements after the LNA are represented by complex vectors $\mathbf{x}$ and $\mathbf{n}$. Under thermal equilibrium and matching conditions, the combiner output can be written as

$$y = \frac{1}{\sqrt{L_t L}} \mathbf{w}^H \mathbf{x} + \frac{1}{\sqrt{L}} \mathbf{w}^H \mathbf{n} \tag{4.19}$$

where $\mathbf{w}$ is the weight vector of the array and the factor $1/\sqrt{L}$ is the combiner transmission coefficient magnitude. The weights to receive the signal from the look direction with a specified amplitude tapering, $\mathbf{w}$ can be written as

$$\mathbf{w} = \frac{2}{\pi}[a_1, a_2 e^{j\varphi}, ..., a_L e^{j(L-1)\varphi}]^T \tag{4.20}$$

where

$$a_l = \sin(\pi\tau_l) \tag{4.21}$$

In the above formulation, the noise of each PIN diode is attenuated by the factor $\sin(\pi\tau)/\pi$ independently. As a result the reduction factor of the total switch noise is more than that of the signal. This effect is ignored in the above formulation. On the other hand, the noise produced in the combiner is not attenuated as the other noises do, but this effect is ignored because the combiner loss is a small fraction of the total loss. Based on (19) and the above discussion, the signal to noise ratio at the output of combiner can be written as

$$SNR_o = \frac{(\sum_{l=1}^{L} a_l)^2}{L_t \sum_{l=1}^{L} a_l^2} \frac{P_s}{P_n} \tag{4.22}$$

or

$$SNR_o = \frac{(\sum_{l=1}^{L} a_l)^2}{L_t \sum_{l=1}^{L} a_l^2} SNR_i \,. \qquad (4.23)$$

In a channel where there are just signal and background noise, the optimum amplitude tapering is uniform tapering or conventional beam-former and the SNR gain is L / L_t. In [53] for an array of four elements with PIN diode switches and combiners of almost the same branch length, the total branch loss is measured to be around 1.7dB. Therefore, it is possible to obtain a SNR gain of more than 4 dB with four elements. When the number of elements increases the loss factor does not increase linearly because the switch and transmission line losses remain constant and only combiner loss increases. For an eight element array with 2dB loss it is possible to obtain 7dB gain.

In a real communication channel with some directional interference sources, using null forming and side-lobe control, the array gain can be much higher. Also, in the proposed structure, antenna element signals are weighted with high resolution phase shifters and combined in the analog domain that allows forming deep nulls. The null bandwidth of this structure is the same as that of general phase shifters and is lower than that of true time delay phase shifters. However, for smart antennas which have few elements and with higher center frequencies, it is possible to obtain considerable null depth and bandwidth. Moreover, the DIS experiences the same loss factor L_t as the desired signal in this structure.

As an example for the effects of null steering on the array gain, let's consider a four-element array and a channel with two equal power directional interference sources.

Suppose, $SNR_i = 20dB$ and $SIR_i = 2dB$ or $SINR_i = 1.6dB$. Making 30dB nulls in the direction of interference, which is possible for this structure, results in $SINR_o$ of around 22dB or an array gain of more than 20dB. For the above channel with -30dB SLL it is possible to obtain an overall array gain of around 20dB. For this SLL control, minimum amplitude tapering of -7dB or relative pulse width of 0.14 is required. For a system with a transmission bandwidth of 10MHz, a switch with 14ns switching time is required to obtain such amplitude tapering which is possible with current PIN diode technology.

4.5.2 Weight quantization

Weight quantization for the MSBF structure is different from other structures. Digital phase shifters and gain control elements are generally quantized linearly. However, in the MSBF structure, the time delay and pulse width are quantized instead of the signal phase and amplitude. In addition, because the amplitude attenuation in (4.15) is a sinusoidal function of the pulse width, the amplitude quantization is not linear. Therefore, for a ν bits pulse-width resolution, the normalized quantized pulse-width levels and the corresponding quantized amplitude levels are given by $(i-1)/2^{\nu+1}$ and $\sin(\pi(i-1)/2^{\nu+1})$, respectively, where $1 \le i \le 2^{\nu}$. With this amplitude quantization, the amplitude resolution is higher than linear quantization for high amplitude levels and lower for small amplitude levels. To quantize the time delay, the phase shift is varied in a manner to obtain the time delay in a fixed range, say [0, 1]. Therefore, the normalized time delay quantization levels are $i/2^{\nu}$, where $1 \le i \le 2^{\nu}$ which is a linear quantization.

It is important to calculate the quantized time delays in such a way to make the phase quantization error independent of the pulse width quantization error. In applying a weight to an element, first the pulse width is obtained using (4.17) with the corresponding quantized pulse width. Next, based on the weight phase, the time delay is calculated from (4.18) which is also related to the pulse width. If a quantized pulse width instead of the calculated pulse width is used in (4.18), the phase quantization error becomes independent of the pulse width quantization error. In addition, because the normalized time delay for each element is varied over [0, 1], the phase shift for the l^{th} element is chosen in the range$[\pi\tau_{lq}, \pi(2+\tau_{lq})]$, where τ_{lq} is the quantized pulse width for the l^{th} element. Therefore, the phase quantization levels are different for different elements. This makes the quantized phase shift for each element different from the general digitized phase shifts. Depending on the calculated analog weight vector and the number of quantization bits, it is observed that quantization using pulse width and time delay may lead to a higher or lower quantization error compared to direct quantization of the phase and amplitude.

4.6 MSBF with Finite Duration Pulse Train

The effectiveness of any ABF or DOA estimation technique depends on the algorithm employed for weight vector calculation and the way it is applied to the array. One issue in most ABF algorithms for single-port structures is that they are slower in convergence than algorithms for multi-port structures. In addition, the total convergence time is directly proportional to the time duration that each weight vector is applied to the array. Therefore, it is useful to enhance and speed up the application of the calculated weight vector.

The analysis presented in [105] and Section 4.2 was based on using an infinite length periodic sampling pulse train as control signal in each antenna element. However, using an infinite pulse train implies applying a fixed weight vector which makes it impractical for updating the weight vector temporarily. Assume that a weight vector is applied in the time duration $[0,T]$ and updated afterwards. In this case, a control signal $\hat{p}_l(t)$ similar to the infinite length pulse train $p_l(t)$ in Section 4.2, but zero outside $[0,T]$ is applied to the l^{th} antenna element. The Fourier series representation of $\hat{p}_l(t)$ is given by

$$\hat{p}_l(t) = \prod\left(\frac{t-T/2}{T}\right)\sum_{n=-\infty}^{n=\infty} c_{nl}e^{j2\pi nf_s t} \tag{4.24}$$

where c_{nl} is given by (4.6) and $\Pi(\cdot)$ represents the rectangular function. Therefore, the total signal at the output of the combiner is given by

$$y(t) = \prod\left(\frac{t-T/2}{T}\right)\sum_{l=1}^{L}\sum_{n=-\infty}^{n=\infty} c_{nl}e^{j2\pi nf_s t}x_l(t)\ . \tag{4.25}$$

The effect of the term $\prod\left(\frac{t-T/2}{T}\right)$ can be included by changing the message signal $m(t)$ to $m_T(t) = m(t)\prod\left(\frac{t-T/2}{T}\right)$ whose Fourier transform is given by

$$M_T(f) = F\left\{m(t)\prod\left(\frac{t-T/2}{T}\right)\right\} = Te^{-j\pi fT}\mathrm{sinc}(fT) * M(f)\,. \tag{4.26}$$

In (4.26), the operator F represents Fourier transform, $(*)$ represents convolution operation and $M(f)$ is the Fourier transform of the message signal $m(t)$. Based on (4.25) and (4.26) there are infinite replicas of the signal $M_T(f)$ which are spaced by f_s. In order to avoid overlapping of different replicas, the sampling frequency should satisfy

$f_s \geq 2B_1$ where B_1 is the bandwidth of $M_T(f)$. Assuming that the effective bandwidth of $\text{sinc}(fT)$ is α/T, and the bandwidth of $M(f)$ is $B_T/2 = B$, the bandwidth of $M_T(f)$ becomes $B_1 = \alpha/T + B_T/2$. The parameter α determines the number of lobes in the effective bandwidth of $\text{sinc}(fT)$. A value of unity for α is sufficient because more than 90 percent of the *sinc* function power is in its first lobe. Therefore, the transmission bandwidth of each replica is increased from B_T to $2B_1 = (2\alpha/T + B_T)$ which requires increasing the bandwidth of the structure between the switches and the LPF. The weighting duration is represented in terms of the signal bandwidth by $T = \beta/B$ where β determines weighting duration normalized to $1/B$. In order to reconstruct just one replica of the signal, the sampling frequency should satisfy $f_s \geq 2B_1$ or

$$f_s \geq (1 + \alpha/\beta)B_T. \tag{4.27}$$

Based on (4.27), in order to decrease the weighting duration (decreasing β), the sampling frequency should be increased.

As discussed in Chapters 2 and 3, perturbation techniques should be used to obtain the gradient vector or array covariance matrix for the ABF or DOA estimation. In any perturbation technique, each adaptation cycle is composed of multiple perturbation cycles. For an ABF algorithm which converges in M iteration cycles and uses Q perturbations in each iteration cycle, the total adaptation time is $T_{tot} = MQT$. Therefore, it is desirable to decrease the weighting interval T to decrease the overall convergence time. On the other hand, based on (4.27), decreasing T or β necessitates increasing f_s, which is limited by the switching time of the PIN diodes. Therefore, availability of fast

PIN diode switches is critical for this structure and a compromise should be made between T and f_s. In addition, there is an image replica in the structure which affects the performance of the structure as f_s increases. In the next section, this image replica is introduced and a technique to remove it is presented.

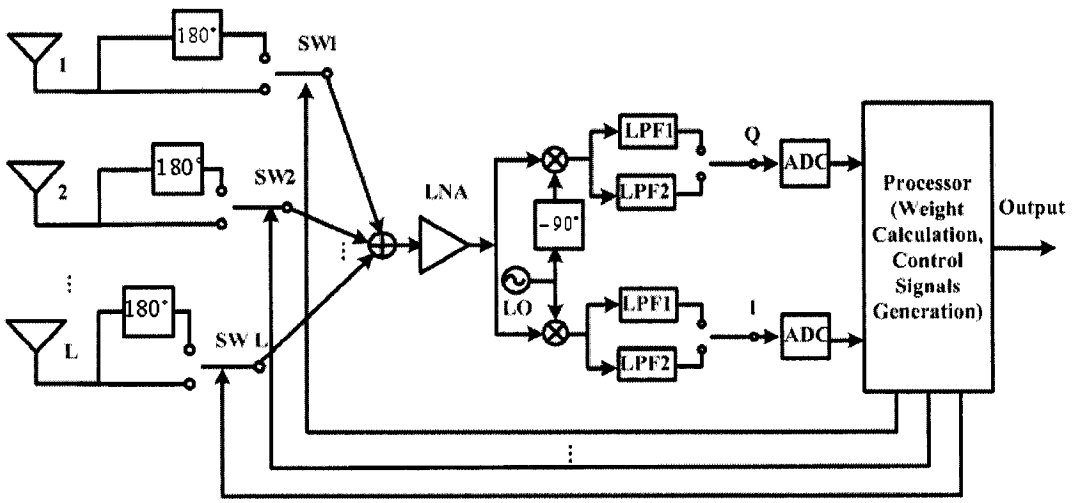

Figure 4.10 An MSBF structure with finite duration pulse trains.

Figure 4.10 shows a MSBF structure when fast weight control is desired which works in two modes: adaptation mode and normal mode. In the adaptation mode, the weights are updated fast and the pulse train duration T is small. In order to recover the signal in the adaptation mode, the receiver bandwidth should be more than f_s and the LPF cutoff frequency should satisfy $B_1 \le B_{c1} \le f_s - B_1$ where, $B_1 = \alpha / T + B_T / 2$. As shown in Figure 4.10, the LPF1 is used for this purpose. The output signals are sampled at a time instant $t = t_0$ away from the edge transients. Both $y_I(t_0)$ and $y_Q(t_0)$ are required in the processor to carry out complex operations such as gradient vector estimation and

weight vector calculation on the output signal. In the normal mode, it is assumed that the adaptive algorithm is converged and the weights are fixed for much longer time duration or the pulse trains are periodic. Therefore, the output signal bandwidth is $B_T/2$ and the second LPF (LPF2) cutoff frequency satisfies $B_T/2 \le B_{c2} \le f_s - B_T/2$. In this mode, samples of $y_I(t)$ and $y_Q(t)$ are used to extract the signal information.

4.7 Image Replica and Rejection Technique

4.7.1 Image replica definition and effect

As discussed in Section 4.2, it is desired to select the replica centered at $f_c - f_s$ which is generated through mixing of the input signal with the first harmonic of the control signal. However, if the control signal spectrum includes a harmonic at $2f_c - f_s$, it will be also translated to $f_c - f_s$ through mixing with the input signal which is modulated on f_c. Figure 4.11 (a)-(d) illustrates the schematic spectra of the impinging signal at one antenna element, the control signal, the switch output signal, and the mixer output signal, respectively. Because the image replica is the image of the desired replica with respect to a mirror located at f_c, it is called 'image replica' as shown in Figure 4.11 (b). In Figure 4.11 (c) the signal replicas bandwidths are expanded due to the finite length sampling pulse train. In addition, after switching of the antenna signals, an undesired replica overlaps the desired replica as shown in Figure 4.11 (c). This is due to the assumption that there is a harmonic of the sampling pulse train at $2f_c - f_s$ as shown in Figure 4.11 (b). In Figure 4.11 (d) the mixer output is shown which illustrates the overlapping of the image replica and the desired replica at in baseband. If the image replica is generated in the weighting process, it corresponds to the n^{th} harmonic of the

sampling pulse train when $2f_c - f_s = nf_s$ where n is given by

$$n = 2f_c / f_s - 1. \tag{4.28}$$

Therefore, if $2f_c / f_s$ is an integer, this replica exists and overlaps totally the desired replica totally. The amplitude and phase of the image replica for each element are determined from (4.6) with n determined from (4.28). The image replicas from different elements generate another pattern which is combined with the desired pattern. Therefore the equivalent weight vector given in (4.13) is modified to

$$\mathbf{w} = [c_{11} + c_{n1}, c_{12} + c_{n2}, ..., c_{1L} + c_{nL}]^{\mathrm{T}}. \tag{4.29}$$

In (4.29) due to different phase and amplitude variations of the desired replica and the image replica coefficients with pulse width and time delay, the desired pattern is distorted. In fact, the beam formed by the desired replica has different nulls, sidelobe region and pointing directions than the one formed by the image replica. Therefore, the image replica pattern deteriorates the desired replica pattern and particularly in the null and sidelobe region. Using (4.6) the ratio of the image replica amplitude over the desired replica amplitude is inversely proportional to n. Therefore, based on (4.28) with not a high f_c / f_s, n is small which intensifies the effect of the image replica. For a system with a fixed fractional bandwidth $b = B_T / f_c$, based on $f_s \geq (1 + \alpha / \beta) B_T$, the ratio f_c / f_s is limited by $f_c / f_s \leq \beta / b(\beta + \alpha)$. Therefore, based on (4.28), n is bounded by

$$n \leq 2\beta / b(\beta + \alpha) - 1 \tag{4.30}$$

which is inversely proportional to the fractional bandwidth. As the fractional bandwidth (γ) increases and the pulse train duration (β) decreases, n decreases which intensifies

the effect of the image replicas. Therefore, with fast weighting rate (small β values), the effect of the image replica is reinforced. With $\beta = 1, \alpha = 1$ and b=0.05, n is less than 20. Considering only the attenuation by the factor $1/n$ in (4.29), the image replica is attenuated by 26dB more than the desired replica. When low sidelobe level (SLL) and

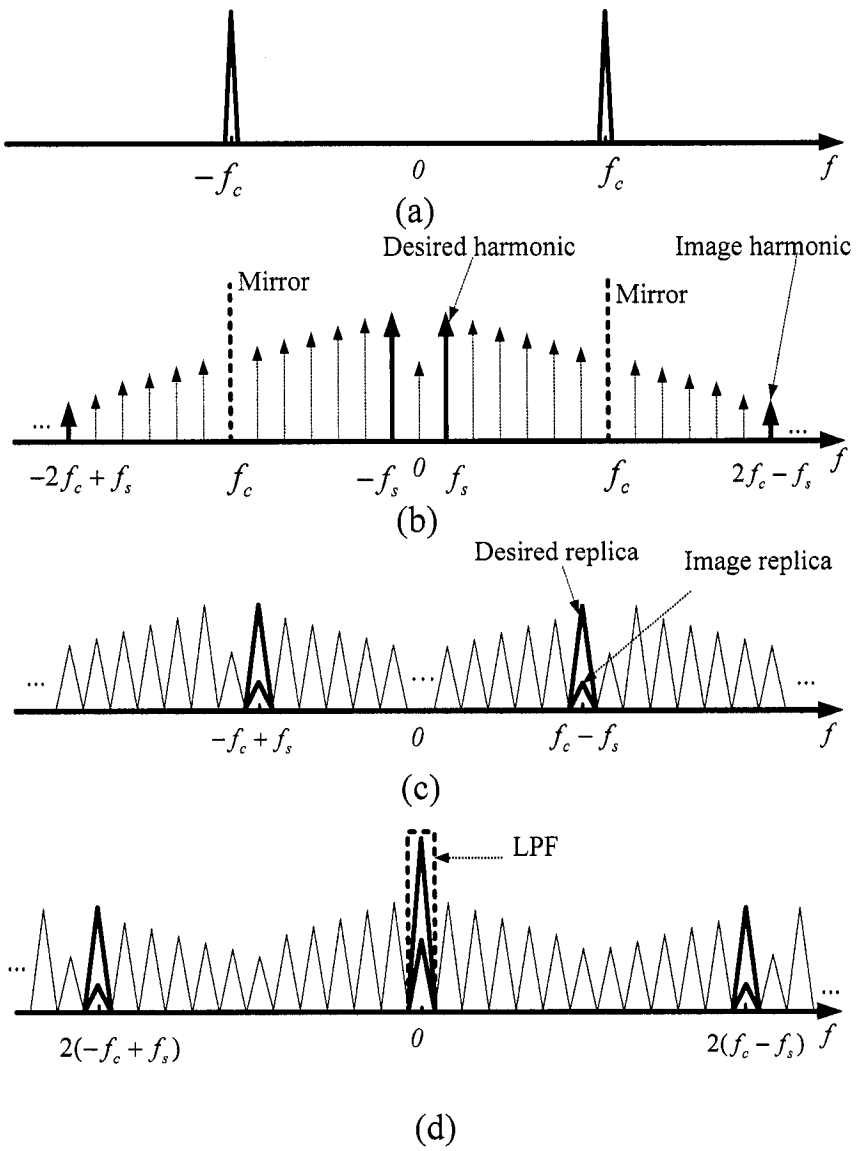

Figure 4.11 (a) Signal spectrum on one antenna element. (b) Sampling pulse train spectrum on one antenna element. (c) Signal spectrum at the output of one switch. (d) Mixer output.

deep nulls are necessary, this amount of loss is not sufficient and the image replica should be cancelled.

When $2f_c / f_s$ is not an integer, no replica with the center frequency at $2f_c - f_s$ exists, but the desired replica is still distorted because each replica has a bandwidth. In fact, any frequency component in the range $[2f_c - f_s - B_1, 2f_c - f_s + B_1]$ which is shown in Figure 4.12 as the 'forbidden band' overlaps the desired replica after switching. When $f_s = 2B_1$, the tails of the two replicas adjacent to the image frequency $2f_c - f_s$ overlap partially the forbidden band. In this case, the lower part of the desired output signal is combined with the weight vector $\mathbf{w} = [c_{11} + c_{(n_0-1),1}, c_{12} + c_{(n_0-1),2}, \ldots, c_{1L} + c_{(n_0-1),L}]^{\mathrm{T}}$ and the upper part with the weight vector $\mathbf{w} = [c_{11} + c_{n_0 1}, c_{12} + c_{n_0 2}, \ldots, c_{1L} + c_{n_0 L}]^{\mathrm{T}}$ where, n_0 is the smallest integer larger than n. Therefore, this overlapping still affects the pattern generated by the desired replica. In addition, because in different frequency ranges the array signals are combined with different weights, the output signal is also distorted spectrally.

4.7.2 Image replica rejection

To resolve the image replica issue, first the ratio $2f_c / f_s$ is set to a non-integer value to remove any replica on $2f_c - f_s$. In addition, f_c and f_s are controlled to place the image frequency $2f_c - f_s$ in the middle of two adjacent replicas. This is achieved by placing $2f_c - f_s$ in the middle of the $(n_0 - 1)^{th}$ and $n_0{}^{th}$ replicas by

$$2f_c - f_s = ((n_0 - 1)f_s + n_0 f_s)/2 \tag{4.31}$$

which gives

$$f_c = (2n_0 + 1)f_s / 4. \tag{4.32}$$

Figure 4.12 (a) shows the location of the image frequency, adjacent replicas and the forbidden band when the two adjacent replicas are symmetric around the image frequency and $f_s = 2B_1$. As can be seen, half of each replica still overlaps the forbidden band because the bandwidth of each replica is $2B_1$ and the space between the $(n_0 - 1)^{th}$ and n_0^{th} replicas is f_s. However, by increasing f_s the difference between two replicas increases and as a result the overlapping with forbidden band decreases. In particular, as shown in Figure 4.12 (b), there is no overlapping with the forbidden band when $f_s \geq 4B_1$, or

$$f_s \geq 2(1 + \alpha / \beta)B_T \tag{4.33}$$

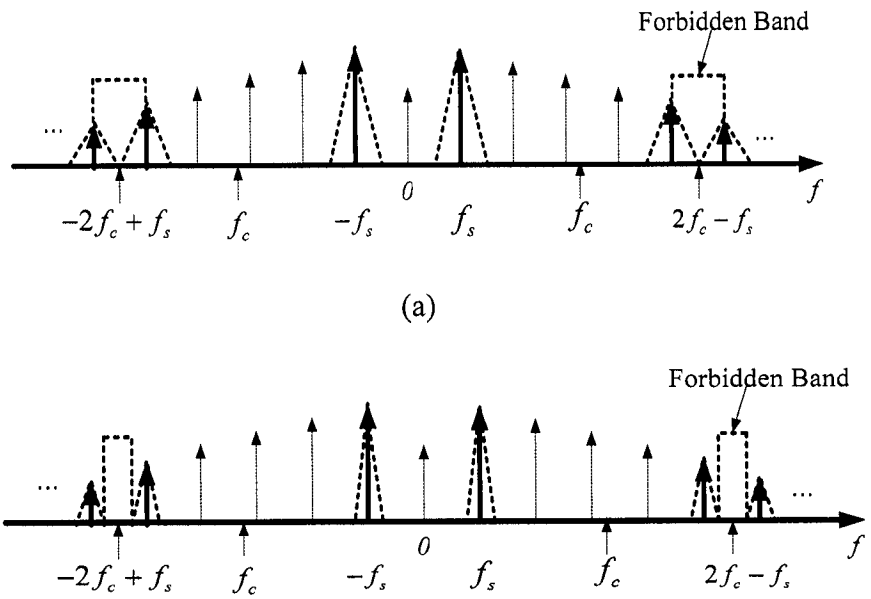

Figure 4.12 Image replica overlapping. (a) Using non-integer $2f_c / f_s$ and $f_s = 2B_1$. (b) Using $f_s = 4B_1$ and $f_c = (2n_0 + 1)f_s / 4$.

which is different from (4.27) by a factor 2. Therefore, by choosing the carrier and sampling frequencies to satisfy both (4.31) and (4.32) the image replica is totally removed. When the structure is working in the normal mode, the sampling frequency should satisfy $f_s \geq 2B_T$ for image rejection instead of the Nyquist condition $f_s \geq B_T$. A problem with (4.31) is that faster switches are required for image rejection because of the factor 2. However, as can be seen from (4.33), increasing the pulse train duration (β) lowers the requirement on the sampling frequency. In practice, a compromise should be made between the sampling frequency and the weighting rate.

4.8 Simulation Results

In all simulations the whole MSBF structure is simulated in the time domain including the transients of the filters. The array signals and finite duration control pulses with proper time delay and the pulse width are generated in the time domain. For more realistic simulations, standard filters are employed and their impulse responses are used in the simulations. The mixer and switches are assumed ideal multipliers. For the training signal, a filtered pulse train with 11 harmonics is considered where its 11^{th} harmonic frequency equals the signal bandwidth. To model the array pattern in the receiving mode, the power of the signals I and Q are sampled and combined as a function of the scanning angle similar to what is performed in a measurement lab. A four element isotropic antenna array with half wavelength spacing is considered in the simulations. Isotropic array elements are assumed in the simulations to focus mainly on issues related to the structure.

4.8.1 Finite pulse train and sampling frequency

4.8.1.1 SLL control

To study the relation between the pulse train duration and the sampling frequency for sidelobe control, a -40dB SLL Chebyshev pattern directed at 10° is modeled with the structure. The LPF bandwidth is considered $f_s/2$ and the pulse width and time delay are quantized with eight bits. A high carrier frequency ($f_c = 100B_T$) is considered in the simulations to ignore the effect of the image replica. Figure 4.13 (a) shows the normalized output power pattern with the pulse train duration $T = 0.5/B$ ($\beta = 0.5$), and different sampling frequencies ($f_s = 1.5B_T, 2B_T$ and $3B_T$).The desired pattern is shown as 'ideal' in this figure for comparison. With $\beta = 0.5$, these sampling frequencies are equivalent to $\alpha = 0.25, 0.5$ and 1, respectively. As can be seen from Figure 4.13 (a), SLL is high for $f_s = 1.5B_T$, but it is reduced by increasing f_s. Another issue in Figure 4.13 (a) is that there is around 6dB increase in SLL with $f_s = 3B_T$. However, based on (4.27), using $\beta = 0.5$, $f_s = 3B_T$ is equivalent to $\alpha = 1$ which should be sufficient to apply the weight effectively. This is due to the effect of the image replica which was discussed in Section 4.7.

Figure 4.13 (b) shows the normalized output power monitored at the output of the structure for $f_s = 1.5B_T$, and for different pulse trains durations. As can be seen the pattern approaches the ideal pattern as the pulse train duration increases. With $\beta = 1$, there is only 2dB increase in the SLL. Based on (4.27) and with $f_s = 1.5B_T$, using $\beta = 0.6, 0.8$ and 1 is equivalent to considering $\alpha = 0.3, 0.4$ and 0.5. Comparing

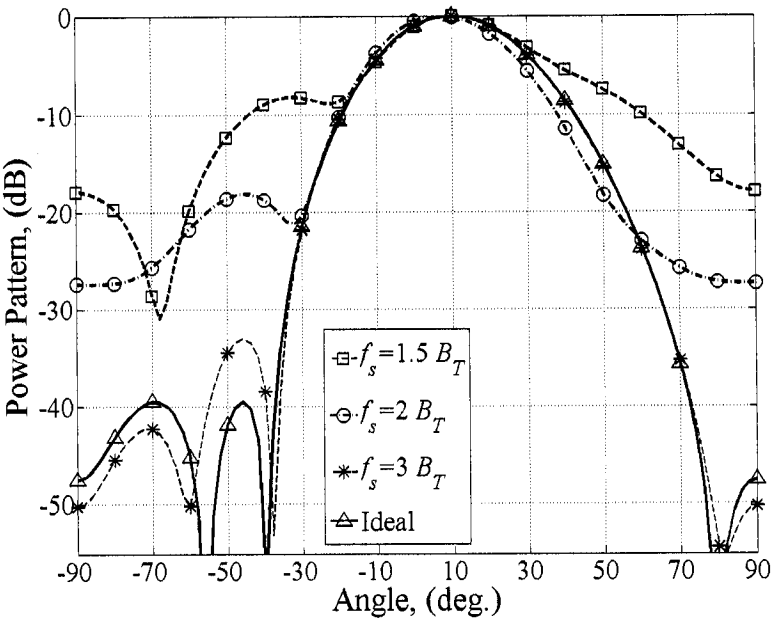

(a)

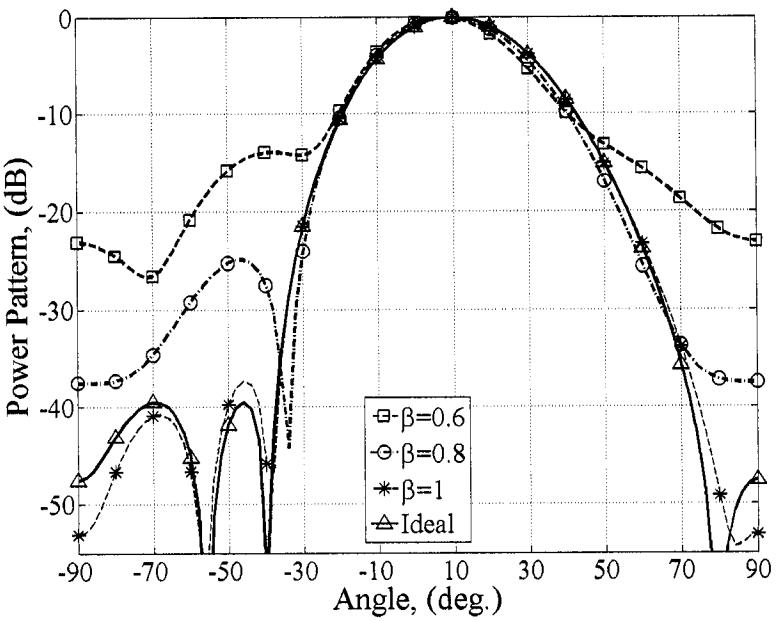

(b)

Figure 4.13 Effect of the sampling frequency and pulse train duration on SLL control. (a) Using fixed pulse train duration ($\beta = 0.5$) and different sampling frequencies. (b) Using fixed sampling frequency ($f_s = 1.5B_T$) and different pulse train durations.

Figure 4.13 (a) and (b), it can be seen that the performance with $\alpha = 1 (f_s = 3B_T, \beta = 0.5)$ is worse than $\alpha = 0.5 (f_s = 1.5B_T, \beta = 1)$. This is due to a higher f_c / f_s ratio with $f_s = 1.5B_T$ which lowers the image replica effect. In fact, if the image replica is not controlled, a large sampling frequency may not necessarily improve the weighting performance.

4.8.1.2 Null-forming

To study the effect of the finite pulse train on null-forming capability, the optimum weight vector for a channel with three interference sources impinging from directions $-60°, 20°$ and $50°$ and the desired signal from $-20°$ is applied to the array. The signal to interference power ratio (SIR) for each interfering source is -10dB and the signal to noise ratio (SNR) is 10dB. In practice the weight vector is calculated adaptively , but in this work the focus is only on applying the weight vector effectively. Therefore, it is assumed that the optimum weight vector is known in the receiver. Similar to the SLL control example, the weights are quantized with eight bits and $f_c = 100B_T$. Figure 4.14 (a) shows the pattern for different sampling frequencies and with $\beta = 0.5$. The same trend as for the SLL control example can be observed. For $f_s = 1.5B_T$, the nulls are removed from the pattern, but as the sampling frequency increases, the nulls are deepened. Figure 4.14 (b) shows the power pattern with $f_s = 1.5B_T$, but with different pulse train durations ($\beta = 0.6, 0.8$ and 1). As can be seen, by increasing the pulse width duration, the pattern approaches the ideal pattern. Moreover, similar to the SLL example, the performance with $\alpha = 1 (f_s = 3B_T, \beta = 0.5)$ is worse than $\alpha = 0.5 (f_s = 1.5B_T, \beta = 1)$ due to the image

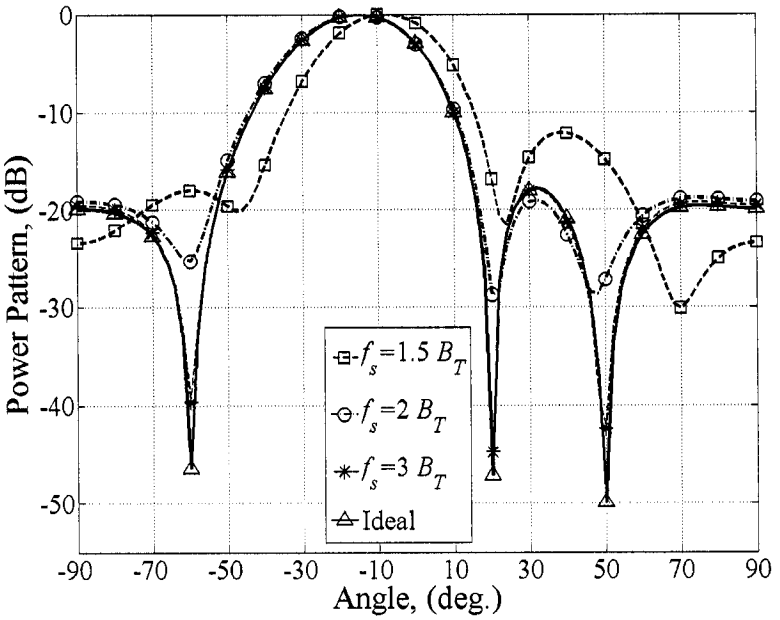

(a)

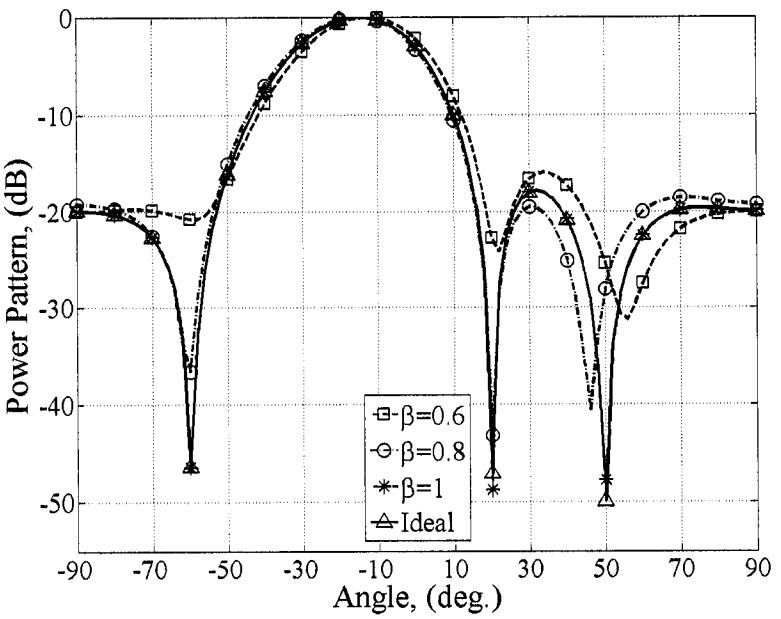

(b)

Figure 4.14 Effect of the sampling frequency and pulse train duration on null-forming. (a) Using fixed pulse train duration ($\beta = 0.5$) and different sampling frequencies. (b) Using fixed sampling frequency ($f_s = 1.5B_T$) and different pulse train durations.

replica effect. This image replica issue is investigated in more detail in the next sub-section.

4.8.2 Image replica

4.8.2.1 Effect of the image replica

In this part, the effect of the image replica on the MSBF structure is studied using SLL control and null-forming examples. In order to focus only on the image replica issue, high resolution weights (12 bits) are applied to the array to minimize the quantization errors. Figure 4.15 (a) shows the pattern achieved when the weight vector is aimed to have a -40dB Chebyshev pattern toward -10° direction and the carrier frequency is an integer multiple of the sampling frequency ($f_c = 5f_s$ $f_c = 10f_s$ $f_c = 25f_s$). For comparison the aimed pattern is shown as 'ideal' pattern in this figure. With these carrier frequencies, the image replica overlaps the desired replica. An eighth order Bessel LPF filter is used in the modeling. The sampling frequency, LPF bandwidth and pulse train duration are considered $4B_T$, $2B_T$ and $1/B$ ($\beta = 1$), respectively. With $f_s = 4B_T$, the carrier frequencies $f_c = 5f_s$ $f_c = 10f_s$, and $f_c = 25f_s$ are equivalent to the fractional bandwidths 5%, 2.5% and 1%, respectively. As can be seen from Figure 4.15 (a), for $f_c = 5f_s$ and $f_c = 10f_s$ the pattern SLL increases by around 18dB and 10dB, respectively. For $f_c = 25f_s$, the pattern SLL approaches that of the desired pastern, but the pattern shape has changed. Figure 4.15 (b) shows the pattern for the null-forming example in Figure 4.14, but with sampling and carrier frequencies used in Figure 4.15 (a). As can be seen from Figure 4.15 (b) for $f_c = 5f_s$ $f_c = 10f_s$ and $f_c = 25f_s$ the null depths in the directions ($[-60^{\circ}, 20^{\circ}, 50^{\circ}]$) are lowered by around ([45dB, 35dB, 30dB]), ([37dB,

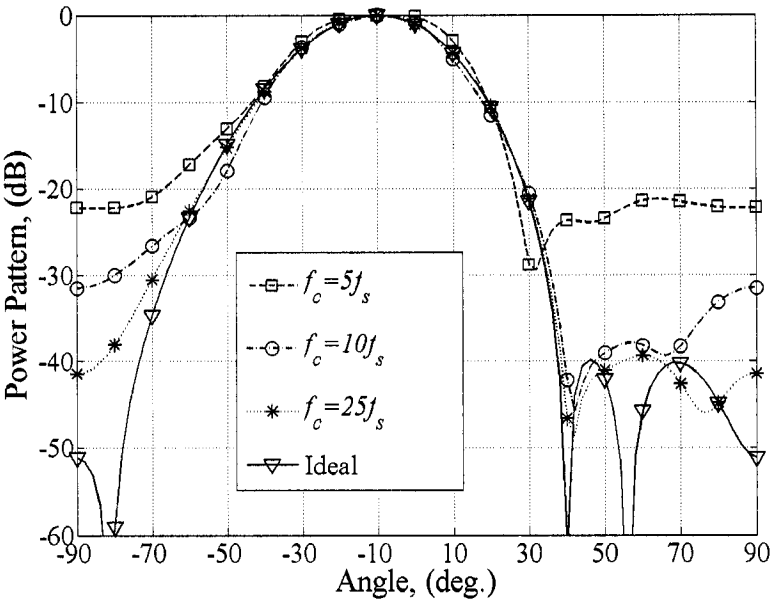

(a)

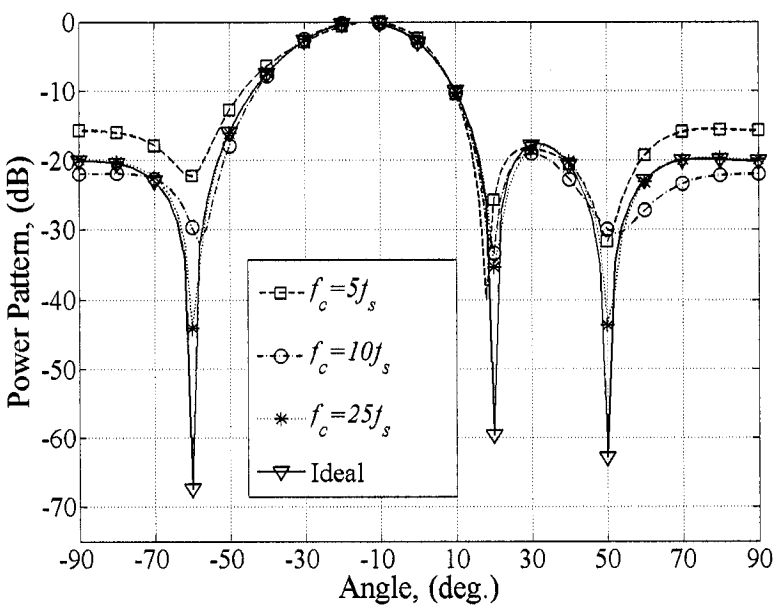

(b)

Figure 4.15 Study of the image replica effects. (a) SLL control example. (b) Null-forming example.

27dB, 32dB]) and ([23dB, 25dB, 24dB]), respectively. Based on Figure 4.15 (a) and (b), the image replica greatly deteriorates the SLL control and null-forming capability of the MSBF structure for high f_c / f_s ratio, if not controlled. Moreover, the null-forming capability of the structure is more affected than the SLL control capability.

4.8.2.2 Image replica rejection

In this part the effectiveness of the image replica rejection technique discussed in Section 4.7, is investigated. Figure 4.16 (a) shows the same pattern as in Figure 4.15 (a), but for different carrier and sampling frequencies. For all graphs the fractional bandwidth is fixed at five percent and the LPF bandwidth (B_1) is considered B_T. In Figure 4.16 (a) the power pattern is plotted when $f_s = 2B_T$ and $f_c = 10 f_s$ which means an image replica overlaps the desired replica. In this case the sampling frequency is two times the effective signal bandwidth ($f_s = 2B_1$). As can be seen, there is around 8dB increase in the SLL. Another pattern is shown by modifying the carrier frequency to $f_c = 9.75 f_s$ which obtained from (4.32) by using $n_0 = 19$. With this carrier frequency, there is no replica at $2f_c - f_s$ and the closest replicas are symmetrically located on both sides. The pattern is significantly improved while f_c / f_s ratio is even lowered. In this case there is around 2dB increase in the SLL. For the third graph, the sampling frequency is increased to $f_s = 4B_T$ to have $f_s = 4B_1$, but f_c is chosen an integer multiple of f_s ($f_c = 5 f_s$). In this case f_c is equal to the first case ($f_c = 10 f_s, f_s = 2B_T$) because fractional bandwidth is fixed and the sampling frequency is doubled. As can be seen, in this case the SLL is increased by 18dB which is due to small f_c / f_s ratio and overlapping of the image

replica. For the fourth graph, carrier and sampling frequencies are chosen $f_c = 4.75 f_s$ and $f_s = 4B_1$, respectively, to satisfy both image rejection conditions in (4.31) and (4.32). As can be seen, there is no increase in SLL in this case. Figure 4.16 (b) shows a null-forming example with the channel scenario used in Figure 4.15 (b) and the image rejection technique used in Figure 4.16 (a). The same improvement as in Figure 4.16 (a) can be observed. As can be seen, by just controlling the relation between the sampling frequency and the carrier frequency ($f_c = 9.75 f_s$), the nulls are deepened by around 10dB to 15dB. The improvement by satisfying both image rejection conditions ($f_c = 4.75 f_s$ and $f_s = 4B_1$) is more significant than for SLL control. A trend in this case is that the performance is even superior to the desired pattern. This is due to different weight quantization techniques used for weighting of the reference pattern (ideal pattern) and the pattern using MSBF structure. As discussed in sub-section 4.5.2 the weight quantization for MSBF structure is different because the time delay and pulse width are quantized instead of the phase shift and amplitude.

4.8.3 Effects of the receiver frequency dependence

In this part the effect of the frequency dependence of the structure is studied. As discussed before the receiver and the LPF filter bandwidths should be increased during adaptation mode because the bandwidth of the signal increases. Figure 4.17 shows the output power pattern for $f_s = 3B_T$, $\beta = 1$ and different LPF bandwidths. A high carrier frequency ($f_c = 100 B_T$) which makes $2f_c / f_s$ a non-integer value, is considered in the simulations to have ignorable image replica. It is assumed that the receiver bandwidth before the mixer is equal to the LPF bandwidth. The frequency dependence of the

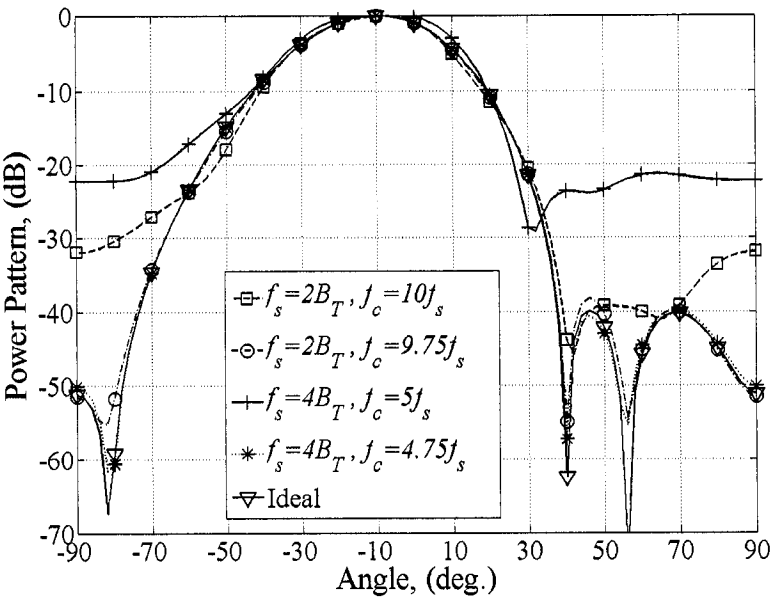

(a)

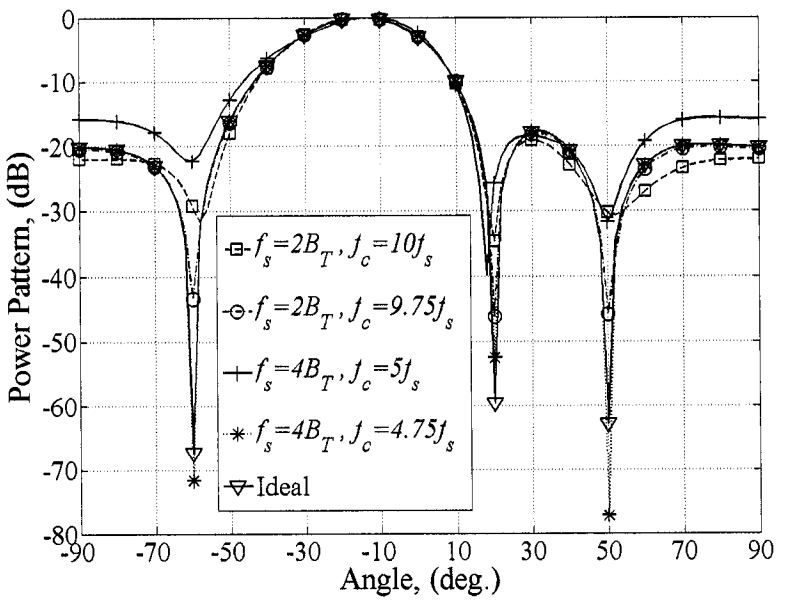

(b)

Figure 4.16 Study of image replica rejection. (a) SLL control example. (b) Null-forming example.

structure before the mixer is modeled by a second order Bessel type BPF and the LPF is an eighth order Bessel filter. As can be seen, for $B_1 = B$, the null depths are limited by around 10dB. In addition, by increasing the LPF bandwidth to $f_s/2 = 3B$ the power pattern approaches the ideal case.

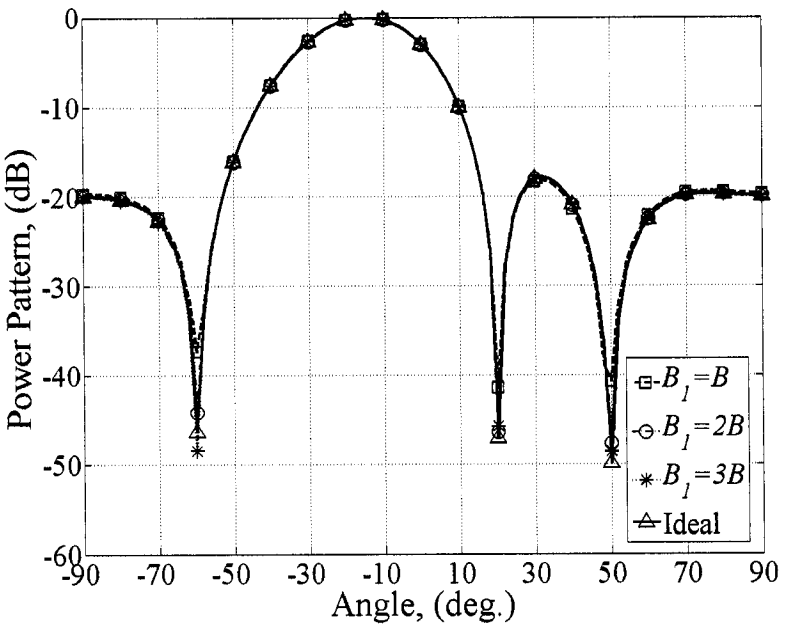

Figure 4.17 Study of LPF bandwidths.

Figure 4.18 shows the same pattern as in Figure 4.17, but for different BPF types used before the mixer. In this way, the sensitivity of the structure to the frequency response of the structure before the mixer is investigated. Different standard BPF types such as Butterworth, Chebyshev I, Chebyshev II, and Bessel are studied. For Chebyshev I, the ripple level in the passband is considered 0.1dB, and for Chebyshev II the attenuation in the stopband is considered 50dB. The bandwidth of the receiver before the mixer is considered two times the LPF bandwidth. As can be seen, by changing the filter

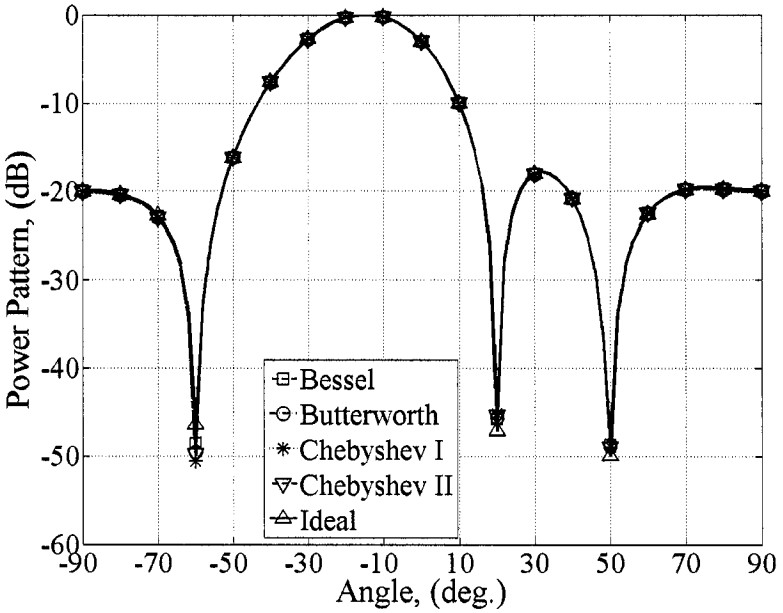

Figure 4.18 Study of the effects of receiver frequency dependence.

type the pattern does not change considerably. This verifies that through using a higher order LPF it is possible to control the frequency dependence of the whole structure mainly by the LPF response.

4.9 Conclusion

A novel technique for realizing phase-amplitude weighting for smart and phased array antennas is proposed. This technique lowers the complexity of the smart antenna system by using a simple block per antenna element to implement both amplitude and phase weighing using only one RF channel. For narrowband applications, this system can provide better performance due to the possibility of implementing phase shift and amplitude tapering with high resolution. A novel switch is designed to maintain a continuous impedance matching between antenna elements and the combiner. A four element antenna array is designed and simulated in the frequency domain to validate the

proposed structure. The proposed technique is also verified using an eight-element dipole array through integrating the NEC software with Matlab. A careful signal to noise ratio analysis of the proposed structure is carried out. Microwave sampling beamforming is modified for finite pulse train duration and image replica rejection. An image replica in the structure is introduced and a rejection technique is presented. A new limit on the sampling frequency and a relation between the sampling frequency and carrier frequency are obtained to reject the image replica. The structure with fast weighting rates is investigated for SLL control and null-forming. The structure is simulated in the time domain by considering a frequency response for the structure.

Chapter 5

Prototype Verification of the MSBF Structure

5.1 Introduction

In this chapter a prototype of the MSBF structure, composed of a four element microstrip patch antenna array with the proposed weighting technique is constructed and verified experimentally. A four branch control circuitry is also built which uses 12 bits pulse width and eight bits time delay resolutions. Therefore, the structure has the potential of 12 bits amplitude control and eight bits phase shift control. The MSBF structure is implemented with a switch design which is compact in size. In this regard, the switch biasing issues are investigated in depth and the switches are studied in the frequency domain using full–wave analysis and also in time domain. The structure scattering parameters are measured for different switching states. Different beamforming examples are examined with the prototype. A measurement setup using a spectrum analyzer and Lab-View programming is devised to study the pattern scanning of the structure. In Section 5.2 the implemented prototype is described. In Section 5.3 simulation and measurement results are presented. Finally, summary and conclusions are given in Section 5.4.

5.2 Prototype Description

5.2.1 Always matched switch

As discussed in [105] the switch in each branch should be always matched and have a 180° phase difference between two states. Figure 5.1 (a) shows the new switch

design where both diodes are controlled using one signal. Therefore, the biasing of the two opposite PIN diodes is dependent. In fact, if the PIN diode that is ON has a voltage V_γ, the other diode is reverse-biased by $-V_\gamma$, a small reverse bias voltage. This lowers the isolation of the OFF PIN diode which requires optimization of L_1, L_2, L_3, and L_4, shown in Figure 5.1(a), to control switch performance. In addition, because the size of the PIN diodes that are used in this design is small (14.4 mil long), the two arms in the $\lambda_g/2$ branch are very close. Therefore, the mutual coupling between these two arms degrades the switch performance.

The switch is optimized using Agilent ADS software package. The RO4350B substrate has parameters $\varepsilon_r = 3.66, h = 20mils$, and $\tan\delta = 0.0034$ and the HPND-4028 PIN diode is used in the design. In the design of this switch round lines are used to improve the performance. Quarter-wave 100Ω lines are used for RF and low frequency isolation. The effect of the biasing capacitors and ground vias are considered in the optimization. The switch is optimized to have high return loss and low insertion loss from both ports in the two switching states, and 180° insertion phase different between two states. To make the optimized design a realizable design, the radius of the curved branch is given by

$$R_0 = 0.5(L_1 + L_2 + L_d + W_1) \tag{5.1}$$

where $W_1 = 42.9$ mil is the width of the 50 ohm lines, and $L_d = 14.4$ mil is the length of the PIN diode. Satisfactory results are obtained for lengths $L_1 = 0.081\lambda_{g1}$, $L_2 = 0.083\lambda_{g1}$, $L_3 = 0.095\lambda_{g1}$, and $L_4 = 0.077\lambda_{g1}$ where $\lambda_{g1} = 1204.4$ mil is wavelength of the wave in the

50 ohm lines. For more accurate simulations the microstrip lines are modeled using ADS Momentum, whose results are combined with the lumped elements in the circuit simulation.

5.2.2 RF hardware integration

A photo of the system RF part is shown in Figure 5.1(b). A four-element microstrip patch antenna array with inset-feed is designed and optimized using the ANSOFT HFSS software package. In this work, to lower the hardware expenses a low-noise amplifier and band-pass filter (BPF) are not used after the antenna elements. Therefore, due to switching of the signals after each block, noise folding could happen. To lower the effect of the noise folding, an antenna with narrow bandwidth is used. For this reason and to integrate the antenna array and the beamforming circuit on the same planar board, the RO-4350B substrate with $h = 20$ mils, $\varepsilon_r = 3.66$, $\tan\delta = 0.0031$ is used. The single antenna patch was first designed and optimized for a low return loss and proper pattern at $f = 5.8GHz$. A return loss higher than 20dB was measured at $f = 5.8GHz$. Then, an array of these patches with $\lambda_0 / 2$ spacing, where λ_0 is the free space wavelength, was optimized for high return loss. The antenna array is constructed separately and its active element pattern and return loss are measured to make sure all elements are working at $f = 5.8GHz$. A return loss of around 14dB with 10dB bandwidth of 50MHz is measured. The antenna signals are combined using a corporate feed which is composed of three two-way Wilkinson combiners. The Wilkinson combiners were designed on $f_c - f_s = 5.7935GHz$, with $f_s = 6.49MHz$. For each two-way Wilkinson

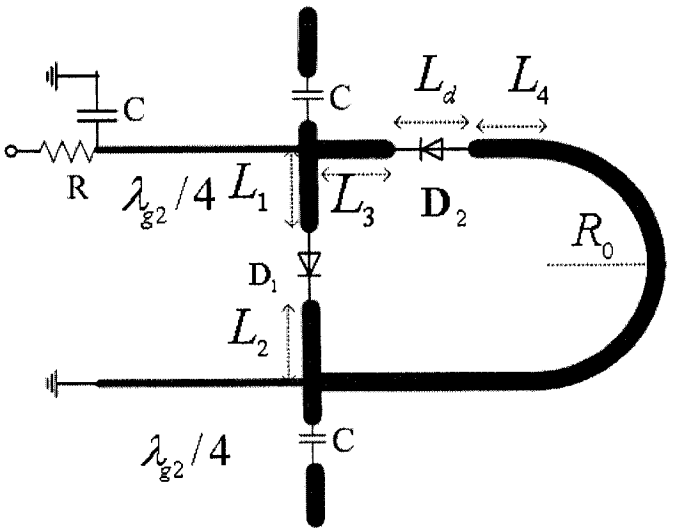

(a)

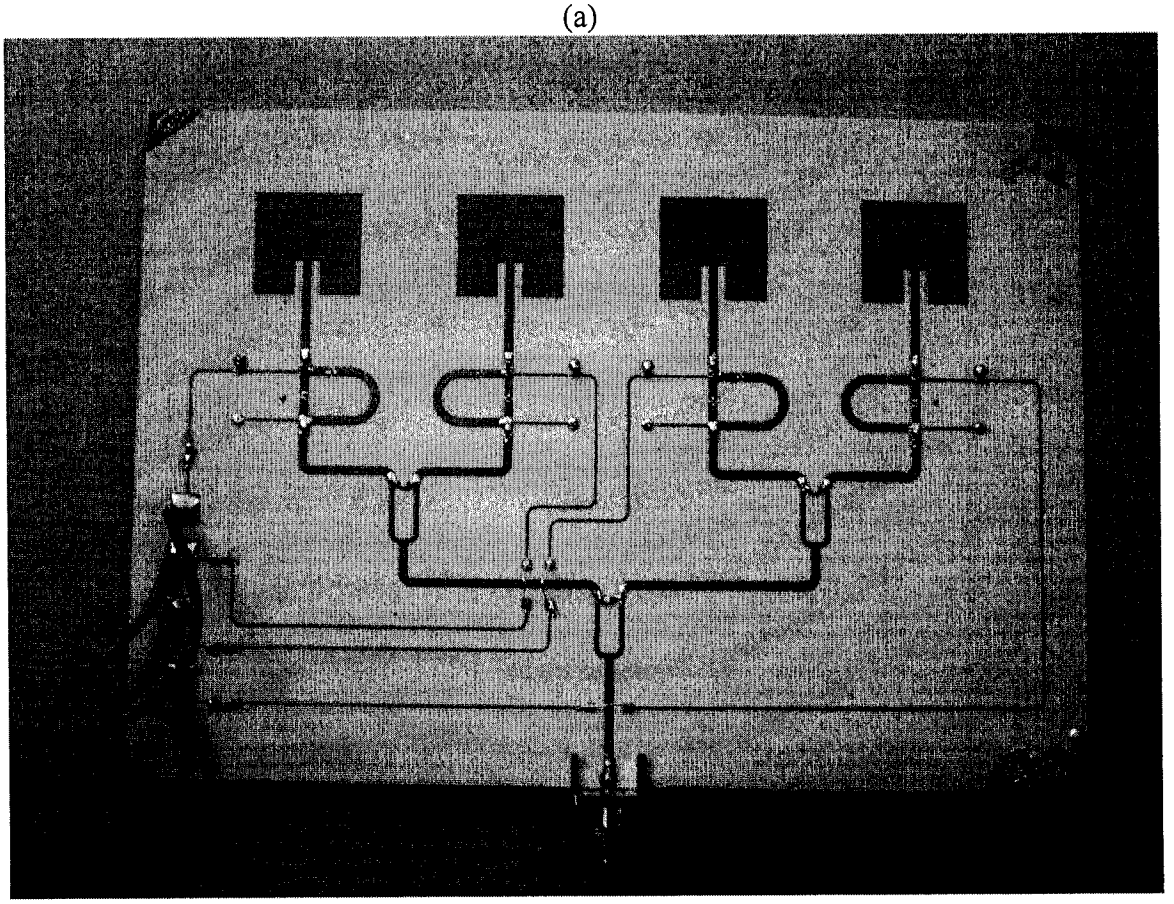

(b)

Figure 5.1 (a) New switch design with biasing circuit. (b) RF part of the system.

combiner, a measured return loss of 16dB, isolation of 18dB and insertion loss of 3.1dB were measured. The switch design in Figure 5.1(a) is integrated with the antenna array and combiners as can be seen in Figure 5.1 (b). The 18pF capacitors are used for DC coupling and RF bypass. A 270Ω resistor is used in each branch to protect the PIN diodes because the control voltage levels are 5 volts and -5 volts.

5.2.3 Control circuitry hardware

The control hardware generates four signals to control the switches. Figure 5.2 (a) and (b) show a block diagram and actual hardware of the control circuitry, respectively [114]. Each branch has a pulse width control block, a time delay block and a PIN driver IC. In order to have all branches synchronized, the same oscillator drives all four branches. In each branch, the pulse width is controlled and then the time delay. The outputs of the time delay ICs go through the PIN diode drivers to handle the high currents required during the ON-OFF transition of the PIN diodes.

For each pulse width control block the 3D7612W-0.25ns IC which is a 12-bit programmable pulse generator with pulse width step of 0.25 ns was used. The pulse width is adjusted using 12 bit binary inputs which can be also controlled directly using a processor. For a desired pulse width of τ in (ns), the address bits are found from the binary equivalence of

$$N_\tau = 4(\tau - t_{inh}) \tag{5.2}$$

where t_{inh}=14ns is the inherent pulse width which is achieved with all the address bits equal to zero. By using this IC, very high resolution amplitude control is achieved. The

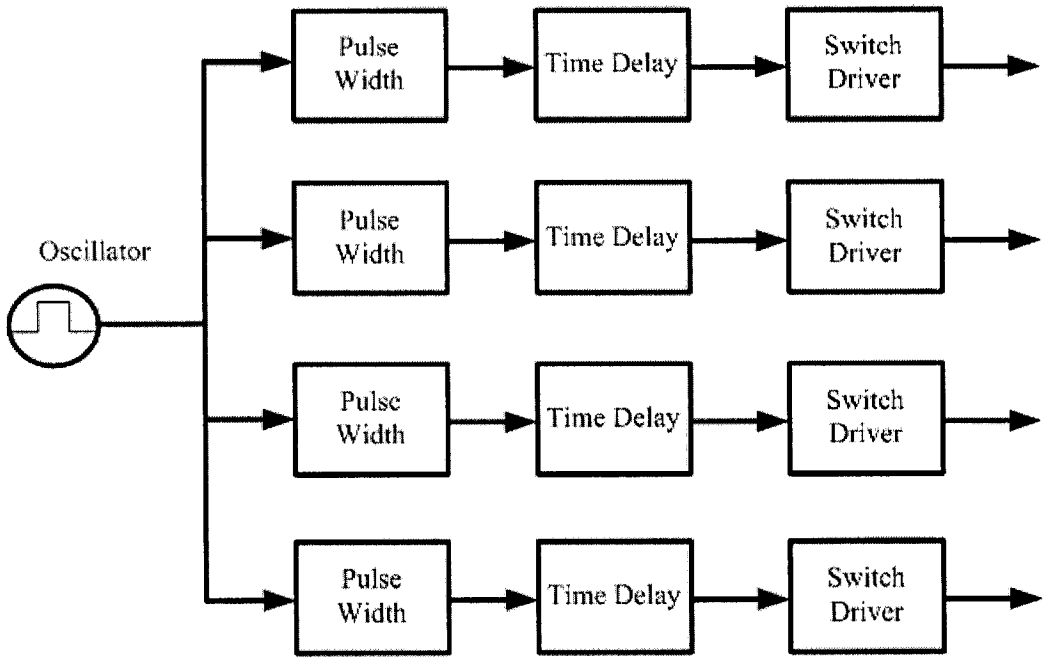

(a)

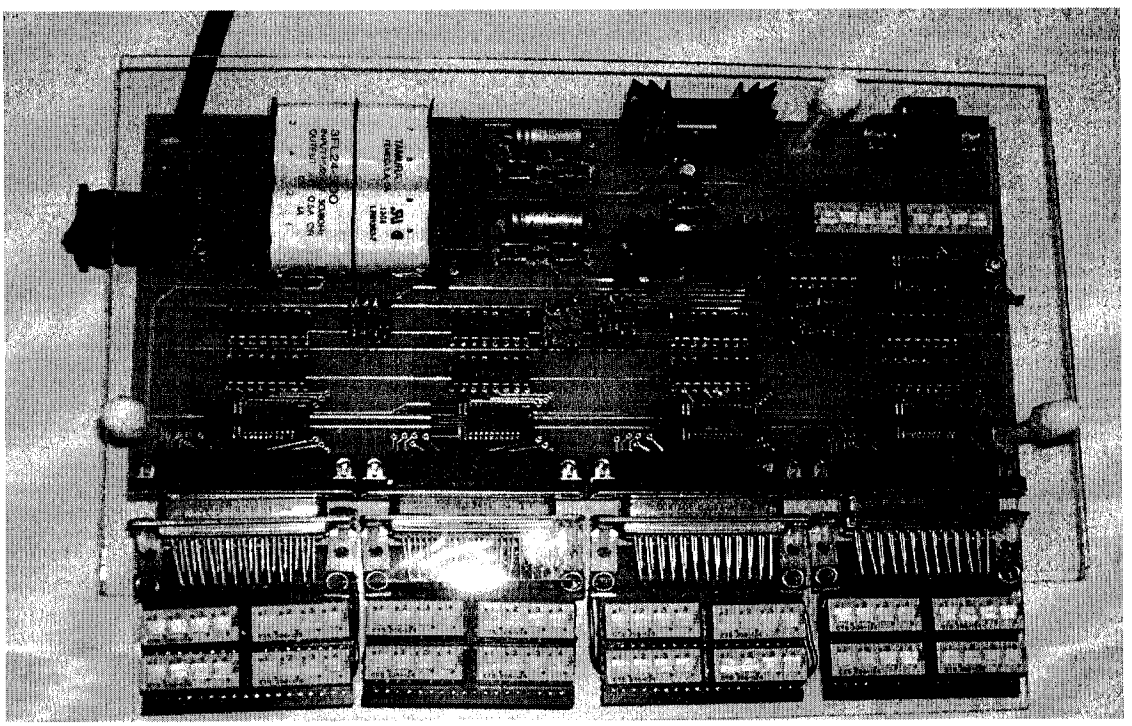

(b)

Figure 5.2 Control block. (a) Block diagram. (b) Actual circuitry [114].

pulse width address bits are set using dip switches. In this work, only eight bits of pulse width control ICs are used and two MSB and two LSB bits are set to zero for simplicity.

For the time delay generator, the 3D7428-1 IC is used which is an eight bit programmable delay line. The time delay values can be varied over 255 equal steps according to

$$t_d = t_{inh} + N_{td} t_{inc} \tag{5.3}$$

where $N_{td} \in [0,255]$ is the programmed address. t_{inc}=1 ns is the delay increment, and t_{inh} is the inherent (address zero) delay which is around 10.5ns. If the same IC is used in all branches, the effect of the inherent time delay can be ignored because the time delay difference between elements controls the phase shift in the MSBF structure. The high time delay resolution makes it possible to achieve high resolution phase shift in the MSBF structure. In this work, the time delay address bits are controlled using dip switches, but they can be also controlled directly using a DSP.

For each driver, a MSD 7800 PIN switch driver is used. This driver has a rise and fall time less than 10ns. The output resistance is measured to be around 200Ω.

5.3 Simulation and Measurement Results

5.3.1 Always matched switch

5.3.1.1 Frequency domain analysis

Figure 5.3 (a)-(c) show the S-parameters of the switch which are obtained using an ADS momentum full wave analysis. Since the phase switch is always ON, we define two states for the switch. In state one the switch transfers the RF signal and in state two it transfers the 180° phase shifted RF signal. Figure 5.3 (a) shows the magnitude of S_{11}

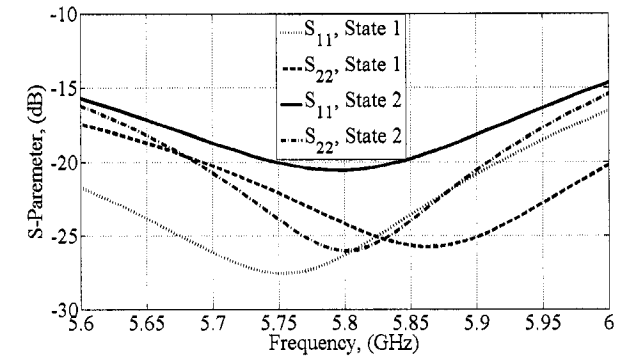

(a)

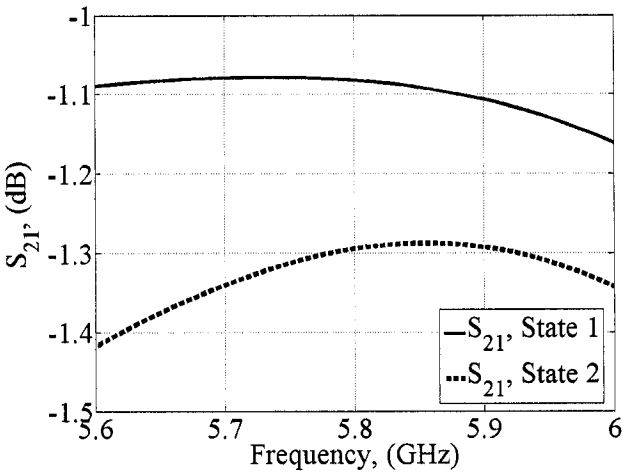

(b)

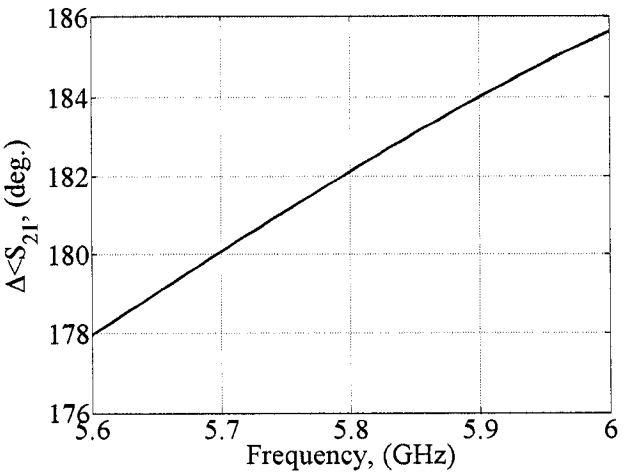

(c)

Figure 5.3 $S_{11}$and S_{22} in the two switching states. (b) S_{21} in two switching states. (c) Insertion phase difference between two states.

and S_{22} in dB for the new switch in states one and two. As can be seen, the switch achieves a return loss more than 15dB over a bandwidth of 400MHz in both states. Figure 5.3(b) shows the S_{21} of the switch for the two states. As can be seen, the average insertion loss of the switch is around 1.2dB. Figure 5.3(c) shows the insertion phase difference between the two states of the switch. The insertion phase achieved at 5.8 *GHz* is around 182°. It should be noted that this deviation from 180° only changes the insertion loss slightly and does not affect the phase shifting capability of the MSBF structure. The linear variation of the insertion phase is due to using a transmission line for 180° phase shift.

5.3.1.2 Time domain analysis

Figure 5.4 studies the time domain performance of the switch. The Ansoft Designer software package is used to carry out this simulation. An approximate Spice library for the PIN diode is generated to match the specifications provided by the manufacturer. Figure 5.4 (a) shows the diode currents when a symmetric 6.49MHz pulse train is connected to the switch. The rise and fall times of the pulse train are assumed to be 5ns. As can be seen, the steady state current for each diode is around 8mA. There is a reverse recovery time (RRT) of around 12 ns during transition of each PIN diode from ON to OFF condition during which the stored charges in the diode is removed. Figure 5.4 (b) shows another example with a positive pulse width of 30 ns. The effective positive pulse width is reduced to 18.5ns. As shown later, this affects the amplitude control capability of the structure.

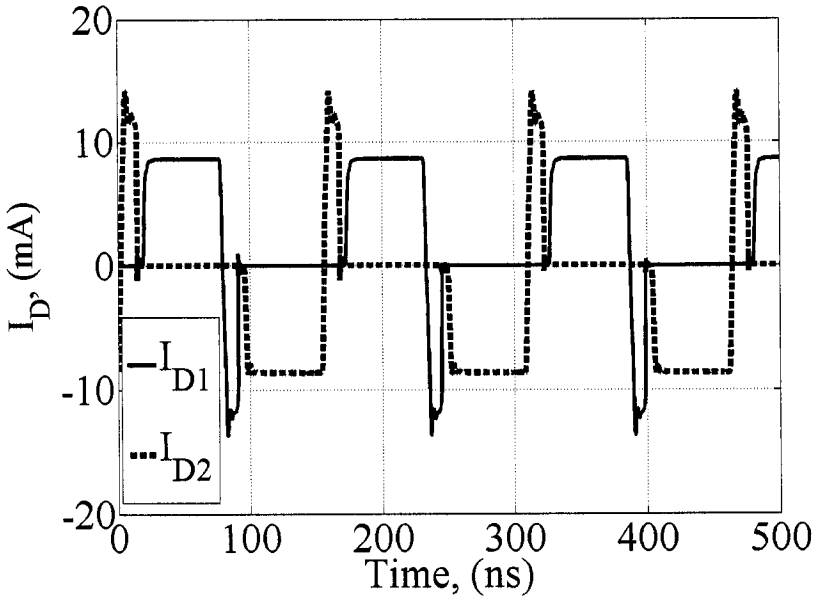

(a)

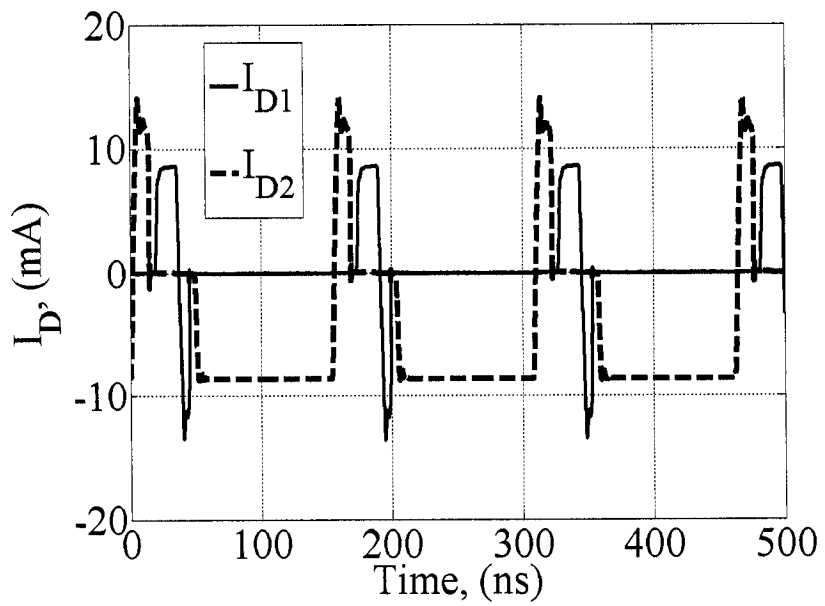

(b)

Figure 5.4 Diodes Currents. (a) Using symmetric control pulse train. (b) Using positive pulse width of 30ns.

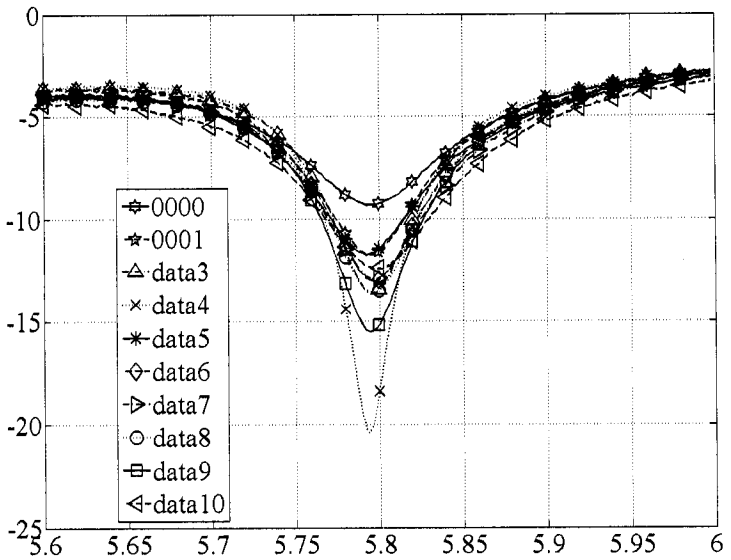

Figure 5.5 Measured S_{11} in different switching states.

5.3.1.3 Measured system S_{11}

Figure 5.5 compares the measured S_{11} from the output of RF circuit in Figure 5.1(b) in different combinations of the state possibilities. There are 16 state possibilities for four switches with two states each. However, based on the symmetric property of the structure there are 10 different states. For example, a switching state of 0101 means the first and third switches are in the state one (D1 ON, D2 OFF), but the second and fourth switches are in state two (D1 OFF, D2 ON). Likewise, a switching state of 0000 means all the switches are in state two, and so on.

As can be seen in Figure 5.5, S_{11} is lower than -12dB for all the switching states except 0000 which is around -9 dB. This is mainly due to a symmetric choice for the orientation of the switches. Based on Figure 5.1 (a) when one switch is in state two the longer branch is active. Therefore, in Figure 5.1 (b) for the switching state 0000 all the

long branches are active. In addition, two long branches from two adjacent switches in the first and second antennas are very close. The same trend happens for the third and fourth elements. Therefore, the mutual coupling between these long branches deteriorates S_{11} in the state 0000. Thus, it is expected that by flipping the two ends arms around, S_{11} should be improved.

5.3.2 Pattern measurement results

5.3.2.1 Measurement setup

Pattern measurement using a network analyzer is based on measuring S_{21} at different angles which requires the same frequency operation for both the transmitter and receiver. In the MSBF structure, if the transmitted signal is on f_c, the received signal by the MSBF antenna array is first on f_c, but it is transferred to $f_c - f_s$ after switching. Therefore, a pattern measurement setup using a spectrum analyzer was designed for this purpose which is shown in Figure 5.6 (a). In this setup, the HP8672A synthesized oscillator is used with the double-ridged waveguide horn antenna model 3115 as transmitter. The horn antenna is a linearly-polarized broadband antenna covering the frequency range of 1GHz to 18GHz. The measurements are carried out in an anechoic chamber with the size 2m x 3m x 4m. The distance between the transmit and receive antennas is 2.7m. A photo of the anechoic chamber, transmit horn antenna, and the receiver are shown in Figure 5.6 (b).

A lab-view code is developed which controls all the devices to measure the pattern. The HP8569B spectrum analyzer is connected to the output of the MSBF receiver. The spectrum analyzer, synthesized RF oscillator and positioner are controlled

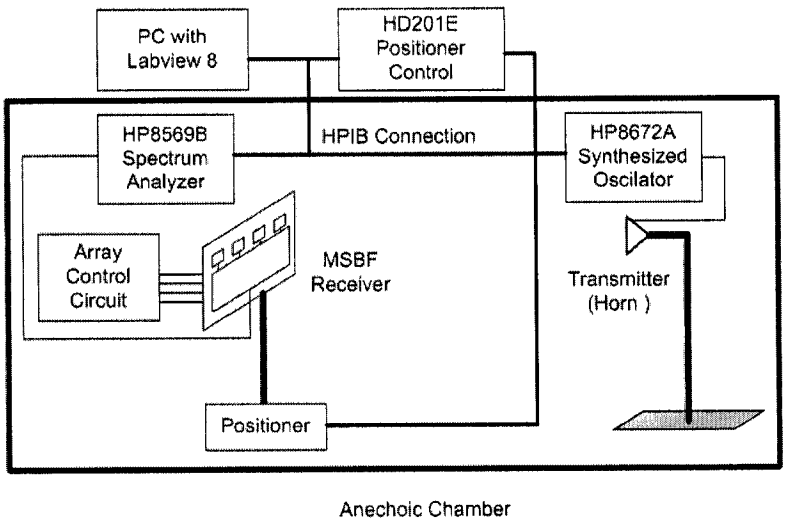

(a)

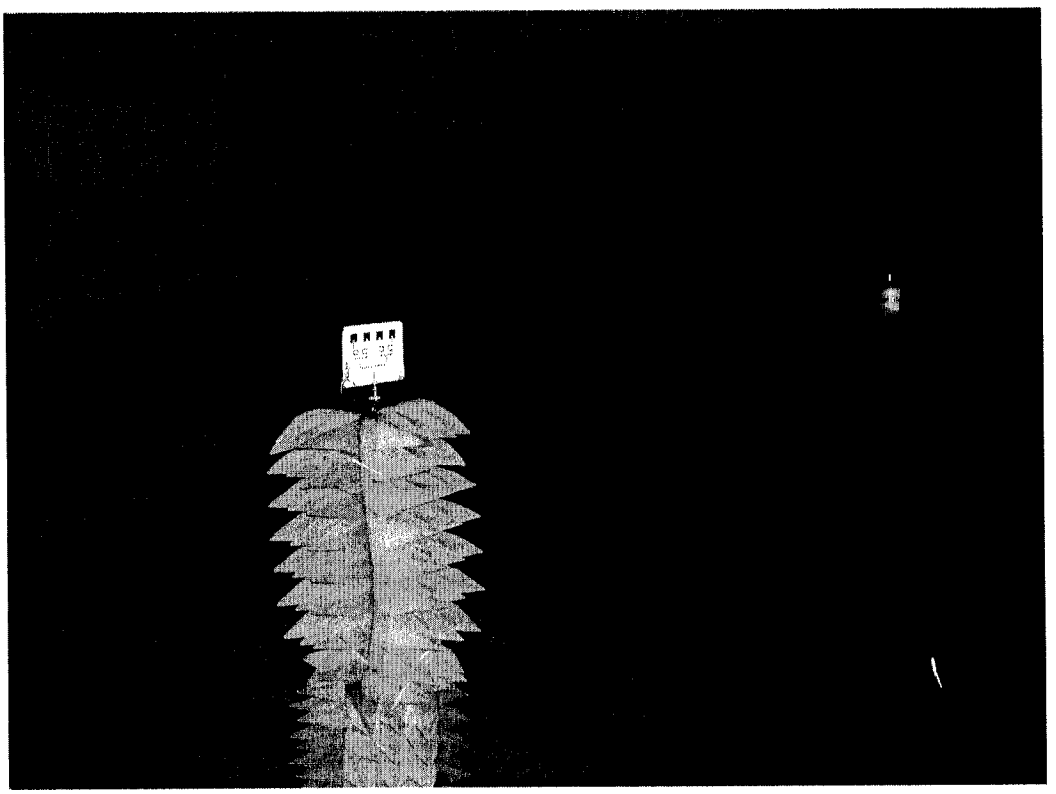

(b)

Figure 5.6 Pattern measurement setup using spectrum analyzer. (a) Setup block diagram. (b) anechoic chamber.

using a PC though HP-IB connection. In the beginning the synthesized oscillator is started using HP-IB control. Then the lab-view code controls the antenna positioner and makes sure that it goes to the right angle through a feedback loop. For each angle the trace of the spectrum analyzer is read by the PC and is transferred to the lab-view. The parameters of the horizontal and vertical axes of the spectrum analyzer are also transferred to the lab-view for locating the desired frequency in the trace and calculating the amplitude. The power of desired frequency $f_c - f_s$ is plotted as function of the positioner angle.

It is important to reduce the noise effect in the spectrum analyzer. In HP8569B spectrum analyzer the noise can be reduced in three ways: averaging, reducing the frequency resolution, and reducing the video filter bandwidth. Using averaging slows down the measurement speed. Therefore, in this measurement setup frequency resolution and video filter control are used for noise reduction.

5.3.2.2 Beam steering

In this part the capability of the MSBF for beam steering is studied. The synthesized oscillator and the center frequency of the spectrum analyzer are adjusted to 5.8GHz. The switching frequency of the control circuit is chosen as 6.49MHz. Figure 5.7(a)-(d) shows the steered uniform normalized patterns measured when control pulses time delays and pulse widths are adjusted for scanning at $\theta_s = 0^\circ, 20^\circ, -10^\circ,$ and 35°, respectively. In each case the pattern obtained using HFSS simulation is also shown for comparison. As can be seen, the pattern is scanned to the proper angles in all cases. In addition, there is a good agreement between HFSS simulations and measurements. The

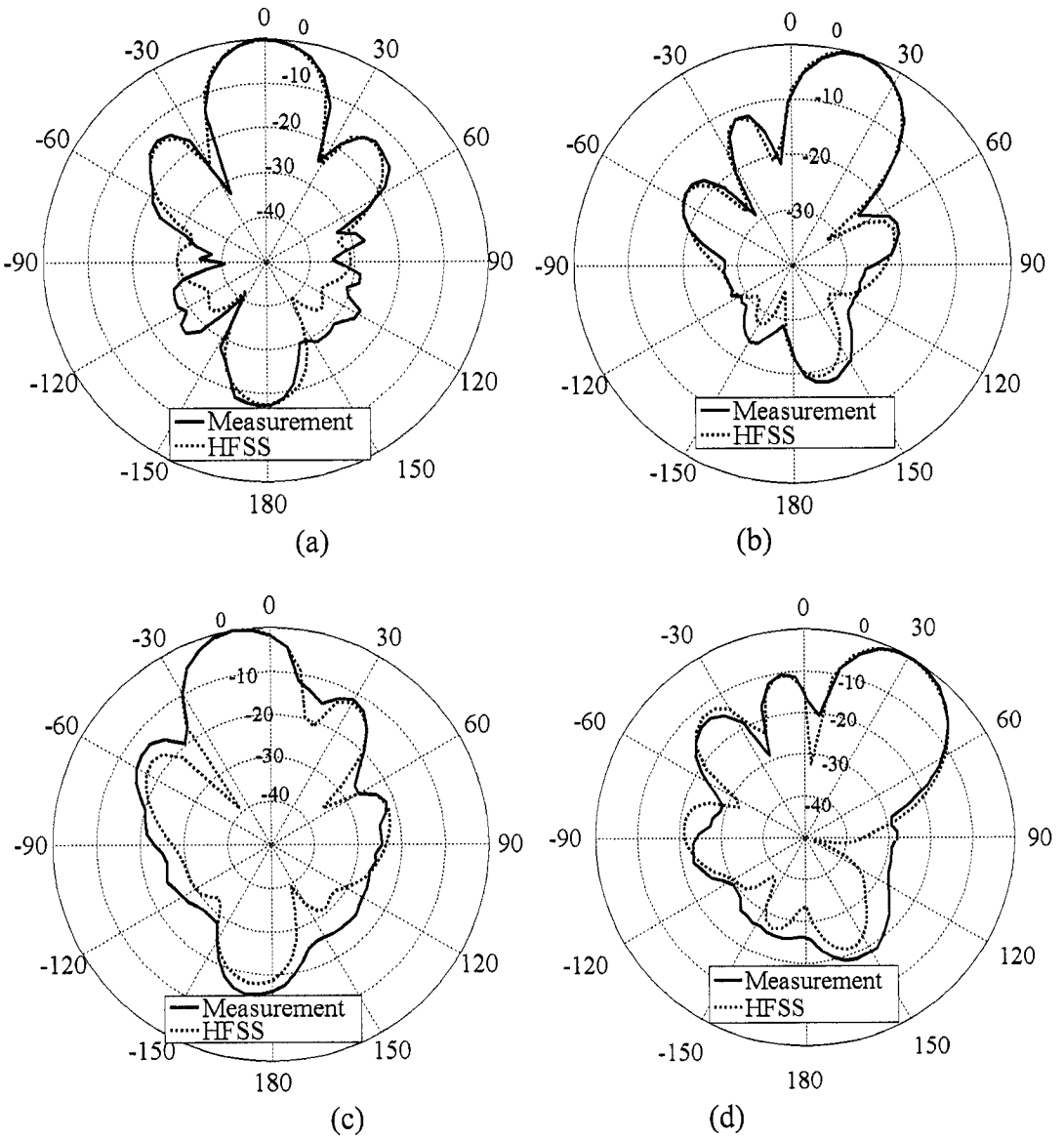

Figure 5.7 Measured and HFSS-simulated radiation patterns for (a) $\theta_s = 0^\circ$ (b) $\theta_s = 20^\circ$ (c) $\theta_s = -10^0$ (d) $\theta_s = 35^0$.

pulse width IC address 252 which is equivalent to $\tau = 77ns$ is applied to all pulse width ICs. The time delays for the four scan angles are shown in Table 1. Figure 5.8 shows the measured control signals applied to the switches for $\theta_s = 35^\circ$ as an example. The control signals are measured using the DPO4104 Tektronix digital scope with 1GHz bandwidth

Table 1 Time delay for different scan angles.

	TD1	TD2	TD3	TD4
$\theta_s = 0^\circ$	0 ns	0ns	0ns	0ns
$\theta_s = 20^\circ$	0 ns	26ns	53ns	79ns
$\theta_s = -10^0$	40ns	27ns	13ns	0ns
$\theta_s = 35^0$	0ns	44ns	88ns	133ns

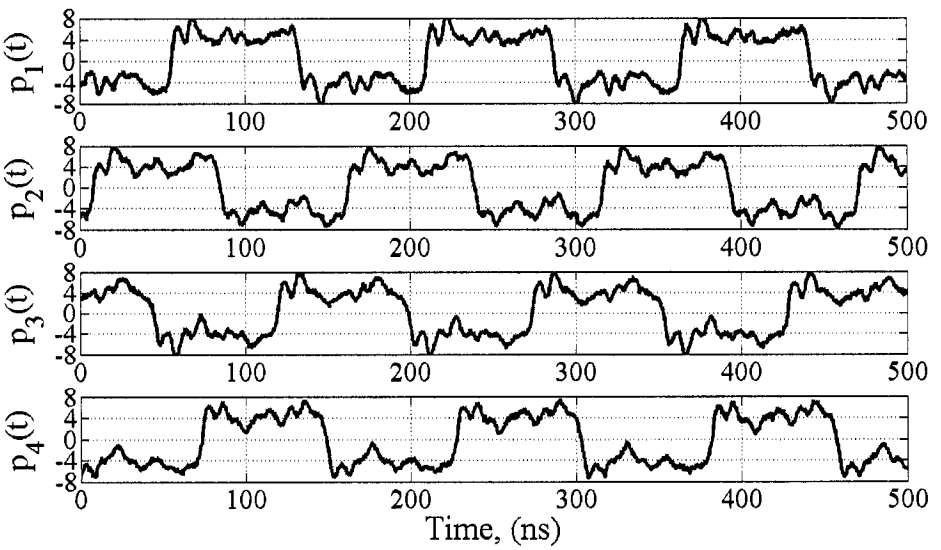

Figure 5.8 Control signals applied to the four branches for $\theta_s = 35^0$.

with four simultaneous channels. The control signals have rise and fall times around 5ns. The zero to zero volts pulse width is measured to be 76.6ns which is close to the desired 77ns value. The measured time delay values are 0ns, 45.9ns, 88.9ns and 136.1ns for this example. Based on the desired values in Table 1, the maximum time delay error is 3.1ns which is a 2.33% error.

5.3.2.3 Side-lobe control

In this part the SLL control capability of the MSBF structure is investigated. Figure 5.9 (a)-(d) shows the broadside Chebyshev normalized patterns with -13.3dB, -14.5dB, -15.3dB, and -20dB sidelobe levels implemented using MSBF structure. The corresponding positive pulse widths (PPW) are 50ns, 44ns, 41ns and 30 ns, respectively. The achieved SLL using MSBF are -16.2dB, -17.5dB, -19.2dB, and -27.3dB, respectively. The corresponding SLL using HFSS simulations are -16dB, -17.3dB, -19dB, and -23.6dB, respectively. The reason the SLL is lower with MSBF is that PPW is the zero to zero pulse width and the effective amplitude is smaller than what is originally planned for. In addition, the rise and fall times and the PIN diode switching time affect the amplitude attenuation. This is especially significant for small PPW (Figure 5.9 (d)). As can be seen the measured SLL is lower than HFSS simulation results by more than 4dB and the pattern is broadened. In fact, the rise and fall times of the control signals increase as pulses become shorter which reduces the effective amplitude tapering. Figure 5.10 (a) and (b) demonstrates the joint SLL control and beam scanning of the MSBF structure. This figure shows the measured and HFSS-simulated patterns steered to 20° and 35°, respectively. Chebyshev patterns with 15.5dB SLL are examined, which is equivalent to using PPW=40ns for the two end elements. As can be seen, the patterns are steered to the proper angles. In addition, again, the SLL with MSBF is lower than HFSS simulations and lower than the target value.

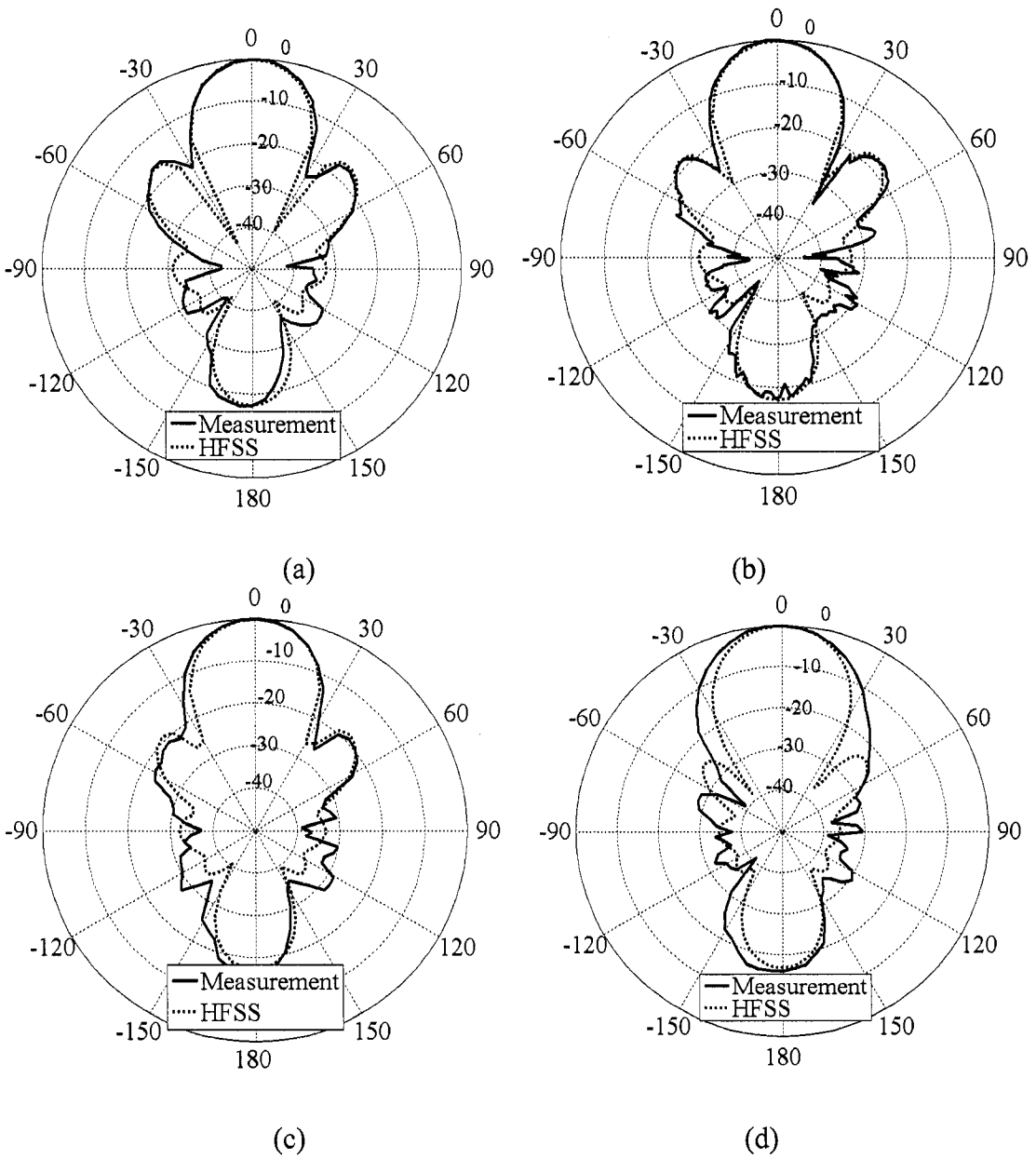

Figure 5.9 Study of SLL control with MSBF. (a) PPW=50ns. (b) PPW=44ns. (c) PPW=41ns. (d) PPW=30ns.

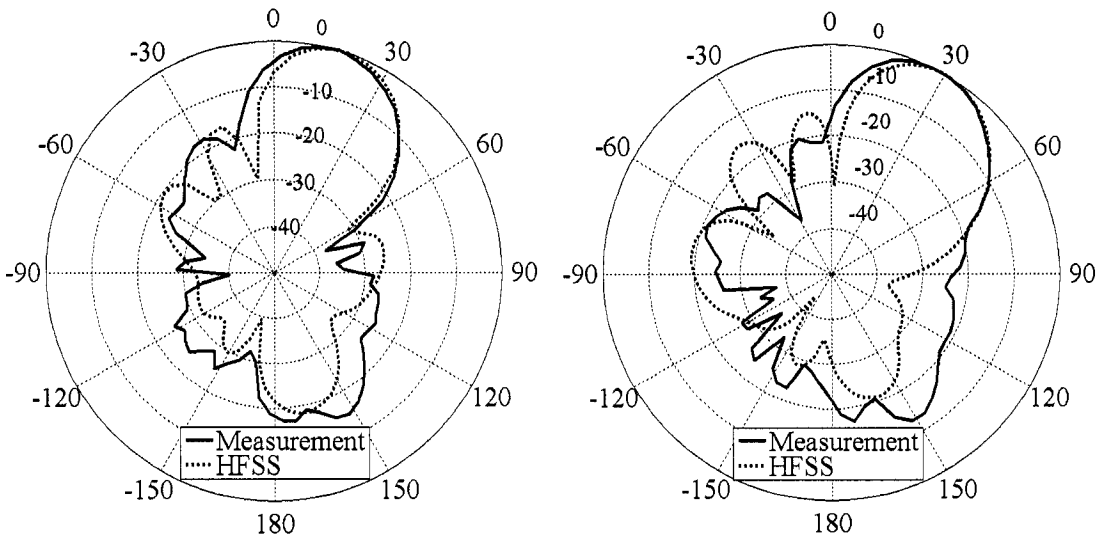

Figure 5.10 Study of joint sidelobe control and scanning. (a) PPW=40ns and $\theta_s = 20^\circ$. (b) PPW=40ns and $\theta_s = 35^\circ$.

5.3.2.4 Null-forming

In this part the null-forming capability of the MSBF structure is investigated. In Figure 5.11(a) a weight vector is applied to the array to steer the beam to 20° and introduce nulls in the $-30^\circ, -10^\circ$, and 50° directions. The pattern using HFSS is also shown. As can be seen the desired patterns are generated. The null depths for $-30^\circ, -10^\circ$, and 50° directions are -22dB, -13.5dB, and -20dB. The null depths from HFSS simulations are -20dB, -22.5dB, and -25dB, respectively. Figure 5.11(b) shows another pattern where a weight vector is applied to the array that directs the beam to the -20° and introduces nulls in the $-50^\circ, 10^\circ$, and 70° directions. As can be seen, the nulls are again introduced in the correct directions. The measured null depths for $-50^\circ, 10^\circ$,

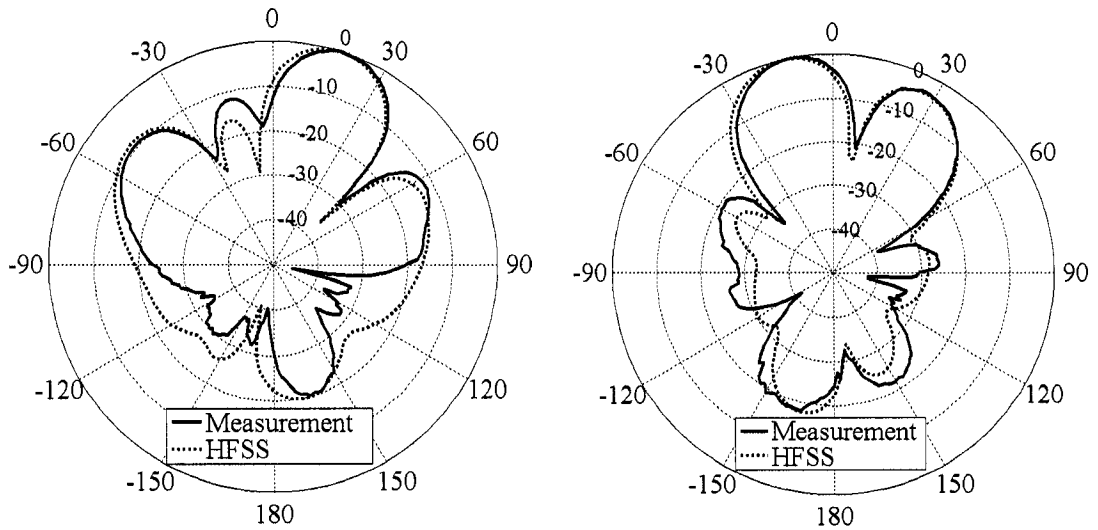

Figure 5.11 Study of null-forming with MSBF. (a) Main beam in the 20° and nulls in the −30°,10°, and 50° directions. (b) Main beam in the −20°, and nulls in the −50°,10°, and 70° directions.

and 70° are -23.5dB, -21, and -31.5, respectively. The corresponding null depths for HFSS simulations are -30dB, -24dB, and -30dB, respectively.

As can be seen, considerable null depths are achieved in both examples. However, the null depths from HFSS simulations are deeper on average. This is mostly due to the errors in the measurements, rise time and fall time of the control signals, switching time of the PIN diodes. From the SLL control examples in Figure 5.10, the pulse widths do not correspond exactly to the amplitude attenuations, while for null-forming both phase shift and amplitude taper should be accurate. In practice the pulse widths should be calibrated to get deeper nulls which are ignored in these measurements.

5.4 Conclusion

The microwave sampling beamformer (MSBF) is studied and verified experimentally. A new compact switch is designed and simulated in the frequency domain using full-wave analysis and also in the time domain. A four element phased array antenna with the control hardware based on the new weighting technique is constructed. The constructed MSBF structure has eight bits phase shift resolution and 12 bits amplitude control resolutions, whose eight bits are used in the measurements. S-parameters of the whole structure are investigated in different switching states. The implemented MSBF structure is examined for beam-steering, sidelobe control, joint beam-steering and sidelobe control, and null-forming. Different examples show that the structure steers the beam accurately to the desired angle. For SLL control and null-forming the pulse width needs to be calibrated to achieve the exact SLL and introduce deep nulls. Nulls with depths more than -30dB are measured.

Chapter 6

Conclusion and Future work

6.1 Conclusion

An MBF structure is a suitable implementation technique for commercial wireless communication applications, due to its low complexity, higher data rate and possible integration with existing cellular base stations. However, there are two problems in a MBF structure; one is the lack of antenna array signals in the processor and the other is the need of phase shifters and amplitude control elements. This thesis addresses these problems.

A new perturbation technique to apply adaptive beamforming and DOA estimation to MBF structures is proposed. The new perturbation technique is based on estimation of the array signal vector in $L+1$ perturbation cycles by making the array signals temporally correlated. By estimating the array signal vector, most of the multi-port algorithms can be used with the MBF structure. The temporal correlation is provided by increasing the weighting rate or reducing the receiver bandwidth. It is observed that optimum perturbation is achieved by inverting the phase of the antenna elements sequentially. In addition, a proper perturbation rate is around LB_T where B_T is the signal transmission bandwidth. The proposed perturbation technique is applied to the ULMS algorithm and its performance is compared analytically and numerically with that of the multi-port ULMS. It is observed that the adaptive single-port algorithm achieves a lower misadjustment than the corresponding multi-port algorithm with $\gamma = -2$ and $Q \cong L$ where, γ is the perturbation coefficient and Q is the weighting rate coefficient.

The proposed perturbation technique is also employed for DOA estimation. The DOA estimation technique is based on adaptively introducing nulls in the direction of signal sources. The proposed technique performance is compared with the spectral MUSIC and beam-space MUSIC. It is observed that the proposed technique is superior to MUSIC as long as the SNR is not very low.

A new implementation technique for phase shifters and amplitude control elements is devised. In this technique both phase shift and amplitude control are realized in one block. This technique is based on fast switching of the antenna array signals using control pulses with adjusted time delay and pulse width. The new technique has the potential for super-resolution weighting due to the availability of high resolution time delay and pulse width control ICs. The main limitation of the technique is that the speed of the switches and the control hardware should be more than the signal transmission bandwidth.

The proposed technique is verified by different simulations in the frequency and time domains using wire and microstrip antenna arrays. A switch for continuous impedance matching and higher power efficiencies is designed. A harmonic analysis of the structure shows that an image replica may be generated in the structure depending on the relation between the carrier frequency and the sampling frequency. Techniques to reject or lower the effect of this image replica are devised.

A prototype of the MSBF structure is built and tested. A four element microstrip antenna array with the feeding network composed of Wilkinson combiners and a switch with PIN diodes are designed and constructed. In addition, a four branch pulse-width time-delay control circuit at a switching frequency of 6.49MHz is also constructed. The

pulse-width and time delay resolutions are 12bits and eight bits, respectively. In this work the antenna array is built using RO-4350B substrate with $\varepsilon_r = 3.66$ and 20mils substrate thickness which provides a narrow bandwidth for inset feed patch antenna array. The main reason for this choice has been to reduce noise folding due to switching. The structure is tested for beam steering, SLL control, SLL control with beam steering, and null forming. The structure scans the beam to the desired directions. For SLL control, when pulse widths are not very narrow, the SLL control is accomplished effectively. However, when pulse widths are narrow, the control hardware fails to work properly. In the null-forming examples nulls deeper than -30dB are recorded.

6.2 Contributions

The main research contributions of this PhD thesis includes the following activities:

- The MSBF structure is proposed for the first time and verified by simulations in the frequency domain using a microstrip antenna array [106]. In addition, several other related issues such as always matched switch design [106], [107], the effects of switch nonideal performance, and system flexibility with advanced signal processing are investigated in [106]. An study of SNR, power efficiency and sensitivity is also presented in [106].
- The MSBF structure is tested using wire antennas by integration of NEC2 and Matlab software packages [105]. Transients of the MSBF are investigated by including the nonlinearity of the switches and frequency dependence of the microstrip transmission lines and lumped elements [109]-[111]. A faster switch design is proposed in [109].

- A prototype of the MSBF structure including the microwave hardware and control hardware is constructed and tested whose results are presented in [111]. A measurement setup using spectrum analyzer for pattern measurement is devised.
- The finite weight duration and image replica issues are investigated and presented in [107], [110].
- The ULMS algorithm with correlated data samples are investigated and presented in [101].
- A new perturbation technique based on array signal estimation is presented in [92] which estimates the array signal vector in L perturbation cycles. In [93], another version of the perturbation technique with (L+1) perturbation cycles is investigated with ULMS algorithm. In [96], CLMS algorithm is integrated with the perturbation technique.
- Hybrid microwave-digital beamforming is presented in [95] which perturbs the weight vector in the microwave domain and applies the weight vector in the digital domain. In [94], a new technique to reduce the weighting rate burden is proposed.

6.3 Suggested Improvements and Future Work

There are several future research directions to improve, modify or extend the MSBF structure. In addition, the perturbation technique may be extended for different applications. In the following some suggested future tasks that can be carried out for further improvement of the developed structure and beamforming techniques are listed:

- The MSBF structure is designed using passive switches. The structure may be constructed using active switches to bring some gain to switching.

- Faster hardware may be designed to improve the bandwidth of the system.
- The current control hardware works up to 25MHz but the oscillator frequency is not stable more than 10MHz. Therefore, by changing the oscillator it is possible to use the structure for frequencies up to 25MHz.
- The structure may be combined with down-conversion branches and a processor for real adaptive beamforming and/or DOA estimation.
- Other adaptive beamforming and DOA estimation algorithms may be combined with the perturbation technique.

REFERENCES

[1] C. Shannon, "A Mathematical Theory of Communication," *The Bell System Technical Journal,* Vol. 27, pp. 379-423, 623-656, July, October 1948.

[2] T. Rappaport, *Wireless Communications Principles and Practice,* Prentice-Hall, 1996.

[3] L. C. Godara, ''Application of antenna arrays to mobile communications, part I: Performance improvement, feasibility, and system consideration,'' *Proc. of IEEE,* Vol. 85, No. 7, pp. 1031-1060, July 1997.

[4] P. V. Rooyen, M. L. Lotter, D. V. Wyk, *Space-time processing for CDMA mobile communications,* Kluwer Academic Publishers, 2000.

[5] S. Chandran, *Adaptive antenna arrays, trends and applications*, Springer 2004.

[6] L. C. Godara, *Smart Antennas,* Florida: CRC Press, 2004.

[7] L. C. Godara, ''Application of antenna arrays to mobile communications, part II: Beam-forming and direction of arrival considerations,'' *Proc. of the IEEE*, Vol. 85, No. 8, pp. 1195-1254, August 1997.

[8] T. K. Sarkar, M. C. Wicks, M. Salazar-Palma, R. J. Bonneau, *Smart antennas*, Wiley Series in Microwave and Optical Eng., 2003.

[9] B. Vucetic, J. Yuan, *space-time coding,* John Wiley 2003.

[10] R. J. Mailoux, *Phased array antenna handbook*, Boston-London: Arch-House, pp.446-517, 1993.

[11] R. C. Hansen, *Phased Array Handbook*, New York: Wily Series in Microwave Engineering, 1997.

[12] R. K. Bhattacharyya, *Phased array antennas, floquet analysis, synthesis, BFNs, and active array systems*, Wiley series 2006.

[13] J. Litva, T. K. Y. Lo, *Digital beamforming in wireless communications*, Artech House Publishers 1996.

[14] S. Haykin, *Adaptive filter theory*, Prentice Hall, 2002.

[15] A. Alexiou, L. Technologies, M. Haadt, "Smart antenna technologies for future wireless systems: Trends and challenges," *IEEE Communication Magazine*, pp. 90-97, Sept. 2004.

[16] T. Ohira, "Adaptive array antenna beamforming architectures as viewed by a microwave circuit designer," in Proc. Asia-Pacific Microwave Conference, Sydney, pp. 828-833, Dec. 2000.

[17] T. Ohira, ''Analog smart antennas: an overview,'' IEEE PIMRC 2002.

[18] S. Jeon, Y. Wang. Y. Qian, and T. Itoh, T. Ohira, "A novel planar array smart antenna system with hybrid analog-digital beamforming," in IEEE MTT-S Int. Microwave Symp. Dig., Vol.1, pp. 121-124, May 2001.

[19] T. Nishio, Y. Wang, T. Itoh, "Multiple-beam Adaptive Array Architecture using Channel-level FDMA Concept," IEEE AP-S International Symposium, June 2003.

[20] S. Jeon, Y. Wang. Y. Qian, and T. Itoh, T. Ohira, "A novel smart antenna system implementation for broadband wireless communication," *IEEE Trans. Antennas Propagat.*, Vol. 45, pp. 2324-2332, Dec. 1997.

[21] T. Nishio, Y. Wang, H. P. Tsai, Itoh, T., "A high-speed adaptive antenna array with simultaneous multiple-beamforming capability," *IEEE Trans. Microwave Theory Tech.*, Vol. 51, No. 12, pp. 2483-2494, Dec. 2003.

[22] A. Cantoni, "Application of orthogonal perturbation sequences to adaptive beamforming," *IEEE Trans.* Antennas *Propugat.,* Vol. 28, pp. 191-202, Mar. 1980.

[23] R. M. Davis, D. C. Farden, and P. J-S. Sher, "A coherent perturbation algorithm," *IEEE* Trans. *Antennas Propagat.,* Vol. 34, pp. 350-387, Mar. 1986.

[24] B. G. Wahlberg, I. M. Y. Mareels, I. Webster, "Experimental and theoretical comparison of some algorithms for beamforming in single receiver adaptive arrays," *IEEE Trans. on Antenna. Propagat.*, Vol. 39, No. 1, pp. 21-28, Jan. 1991.

[25] I. Webster, R. J. Evans, and A. Cantoni, "Robust perturbation algorithms for adaptive antenna arrays," *IEEE Trans. Antennas Propagat.,* Vol. 38, pp. 195-201, Feb. 1990.

[26] L. C. Godara and A. Cantoni, "Analysis of constrained LMS algorithm with application to adaptive beamforming using perturbation sequences," *IEEE Trans. Antennas Propagat.,* Vol. 34, pp. 368-379, Mar. 1986.

[27] L. C. Godara and A. Cantoni, "Analysis of the performance of adaptive beamforming using perturbation sequences," *IEEE Trans. Antenna. Propagat.,* Vol. 31, pp. 268-279, Mar. 1983.

[28] S. Denno et al, "M-CMA for digital signal processing adaptive antennas with microwave analog beamforming," IEEE Aerospace Conf., Big Sky, Mar. 2000.

[29] S. Denno, T. Ohiro, "Modified constant modulus algorithm for digital signal processing adaptive antennas with microwave analog beamforming," *IEEE Trans. Antennas Propagat.* , Vol. 5o, No. 6, pp. 850–857, June 2002.

[30] R. M. Davis, "Phase-Only LMS and Perturbation Algorithms," *IEEE Trans. Aerospace and Electronic Systems*, Vol. 34, No. 1, pp. 169-178, Jan. 1998.

[31] T. Do-Hong, P. Russer, "Signal processing for wideband smart antenna array applications," *IEEE Microwave magazine*, pp. 57-67, Mar. 2004.

[32] T. Ohira et al, "Electronically steerable passive array radiator for low-cost analog adaptive beamforming," IEEE International Conference Phased Array Systems Tech., pp. 101-104, Dana Point, CA, May 2000.

[33] K. Krim, M. Viberg, "Two decades of array signal processing, the parametric approach," IEEE Signal Processing Magazine, pp. 67-94, July 1996.

[34] D. E. Dudgeon, "Fundamentals of digital array processing," *Proc. IEEE, V*ol. 65, pp. 898-904, 1977.

[35] R. A. Mucci, "A comparison of efficient beamforming algorithms," *IEEE Trans. Acous., Speech, Signal processing*, Vol. ASSP-32, pp. 548-558, 1984.

[36] R. G. Pridham, R. A. Mucci, "Digital interpolation beamforming for low-pass and bandpass signals," *Proc. of IEEE*, Vol. 67, pp. 904-919, 1979.

[37] H. Fan, E. I. El-Masry, and W. K. Jenkins, "Resolution enhancement of digital beamforming," *IEEE Trans. Acous., Speech, Signal Processing*, Vol. ASSP-32, pp. 1041-1052, 1984.

[38] M. Kozak, M. Karaman, "Digital phased array beamforming using single-bit delta-sigma conversion with non-uniform oversampling," *IEEE Trans. Sonics Ultrason., Ferroelec.,Freq. Contr.,*Vol.48, No. 4, pp.922-931, July 2001.

[39] K. Ranganathan, M. K. Santy, T. N. Blalock, J. A. Hossack, W. F. Walker, "Direct sampled I/Q beamforming for compact and very low-cost ultrasound imaging," *IEEE Trans. Sonics Ultrason., Ferroelec.,Freq. Contr.,* Vol. 51, No. 9 pp. 1082-1094, Sept. 2004.

[40] T. Ohira, Y. Suzuki, H. Ogawa, and K. Kamitsuna, "Megalithic microwave signal processing for phased-array beamforming and steering," *IEEE Trans. Microwave Theory Tech.*, Vol. 50, pp. 3052-3058, Dec. 2002.

[41] J. Roderick, H. Krishnaswamy, K. Newton, H. Hashemi, "Silicon-based ultra-wideband beam-forming," *IEEE J. Solid-State Circuits,* Vol. 41, Issue 8, pp. 1726-1739, Aug. 2006.

[42] T. S. Chu, J. Roderick, and H. Hashemi, "An integrated ultra-wideband timed array receiver in 0.13 _m CMOS using a path-sharing true time delay architecture," *IEEE J. Solid-State Circuits*, Vol. 42, No. 12, pp. 2834-2850, Dec. 2007.

[43] Y. Ji, K. Inagaki, O. Shibata, Y. Karasawa, "Receive mode of optical signal processing multibeam array antennas," *IEEE Microwave and Guided Wave Letters*, Vol. 8, No. 7, July 1998.

[44] S. Obayashi, H. Shoki, O. Shibata, H. Kasami, S. Otaka, H. Tsurumi, and Y. Suzuki, "An adaptive array for high speed wireless local loop steered by local signal phase shifters," IEEE Antennas and Propagation Society International Symposium., Vol. 2, pp.1436-9,1999.

[45] H. Hashemi, X. Guan, A. Komijani, A. Hajamiri, "A 24-GHz SiGe phased-array receiver-Lo phase-shifting approach," *IEEE Trans. Microwave Theory Tech.*, Vol. 53, No. 2, pp. 614-626, Feb. 2005.

[46] A. Hajimiri, H. Hashemi, A. Natarajan, X. Guan, A. Komijani, " Integrated phased array systems in silicon," *Proc. of IEEE*, Vol. 93, No. 9,, Sept. 2005.

[47] S. A. Mitilineos, and C. N. Capsalis, "A new, low-cost, switched beam and fully adaptive antenna array for 2.4 GHz ISM applications," *IEEE Trans. Antennas Propagat.,* Vol. 55, No. 9, pp. 2502-2508, Sept. 2007.

[48] C. Sun, A. Hirata, T. Ohira, N. C. Karmakar "Fast beamforming of electronically steerable parasitic array radiator antennas: theory and experiment," *IEEE Trans. Antenna. Propagat* , Vol. 52, No. 7, pp. 1819–11832, July 2004.

[49] K. Yang, and T. Ohira, "Realization of Space–Time Adaptive Filtering by Employing Electronically Steerable Passive Array Radiator Antennas,'' *IEEE Trans. Antenna. Propagat.,* Vol. 51, No. 7, pp. 1476-1485, July 2003.

[50] E. Taillefer, A. Hirata, and T. Ohira, "Direction-of-Arrival Estimation Using Radiation Power Pattern With an ESPAR Antenna," *IEEE Trans. Antenna. Propagat.,* Vol. 53, No. 2, pp. 678-684, Feb. 2005.

[51] C. Plapous, J. Cheng, E. Taillefer, A. Hirata, T. Ohira, "Reactance domain MUSIC algorithm for electronically Steerable parasitic array radiator," *IEEE Trans. Antenna. Propagate.,* Vol. 52, No. 12, pp. 3257-3264, Dec. 2004.

[52] J. Lu, D. Ireland, and R. Schlub, "Dielectric Embedded ESPAR (DE-ESPAR) Antenna Array for Wireless Communications," *IEEE Trans. Antennas Propagat.,* Vol. 53, No. 8, pp. 2437-2442, Aug. 2005.

[53] Y. Yusuf, and X. Gong, *Member,* "A low-cost patch antenna phased array with analog beam steering using mutual coupling and reactive loading," *IEEE Antennas and Wireless Propagat. Lettters*, Vol. 7, pp. 81-84, 2008.

[54] A. Sutinjo, M. Okoniewski, and R. H. Johnston, "An octave band switched parasitic beam-steering array," *IEEE Antennas and Wireless Propagate. Letters*, Vol. 6, pp. 211-214, 2007.

[55] J. D. Fredrick, Y. Wang, T. Itoh, "A smart antenna receiver array using a single RF channel and digital beamforming," *IEEE Trans. Microwave Theory Tech.*, Vol. 50, pp. 3052-3058, Dec. 2002.

[56] S. Kim, Y. E. Wang, "A series-fed microstrip receiving array for digital beamforming," *IEEE Antennas and Wireless Propagation Letters*, Vol. 3, 2004.

[57] D. S. Goshi, Y. Wang, T. Itoh, "A compact digital beamforming SMILE array for mobile communications," *IEEE Trans. Microwave Theory Tech.,* Vol. 52, No. 12, pp. 2732-2738, Dec. 2004.

[58] J. D. Fredrick, Y. Wang, T. Itoh, "Smart antenna based on spatial multiplexing of local elements (SMILE) for mutual coupling reduction," *IEEE Trans. Antennas Propagat.* , Vol. 52, No. 1, pp. 106–114, Jan. 2004.

[59] L. Jofre, C. Stoltidou, S. Blanch, T. Mengual, B. Vidal, J. Martí, I. McKenzie, and J. M. del Cura, "Optically Beamformed Wideband Array Performance," *IEEE Trans. Antennas Propagat.,* Vol. 56, No. 6, 1594-1604, June 2008.

[60] H. R. Rideout, J. S. Seregelyi, and J. Yao, "A true time delay beamforming system incorporating a wavelength tunable optical phase-lock loop," *Journal of Lightwave Tech.*, Vol. 25, No. 7, pp. 1761-1770, July 2007.

[61] D. B. Hunter, M. E. Parker, and J. L. Dexter, "Demonstration of a Continuously Variable True-Time Delay Beamformer Using a Multichannel Chirped Fiber

Grating," *IEEE Trans. Microwave Theory Tech.*, Vol. 54, No. 2, pp. 861- 867, Feb. 2006.

[62] L. G. Maloratsky, *Passive RF& microwave integrated circuits*, Elsevier 2004.

[63] L. Devlin, "The design of integrated switches and phase shifters," IEE Tutorial Colloquium, pp. 2/1-2/14, Nov. 1999.

[64] F. Di Paolo, "A simple, high yield 6 to 18 GHz GaAs monolithic phase shifter," *Microwave J.*, pp. 92–104, Apr. 1997.

[65] J. Grajal, J. Gismero, M. Mahfoudi, and F. A. Petz, "A 1.4–2.7 GHz analog MMIC vector modulator for a crossbar beamforming network," *IEEE Trans. Microwave Theory Tech.*, Vol. 45, pp. 1705–1714, Oct. 1997.

[66] F. Ellinger,U. Lott, and W. Bächtold, ''An Antenna Diversity MMIC Vector Modulator for HIPERLAN with Low Power Consumption and Calibration Capability," *IEEE Trans. Microwave Theory Tech.,* Vol. 49, No. 5, May 2001.

[67] J. I. Alonso, J. M. Blas, L. E. Garcia, et. al "Low cost electronically steered antenna and receiver system for mobile satellite communications," *IEEE Trans. Microwave Theory Tech.*, Vol. 44, No. 12, 2438-2449, Dec. 1996.

[68] R. E. Collins ,*Foundations for microwave engineering*, McGraw-Hill International edition, 1992.

[69] B. Widrow, J. McCool, "A comparison of adaptive algorithms based on the methods of steepest descent and random search," *IEEE Trans. Antenna. Propagat.*, Vol. 24, Issue 5, pp. 615 – 637, Sept. 1976 .

[70] T. A. Denidni and G. Y. Delisle, "A nonlinear algorithm for output power maximization of an indoor adaptive phased array," *IEEE Trans. Electromagn. Compat.*, Vol. 37, No. 2, May 1995.

[71] T. A. Denidni, D. McNeil, and G. Y. Delisle, "Experimental investigation of a new adaptive dual-antenna array for handset applications," *IEEE Trans. Veh. Technol.*, Vol. 52, No. 6, Nov. 2003.

[72] E. Van Lil, A. R. Van, "Transmission line model for mutual coupling between microstrip antennas," *IEEE Trans. Antenna. Propagat.*,, Vol. AP-32, No. 8, Aug. 1984.

[73] H. Aoyama, H. Arai, "Mutual coupling matrix estimation and null forming methods for MBF antennas," *IEICE Trans. Commun.*, Vol. E88-B, No. 6, pp. 2305-2312, June 2005.

[74] A. Benalla, K. Gupta, "Multi-port network approach for modeling the mutual coupling effects in microstrip patch antennas and arrays," *IEEE Trans. on Antenna. Propagat.*, Vol. 37, No. 2, pp. 148-152, Sept. 1989.

[75] I.J. Gupta, A.A. Ksienski, "Effect of Mutual Coupling on the Performance of Adaptive Antennas," *IEEE Trans. on Antenna. Propagat.*, Vol. 31, No. 5, pp. 785-791, Sept. 1983.

[76] G. Y. Delisle, J. A. Cummins, "Mutual coupling in the signal-to-noise ratio optimization of antenna arrays," *IEEE Trans. Electromagn. Compat.*, Vol. EMC-15, No. 2, pp. 38-44, May 1973.

[77] G. Y. Delisle, J. A. Cummins, S. M. Sanzgiri, "Optimum processing of antenna array signals in the presence of discrete noise sources," *IEEE Trans. Electromagn. Compat.*, Vol. EMC-16, No. 2, pp. 98-106, May 1974.

[78] P. Maagt, R. Gonzalo, Y. C. Vardaxoglou, and J. M. Baracco, "Electromagnetic bandgap antennas and components for microwave and (sub) millimeter wave applications," *IEEE Trans. Antenna. Propagat.,* Vol. 51, No. 10, pp. 2667-2677, Oct. 2003.

[79] F. Yang, Y. Rahmat-Samii, "Microstrip antennas integrated with electromagnetic band-gap (EBG) structures: a low mutual coupling design for array applications," *IEEE Tran. On antenna and propagation*, Vol. 51, No. 10, pp. 2936-2946, Oct. 2003.

[80] C. Chunyue, L. Yinghua, "Mutual coupling calibration algorithm of array antennas and its error estimation," Proceedings. ICSP '04., 7th International Conference on signal processing, pp.487-490, 2004.

[81] Y. Wang, S. Xu, "Mutual coupling calibration of DBF array with combined optimization method," *IEEE Trans. Antennas Propagat.*, Vol. 51, No. 10, pp. 2947–2952, Oct. 2003.

[82] K. R. Dandekar, H. Ling, G. Vu, "Experimental study of mutual coupling compensation in smart antenna applications," *IEEE Trans. Wireless Commun.*, Vol. 1, No. 3, pp. 480-487, July 2002.

[83] R. S. Ade, T. K. Sarkar, "Elimination of the effects of mutual coupling in an adaptive nulling system with look direction constraint," IEEE AP-S International Symposium, Vol. 2, pp. 1164 – 1167, July 1996.

[84] R. Nitzberg, "effects of errors in adaptive weights," *IEEE Trans. on Aerospace and Electronic Systems*, Vol. AES 12, No. 3, May 1976.

[85] M. Wennstrom, T. Oberg, A. Rydberg, "Effects of finite weight resolution and calibration errors on the performance of adaptive array antennas," *IEEE Trans. on Aerospace and Electronic Systems*, Vol. 37, No. 2, April 2001.

[86] L. Godara, "The effect of phase-shifter errors on the performance of the adaptive antenna array beamformer," IEEE Journal of Socienic Engineering, Vol. 10, Issue 3, pp. 278-284, 1985.

[87] W. P. M. N. Keizer, "Element failure correction for a large monopulse phased array antenna with active amplitude weighting," *IEEE Trans. Antennas Propagat.*, Vol. 55, No. 8, pp. 2211-2218, Aug 2007.

[88] H.G. Park, J. H. Jung, H. S. Oh and M.G. Kyeong, "Model based antenna array calibration for smart antenna systems," *IEE Electronics Letters,* Vol. 38, No.15, July 2002.

[89] B. C. Ng and C. M. S. See, "Sensor-array calibration using a maximum likelihood approach," *IEEE Trans. Antennas Propagat.*, Vol. 44, pp. 827–835, June 1996.

[90] T. W. Nuteson, J. E. Stocker, J. S. Clark, D. S. Haque, G. S. Mitchell, ''Performance characterization of FPGA technique for calibration and beamforming in smart antenna application,'' *IEEE Trans. Microwave Theory Tech.*, Vol. 50, No. 12, pp. 3043-3051, Dec. 2002.

[91] E. K. L. Hung, ''Matrix-construction calibration methods for antenna arrays," *IEEE Trans. On Aerospace and Electronics Systems*, Vol. 36, pp. 819-828 July 2000.

[92] S. Farzaneh, A. Sebak, ''Fast adaptive microwave beamforming using array signal estimation,'' *IEEE Trans. Antennas Propagat.,* Vol. 55, No. 3, pp. 850-858, Mar. 2007.

[93] S. Farzaneh, A. Sebak, "Adaptive microwave beamforming using high weighting rate and ULMS algorithm," IEEE conference on vehicular technology, Montreal, Canada, Sept. 2006.

[94] S. Farzaneh, A. Sebak, "Adaptive microwave beamforming with low weighting rate requirement," ISSSE conference, Montreal, Canada, July 28-August 2, 2007.

[95] S. Farzaneh, A. Sebak, ''Hybrid microwave-digital beamforming using fast perturbations,'' *IEEE Trans. Antennas Propagat.,* submitted for publication.

[96] S. Farzaneh, A. Sebak, ''Adaptive microwave beamforming using fast perturbation,'' presented in ANTEM/URSI, Montreal, Canada, July 2006.

[97] N. J. Bershad, L. Z. Qu, "LMS adaptation with correlated data-a scalar example," *IEEE Trans. Acoust. Speech, Signal Processing*, Vol. ASSP-32, No. 4, pp. 695-700, Aug. 1984.

[98] S. C. Douglas, W. Pan, ''Exact expectation analysis of the LMS adaptive filter,'' *IEEE Trans. Signal Proccesing,* Vol. 43, No. 12, pp. 2863-2871,Dec. 1995.

[99] S. C. Douglas, "Exact expectation analysis of the LMS adaptive filter for correlated Gaussian input data," in *Proc. 26th Ann. Asilomar Conf. Signals, Sys., Comput.*, Vol. 1, pp. 566-570, Oct. 1992.

[100] M. Rupp, H. J. Butterweck, "Overcoming the independence assumption in LMS filtering,'' *Proc. of the 37th Asilomar Conf. on Signals, Systems & Computers*, 607 – 611, 2003.

[101] S. Farzaneh, A. Sebak, "Effect of temporal correlation on the adaptive beamforming performance," IEEE AP-S International Symposium, Hawaii, US, pp. 3864-3867, June 2007.

[102] S. W. Nah, H. Arai "Beam-space MUSIC DOA system using phase shifter," *IEICE Trans. Commun.*, Vol.E90–B, No.2, 291-295, Feb. 2007.

[103] F. Li and H. Liu, "Statistical analysis of beam-space estimation for direction-of-arrivals," *IEEE Trans. Signal Process.* , Vol. 42, No. 3, pp. 604-610, Mar. 1994.

[104] C. Sun and Y. X. Yang, "On beampattern design for beamspace MUSIC," Acoustical Science and Technology, Vol. 25, No. 1, pp. 2-8, Jan. 2004.

[105] S. Farzaneh, A. Sebak, "Low complexity amplitude-phase weighting for microwave beamforming," IEEE AP-S International Symposium and USNC/URSI national radio science meeting, pp. 299-302, July 2005.

[106] S. Farzaneh, A. Sebak, "A Novel amplitude-phase weighting for analog microwave beamforming," *IEEE Trans. Antennas Propagat.*, Vol. 54, No. 7, pp. 1997-2008, July 2006.

[107] S. Farzaneh, A. Sebak, R. Paknys, "A new switch design for microwave sampling beamformer," in proceedings of ANTEM/URSI 2006, Montreal, Canada, July 2006.

[108] S. Farzaneh, A. Sebak, ''Microwave sampling beamformer with finite pulse train," IEEE AP-S International Symposium, Hawaii, US, pp. 1941-1944, June 2007.

[109] S. Farzaneh, A. Sebak, ''A transient analysis of microwave sampling beamformer," presented in URSI conference, Ottawa, Canada, July 2007.

[110] S. Farzaneh, A. Sebak, ''Modified microwave sampling beamformer for fast weighting control and image rejection,'' *IEEE Trans. Antennas Propagat.*, accepted for publication.

[111] S. Farzaneh, A. Sebak, ''Microwave sampling beamformer: prototype verification and switch design,'' *IEEE Trans. Microwave Theory Tech.*, conditionally accepted for publication.

[112] http://www.si-list.net/swindex.html, July 9, 2008.

[113] D. M. Pozar, microwave and RF wireless systems, Univ. of Massachusetts at Amherst, 2001.

[114] E. S. Eddine, H. Dhafir, P. M. Masud, R. N. Epee, "Implementation of the control circuitry for a new phase shifter and gain control element for microwave beam forming," Undergraduate student group project, Concordia University, March 2007.